Jacobs University Bremen
School of Engineering and Science

PhD Thesis

Impact of Local Magnetic Moments on the Anderson Metal-Insulator Transition

Daniel Jung

July 29, 2014

Presented to the

School of Engineering and Science

in partial fulfillment of the requirements for the degree of

Doctor of Philosophy in Physics

Committee

Prof. Dr. Stefan Kettemann (advisor)
Prof. Dr. Ulrich Kleinekathöfer
Prof. Dr. Keith Slevin (external)

Date of defense: March 24, 2014.

"Very few believed [in localization] at the time, and even fewer saw its importance; among those who failed to fully understand it at first was certainly its author. It has yet to receive adequate mathematical treatment, and one has to resort to the indignity of numerical simulations to settle even the simplest questions about it."

P. W. Anderson, Nobel lecture (1977)

Abstract

This thesis considers the impact of local magnetic moments on the Anderson transition, which is a disorder-induced quantum phase transition from a metallic to an insulating phase. In certain doped semiconductors like phosphorus-doped silicon (Si:P), a metal-insulator transition (MIT) is observed which is driven not only by disorder, but also by interaction. The latter gives rise to a MIT by itself, the Mott-Hubbard transition. Furthermore, local magnetic moments have been found in Si:P, which persist deep into the metallic regime. The formulation of an acceptable theoretical description of the MIT in such materials is still pending.

We approach the problem within an effective model, using the well-known Anderson model to describe the dynamics of the electrons inside the impurity band formed by the donor states. The presence of a finite concentration of local magnetic moments is approximated by an exchange coupling to classical magnetic impurities. The effects of Heisenberg impurities are compared with those of Ising impurities. The results are obtained numerically, based on a finite-size scaling analysis of the typical density of states, which is the geometric average of the local density of states. The latter is calculated by means of the kernel polynomial method, which allows for an efficient estimation of spectral quantities.

The results show that the critical value W_c of the site-diagonal disorder amplitude is a monotonically decreasing function of the exchange coupling strength J in the case of Ising impurities. In the presence of Heisenberg impurities, W_c is first enhanced with increasing J, before it eventually decreases as well. The difference in behavior can be explained by a change of symmetry from orthogonal to unitary, caused by the Heisenberg impurities. The scaling of W_c with J is analyzed and compared to analytical predictions.

Contents

1. Introduction

In this thesis, the effects of local magnetic moments on the Anderson metal-insulator transition (AMIT) are investigated. The AMIT is a continuous (second order) quantum phase transition from a metallic to an insulating phase, induced by disorder [BK94]. The DC conductivity is thereby expected to vanish beyond a critical amount of disorder, or if the density of states (DOS) around the Fermi energy is sufficiently low. The prefix "quantum" distinguishes this kind of phase transition from conventional, thermally driven phase transitions known from thermodynamics, as the AMIT occurs at zero temperature, driven merely by quantum fluctuations [BK94].

In solids, disorder can manifest itself in various forms: The most prominent is *substitutional disorder*, where a certain fraction of the host atoms are replaced by those of another element, forming an alloy with two or more components [Jun10]. This can either be achieved on purpose to control the electronic properties of a material (doping), or represent natural imperfection (impurities). Other forms of disorder include *interstitial disorder* (atoms at interim positions of the crystal lattice) and *structural disorder* (vacancies, adatoms, glasses). Depending on the type, parameters controlling the amount of disorder may be given by the concentration of dopants, impurities or vacancies, or by the range and shape of a probability density function that assigns random values to a disorder potential or a transfer matrix element.

The occurrence of a metal-insulator transition (MIT) is explained by the nature of the electronic eigenstates near the Fermi energy. Following basic solid state theory, the problem of free electrons moving in a strictly periodic potential is solved by the *Bloch theorem* [AM76] (see section 2.1). The solutions for the electronic eigenstates are known as *Bloch waves*, which are called *extended* in the sense that they feature a non-zero wave function intensity (WFI) throughout the crystal, similar to plane waves. Extended eigenstates allow the electron to travel to the far edge of the crystal, thus contributing to the conductance of the specimen. This picture constitutes the fundamental explanation for the good electronic transport properties of metals.

As soon as there are deviations from the periodic symmetry of the potential, caused for example by the existence of impurities, the Bloch theorem no longer applies. In fact, pure crystals are rather the exception in nature than the rule [LT85]. Small amounts of disorder may however still be treated within perturbational approaches [LT85]. Within the picture of the classical *Drude theory* [AM76], impurities cause the electronic wave functions to scatter, reducing their mean free path, and hence the resistivity of the material receives a positive *weak localization correction*, as illustrated in figure 1.1. The motion of the electron becomes thereby *diffusive*. Also *weak antilocalization corrections* are known, for example in systems with symplectic symmetry (see section 2.4).

However, going beyond the *weak localization* regime, the classical picture has proven

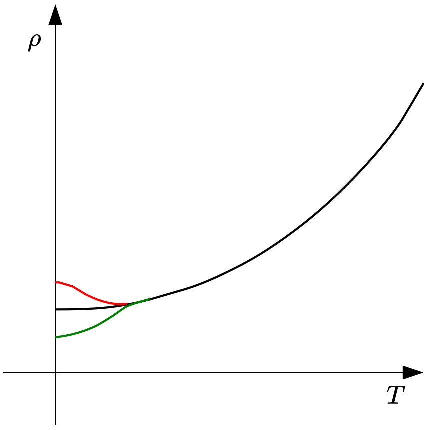

Figure 1.1.: Illustration of weak localization (red) and weak antilocalization corrections (green) to the resistivity ρ for small temperatures.

to be insufficient to explain certain experimental data, which indicates the complete suppression of the conductivity beyond a critical amount of disorder. Anderson was among the first to realize that facing *strong disorder* (or in energy regions of sufficiently low DOS), the quantum-mechanical nature of the electron has to be taken into account for a correct understanding of the phenomenon. In his description, the coherent backscattering of the wave function amplitudes can cause *localization* of the electronic wave functions through interference [And58]. In other words, an electron occupying a *localized state* is confined to a certain region within the crystal and can no longer travel freely through the material. The number of eigenstates that contribute to the conductivity is thereby reduced.

The phenomenon of localization exists already in classical terms, for a particle may be trapped within the tails of a fluctuating potential landscape, as illustrated in figure 1.2. However, the quantum-mechanical treatment allows for two additional effects that turn out to be essential for the description of electron wave function localization: *Tunneling*, and *constructive interference* [KM93]. Tunneling allows the electron to overcome certain potential barriers which in classical terms would be insurmountable. On the other hand, constructive interference can cause certain classically extended states to be localized in effect.

While the localization mechanism of electronic wave functions and the complete suppression of electron diffusion due to disorder has been generally accepted by the scientific community, there is an ongoing debate about the order of the phase transition [MFT99]. Among others, Mott argues that the transition should be of first order [Mot68, Mot72, Mot90], implying a discontinuity of the conductivity at the critical point. At first, this was supported by some experimental evidence. But since the one-parameter *scaling theory of localization* (see section 2.3) has been formulated [Abr79], it is widely accepted that the AMIT is of second order, so that the conductivity changes continuously across the critical point. Furthermore, these findings are compatible with a field-

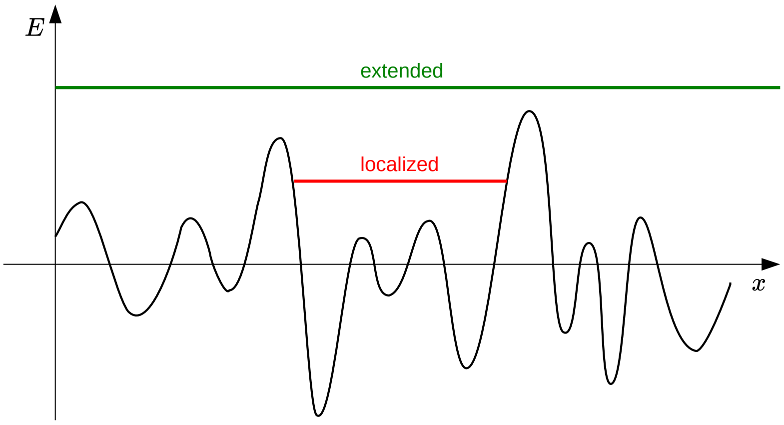

Figure 1.2.: Illustration of a classically extended (green) and a classically localized state (red) in a fluctuating 1D potential landscape.

theoretical description in terms of the *non-linear sigma model* [Weg86, Weg87a, Weg87b], which results in many useful relations and estimates for the critical exponents.

Already earlier, a close relation between the localization problem and *random matrix theory* (RMT) has been established, from which a classification scheme regarding the symmetry properties of the random matrices is known. Since then it has been possible to distinguish different types of random systems by their symmetry properties, finding that the principle of *universality* applies to the properties of the MIT for systems of the same symmetry class (and with the same number of dimensions).

Another remarkable discovery has been the identification of multifractality in the electronic wave functions near the critical point [CP86, SG91, GS92]. It turns out that the wave function amplitudes follow a log-normal distribution. Meanwhile, theorists have established a powerful method to identify the properties of a MIT by observing the multifractal behavior of the wave functions, commonly known as *multifractal analysis* (MFA) [VRR08, RVR08, RVR09, RVSR10, RVSR11]. The multifractal properties of the electronic states also play a crucial role in the present thesis (see chapter 4).

This sums up the most important theoretical findings that have been obtained since the original formulation of the problem of localization over five decades ago. It is however still a highly active field of research, mainly because there exists to date no satisfying theory providing a thorough explanation of the localization mechanism observed in many real materials, which leads to a MIT. Due to the lack of analytic predictions, the problem of localization relies heavily on numerical simulations [Nob77]. But even then it seems difficult to account for the various effects which may play a crucial role in the real material, without neglecting vital ingredients. For example, electron-electron interaction is often neglected, which can cause a localization scheme by itself, leading to the *Mott-Hubbard transition* [Mot67, Mot68]. Also the present thesis has to describe the problem using an approximative picture, picking only one aspect out of the problem: To examine the effects of local magnetic moments on the AMIT.

A variety of experimental studies have been performed to analyze the transition from metallic to insulating behavior in real materials [LT85, BK94, vL00, LvTW09]. The present thesis lays focus on phosphorus-doped silicon (Si:P). Some key results of Si:P are reviewed in section 2.6, as well as a clarification of the physical situation leading to the MIT. In short, a rising concentration of P-dopants increases the amount of charge carriers, thus increasing the conductivity, but also increases the amount of disorder. The strong Coulomb repulsion splits the impurity band formed by the dopant levels into two Hubbard sub-bands and favors single occupancy of the localized dopant states, which are distributed randomly throughout the system [vL00]. This gives rise to local magnetic moments [Sac89, vL98, vL00], which further complicate the description of the MIT in this material.

We study the influence of local magnetic moments on the AMIT within an effective model for the impurity band electrons. The model is based on the well-known Anderson model [And58], extended by a term describing a local exchange coupling to magnetic spin-1/2 impurities. The influences of two kinds of impurities on the AMIT are compared, *Heisenberg impurities* and *Ising impurities*, both in a semi-classical treatment. The dependence of the critical disorder on the exchange coupling strength is analyzed and compared to analytic predictions. Also some qualitative results for the influence of local magnetic moments on the complete phase diagram in the disorder-energy plane are obtained.

To analyze the MIT, a finite-size scaling (FSS) approach for the geometric average of the local density of states (GLDOS) is used [ASO06]. The *local density of states* (LDOS) can efficiently be calculated within the *kernel polynomial method* (KPM) [WWAF06]. The KPM is a polynomial expansion technique using Chebychev polynomials (see section 3.2). Spectral quantities like the LDOS can be calculated directly, without the need to obtain the actual eigenspectrum of the system. Despite its abilities, the KPM has not yet received appreciable attention in the physics community. We shall therefore explain it to a certain level of detail in section 3.2. We extend KPM approaches by others [SF09] by combining it with the FSS analysis.

After this general introduction to the problem of electron localization and the MIT in doped semiconductors, chapter 2 will further illuminate some key aspects fundamental to our analysis. Then, in chapter 3, the numerical methods used to obtain the results are explained. The FSS approach is introduced in chapter 4. In chapter 5, the studied model is introduced and the main results are presented. Some concluding remarks are made in chapter 6.

2. Anderson metal-insulator transitions: Fundamentals

This chapter reviews some essential aspects regarding metal-insulator transitions (MIT), which are fundamental to our analysis. Readers unfamiliar with the concept of effective tight binding models (ETBM) find a brief introduction into a class of simple ETBM in section 2.1[1]. It is instructive to introduce the basic properties of such models in the absence of disorder, before they are extended by random components in section 2.2. Fundamental to any finite-size scaling (FSS) approach is certainly the scaling theory of conductivity [Abr79], which is briefly reviewed in section 2.3. The symmetry classification of the Hamiltonian considered in the present thesis plays an important role for the interpretation of the results, so it seems natural to introduce the Wigner-Dyson classification scheme [Dys62] (section 2.4). The multifractal properties of electron states near the MIT have to be considered in the FSS approach, so basic assumptions of multifractal analysis (MFA) are examined in section 2.5. The physical situation leading to the MIT in doped semiconductors like phosphorus-doped silicon (Si:P) is illuminated in section 2.6, where also some key experimental results for Si:P are mentioned.

2.1. Effective tight binding models

A class of simple effective tight binding model (ETBM) Hamiltonians shall be introduced, which are popular for both numerical and analytical investigations throughout solid state theory. They describe the dynamics of a single particle (for example an electron) at zero temperature ($T = 0\,\mathrm{K}$) in a (possibly random) potential. Hence, no thermal effects and no electron-phonon interaction are considered. The Hamiltonian possesses only two terms, one corresponding to the potential energy and the other to the the kinetic energy of the particle. Electron-electron interaction is neglected as well, which would require a many-body description.

The Hamiltonian is most conveniently written in a basis of states each localized at a lattice site, which is referred to as the *site-diagonal basis* in the following. In one-band models without spin, there is only one state per lattice site (including the spin of the electron, there are two). So the Hamiltonian possesses $N_\mathrm{k} = N$ eigenstates, where N is the number of lattice sites ($N_\mathrm{k} = 2N$ if the electron spin is considered). Each state can be occupied by the electron. The site-potential ε_i, located at site i, is related to the probability that the electron is occupying a state located at that particular site. The

---

[1] Beyond this, the reader is referred to more general introductions to condensed matter theory [AM76, Czy08].

general form of such a one-band Hamiltonian is

$$\hat{H} = \sum_i \varepsilon_i \left|i\right\rangle \left\langle i\right| + \sum_{\langle i,j \rangle} t_{ij} \left|i\right\rangle \left\langle j\right| \quad . \tag{2.1}$$

To describe a system without site-diagonal disorder, the site potentials ε_i are constant, $\varepsilon_i = \varepsilon$, and can be chosen to $\varepsilon = 0$ without loss of generality. This has also the advantage of highlighting the symmetric nature of the energy spectrum of tight binding Hamiltonians when the potential possesses inversion symmetry [Czy08]. The continuous-space form of the potential, $\tilde{\varepsilon}(\mathbf{r})$, is then a periodic function, i.e. it is invariant under shifts by lattice vectors $\mathbf{R}$,

$$\tilde{\varepsilon}(\mathbf{r}) = \tilde{\varepsilon}(\mathbf{r} + \mathbf{R}) \quad . \tag{2.2}$$

In other words, a lattice-periodic $\tilde{\varepsilon}(\mathbf{r})$ correspons to constant site-potentials $\varepsilon_i = \varepsilon$.

By the second term, the electron is allowed to switch to another state, located at another lattice site. In this way, the motion of the electron through the crystal is accomplished by *hopping transport*. For systems without off-diagonal disorder, a constant hopping amplitude $t_{ij} = t$ is considered, which allows hopping from site to site with a probability proportional to $|t|^2$. t may serve as the energy scale for all other energetic quantities[2]. In this simple class of ETBM, the hopping amplitude is only non-zero for matrix elements connecting neighboring lattice sites (nearest neighbor approximation, NN). It is immediately clear that in a d-dimensional hypercubic system, there are $Z = 2d$ nearest neighbors.

The one-particle eigenfunctions and eigenenergies of the Hamiltonian (2.1) are generally given by the time-independent Schrödinger equation,

$$\hat{H}\psi_{\mathbf{k}}(\mathbf{r}) = E_{\mathbf{k}}\psi_{\mathbf{k}}(\mathbf{r}) \quad . \tag{2.3}$$

If there is no disorder in the system, i.e. the potentials ε_i and hoppings t_{ij} are constant, the solutions $\psi_{\mathbf{k}}(\mathbf{r})$ fulfill the *Bloch condition* [Czy08]

$$\psi_{\mathbf{k}}(\mathbf{r} + \mathbf{R}) = \mathrm{e}^{i\mathbf{k}\cdot\mathbf{R}}\,\psi_{\mathbf{k}}(\mathbf{r}) \quad . \tag{2.4}$$

One has to consider a finite sample with periodic boundary conditions (PBC) in order to normalize the eigenfunctions,

$$\psi_{\mathbf{k}}(\mathbf{r}) = \psi_{\mathbf{k}}(\mathbf{r} + N_i\mathbf{a}_i) \quad , \quad \mathrm{N_i} > 0 \quad , \quad \mathrm{i} \in \{1, 2, \ldots, \mathrm{d}\} \quad , \tag{2.5}$$

where $\mathbf{a}_i$ are the basis vectors spanning the conventional unitcell. Formally, only then the eigenfunctions $\psi_{\mathbf{k}}(\mathbf{r})$ and eigenenergies $E_{\mathbf{k}}$ can be classified by the crystal momentum $\mathbf{k}$, the values of which can be taken entirely from the first Brillouin zone (1BZ). The eigenfunctions itself are of the form

$$\psi_{\mathbf{k}}(\mathbf{r}) \sim \mathrm{e}^{i\mathbf{k}\cdot\mathbf{r}} u_{\mathbf{k}}(\mathbf{r}) \quad , \tag{2.6}$$

---

[2] We will refer to the values of many energetic quantities as multiples of t. This corresponds to setting $t = 1$ in numerical simulations.

Table 2.1.: List of important symmetry points of simple cubic crystal structures and their coordinates within the first Brillouin zone [SW82].

Name	$\mathbf{k}$
Γ	$(0,0,0)$
X	$(\frac{\pi}{a},0,0)$
M	$(\frac{\pi}{a},\frac{\pi}{a},0)$
R	$(\frac{\pi}{a},\frac{\pi}{a},\frac{\pi}{a})$

which are called *Bloch waves*, and $u_{\mathbf{k}}(\mathbf{r})$ are the lattice-periodic *Bloch factors* modulating the wave [Czy08]. So in essence, all eigenstates of a non-disordered tight binding system are *extended*, similar to plane waves. An extended state lets an electron travel to the far edge of the crystal and hence contributes to the conductivity of the system.

Following the usual approach within the tight binding approximation, the (one-band) energy dispersion is given by [Czy08]

$$E(\mathbf{k}) = E_0 + t \sum_{\mathbf{R}} \mathrm{e}^{-i\mathbf{k}\cdot\mathbf{R}} \quad , \tag{2.7}$$

where t is the abovementioned *hopping parameter* and the lattice vectors $\mathbf{R}$ are limited here to those pointing to the neighboring lattice sites (nearest neighbor approximation). If the potentials ε_i are set to zero, also $E_0 = 0$. Evaluating (2.7) explicitely for a three-dimensional tight binding system yields the characteristical cosine-like dispersion relation [Czy08]

$$E(\mathbf{k}) = -2t\left(\cos(k_1 a) + \cos(k_2 a) + \cos(k_3 a)\right) \quad , \tag{2.8}$$

where a is the lattice spacing. The dispersion (2.8) is plotted in figure 2.1 along straight lines through important symmetry points within the 1BZ (see table 2.1). According to equation (2.8), on a d-dimensional hypercubic lattice with Z nearest neighbors, the bandwidth is

$$D = 2Zt = 4dt \quad , \tag{2.9}$$

which can also be verified by a numerical calculation[3] of the *density of states* (DOS) $\rho(E)$ in figure 2.2 for $d = 3$.

The DOS of a finite system with discrete eigenenergies E_k is defined as [WWAF06]

$$\rho(E) = \frac{1}{N_\mathrm{k}} \sum_k \delta(E - E_k) \quad , \tag{2.10}$$

where k is an index labeling the eigenstates, and N_k is their number. If E is substituted by the dispertion relation (2.8), the characteristic DOS of a three-dimensional one-band nearest neighbor tight binding Hamiltonian without disorder (2.1) is obtained, as depicted in figure 2.2. It features a squareroot-like behavior at the band edges,

---

[3] The source code used to obtain the figure is shown as an example in appendix B.

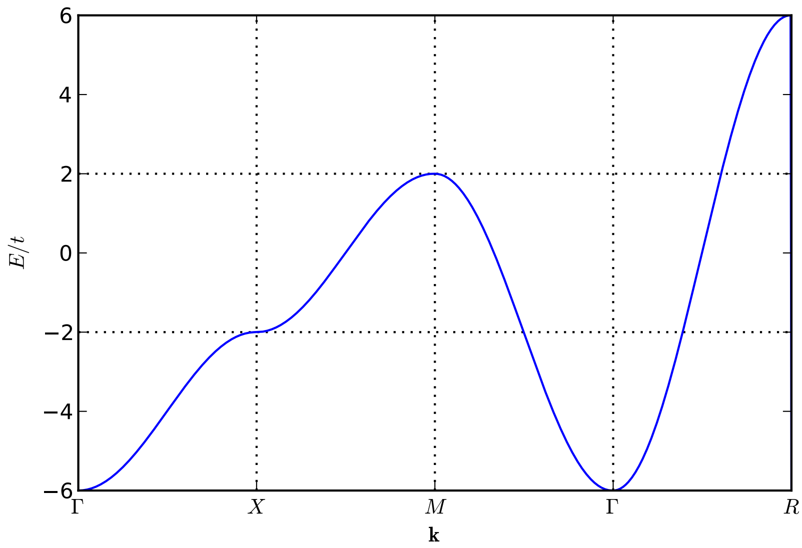

Figure 2.1.: Energy dispersion $E(\mathbf{k})$ (2.8) (band structure) of a non-disordered three-dimensional one-band nearest neighbor tight binding system along selected symmetry lines through the first Brillouin zone. The symmetry points are listed in table 2.1.

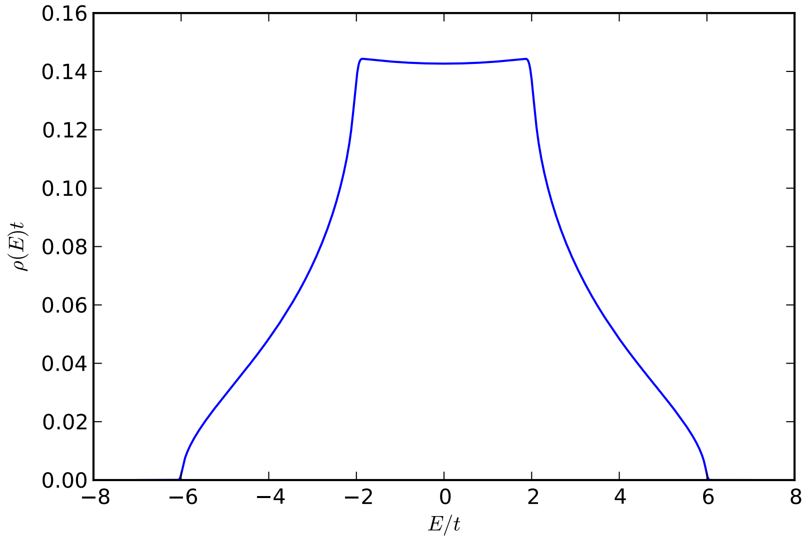

Figure 2.2.: Density of states of a non-disordered three-dimensional one-band nearest neighbor tight binding Hamiltonian (2.1), for a system size of $N = L^3 = 100^3$ and using $M = 350$ Chebychev moments for the kernel expansion (3.3). The source code used to obtain this figure can be found in appendix B.

$\rho(E) \sim \sqrt{E}$, which is characteristical for the DOS of a 3D material [AM76]. Also visible are the *Van-Hove singularities* at energies $E/t = \{-6, -2, 2, 6\}$, which are characteristic for a non-disordered system and exist due to highly degenerate eigenstates at certain symmetry points in **k**-space. At those energies, the energy dispersion $E(\mathbf{k})$ has a slope equal to zero (cf. figure 2.1).

2.2. Disordered systems: The Anderson model

Some of the simplest models for investigating the effects of disorder are variants of the Hamiltonian (2.1), giving up the constant nature of at least one of the parameters t_{ij} or ε_i, and replacing it by random variates, drawn from some probability distribution. If the site potentials are drawn from a continuous uniform probability distribution of finite width W (*box distribution*),

$$\mathcal{P}_{\mathrm{B}}(\varepsilon_i) = \frac{1}{W}\,\Theta\left(\frac{W}{2} - |\varepsilon_i|\right) \quad , \tag{2.11}$$

while the hopping parameters remain constant, the Hamiltonian (2.1) is known as the *Anderson model* [And58],

$$\hat{H} = \sum_i \varepsilon_i \left|i\right\rangle \left\langle i\right| + t \sum_{\langle i,j \rangle} \left|i\right\rangle \left\langle j\right| \quad . \tag{2.12}$$

The width W of the interval from which the site potentials are drawn is a measure for the disorder strength. For $W = 0$, the non-disordered tight binding Hamiltonian is recovered, and the resulting DOS is shown in figure 2.2. As soon as W is increased, the DOS starts to broaden, and because of normalization, its value at the band center ($E = 0$) is shrinking, as shown in figure 2.3. Being a one-band model, and neglecting any kind of thermal effects or interactions, the Anderson model assures that a transition to insulating behavior can only be due to a transformation of the character of the wavefunctions at the Fermi energy, and not because of the emergence or shift of band gaps [Mil00].

For $W > 0$, the system loses its periodic symmetry. For *weak disorder* (small disorder values W), deviations from the Bloch theory reviewed above can sometimes still be taken into account perturbatively [BK94]. However, for larger disorder values W, the eigenstates can no longer be classified by the crystal wave vector **k**, and are not of Bloch type (2.6) anymore[4]. Bloch theory is no longer applicable. The energy dispersion (2.7) (band structure) becomes meaningless, as the energy levels are now distributed randomly and are fluctuating throughout the lattice. As a consequence, the van-Hove singularities in the DOS "smear out" (cf. figure 2.3), as the degenerate eigenstates of the non-disordered system dissolve into a band of random energy levels [Jun10].

From (2.9) and (2.11) it is immediately clear that the theoretical band edges (the *Lifshitz boundaries*) depend on the disorder strength W like [KM93]

$$\left[-Zt - \frac{W}{2}, Zt + \frac{W}{2}\right] \quad , \tag{2.13}$$

---

[4] Still, we use the index k in the following to label the different eigenstates of a system.

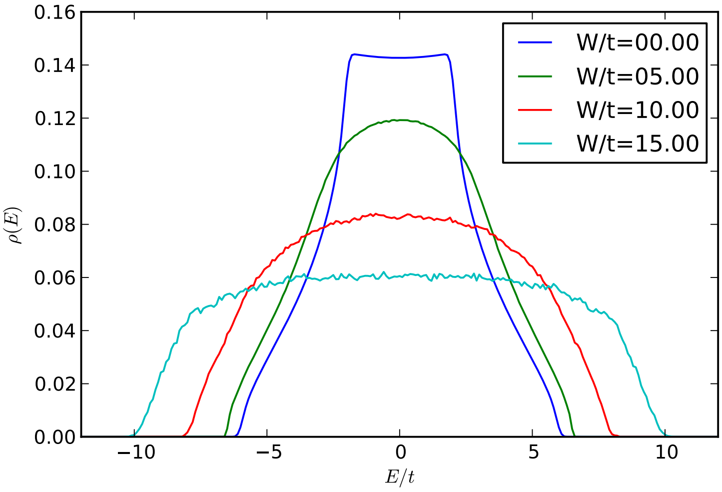

Figure 2.3.: Density of states of the Anderson model (2.12) for different values of the disorder parameter W. The system size is $L = 50$, and the number of Chebychev moments (see section 3.2) is $M = 6250$ (for $W = 0$, it is $M = 625$).

with $Z = 2d$ in hypercubic systems. However, as numerical calculations do usually not cover *rare events*, i.e. extremal eigenvalues in the band tails that occur only with vanishing probability in a sample, the numerical bandwidth as shown in figure 2.3 is usually smaller than the theoretical boundaries (2.13).

The Anderson model (2.12) describes the dynamics of an electron in a disordered potential at zero temperature, $T = 0\,\mathrm{K}$. Its relevance is due to the absense of any other mechanisms that could be responsible for localizing the wave functions, like interactions (Mott transition) or thermal effects [KM93]. Hence, the disorder-induced metal-insulator transition (MIT), which is called *Anderson metal-insulator transition* (AMIT) accordingly and occurs at some nonzero critical disorder strength W_c in $d > 2$ dimensions, can be thoroughly analyzed.

2.2.1. Other choices for the disorder potential

Typically, the random potentials ε_i are drawn from a uniform continuous probability distribution (2.11) (also known as a box distribution of width W), but other choices can be justified as well [KM93], as for example a normal (Gaussian) distribution,

$$\mathcal{P}_\mathrm{N}(\varepsilon_i) = \frac{1}{\iota\sqrt{2\pi}} \exp\left(-\frac{\varepsilon_i^2}{2\iota^2}\right) \tag{2.14}$$

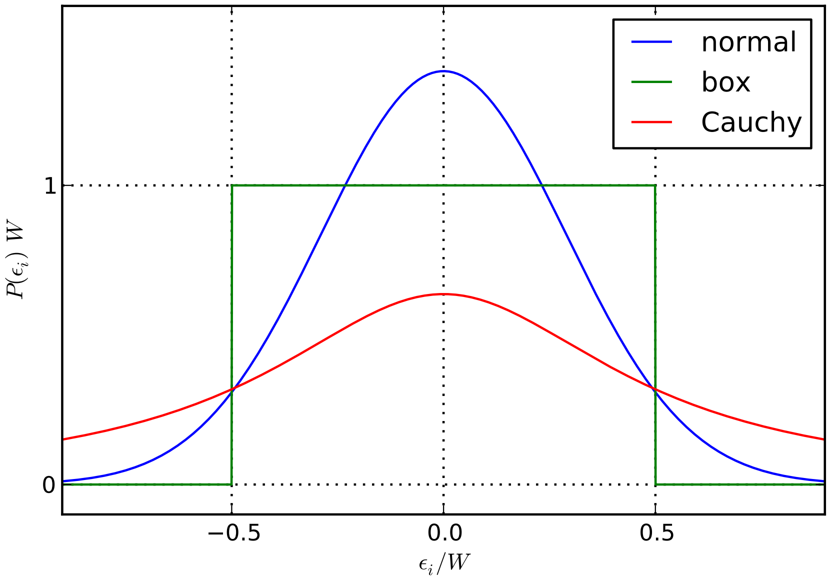

Figure 2.4.: The probability density functions of the box distribution (2.11), the normal distribution (2.14) and the Cauchy distribution (2.15), rescaled by (2.17) and (2.18).

or a Lorentz (Cauchy) distribution [BSK87],

$$\mathcal{P}_{\mathrm{L}}(\varepsilon_i) = \frac{\zeta}{\pi(\varepsilon_i^2 + \zeta^2)} \quad , \tag{2.15}$$

each leading to another shape of the phase trajectory in the energy-disorder plane (see figure 2.6). The probability density functions (PDF) of the three distributions are compared in figure 2.4. To investigate the more realistic case of a disordered alloy, one could also consider a discrete probability distribution for the ε_i. The simplest is given by the binary distribution,

$$\mathcal{P}_{\mathrm{A}}(\varepsilon_i) = \frac{(1-x)\,\delta(\varepsilon_i - \varepsilon_{\mathrm{A}}) + x\,\delta(\varepsilon_i - \varepsilon_{\mathrm{B}})}{2} \quad , \tag{2.16}$$

where a concentration x of B-atoms within a host material of A-atoms is described. In this case, two bands may form, depending on the two disorder-influencing parameters, the value of x and the energy difference $|\varepsilon_{\mathrm{A}} - \varepsilon_{\mathrm{B}}|$.

To make the resulting phase diagrams corresponding to different continuous probability distributions comparable, it is important to scale them in a way so that their standard deviations agree [Sch85]. To compare the normal distribution (2.14) to the box distribution (2.11), the parameters W and ι are thus related by [BSK87]

$$W = \iota\sqrt{12} \quad . \tag{2.17}$$

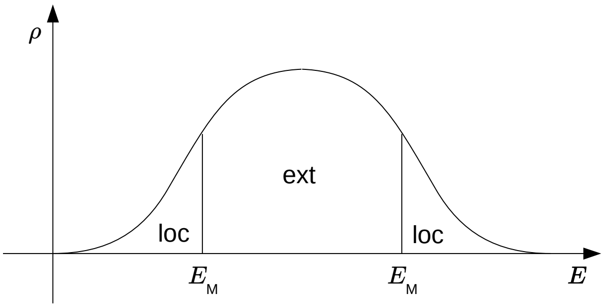

Figure 2.5.: Illustration of the concept of mobility edges E_{M} in a schematic plot of the density of states ρ.

For the Cauchy distribution (2.15), the standard deviation is not defined. Instead, its *half width at half maximum* (HWHM) value can be adjusted to that of the box distribution (2.11) [BSK87], which yields

$$W = 2\zeta \quad . \tag{2.18}$$

2.2.2. Mobility edges

As soon as disorder is introduced, a certain fraction of the eigenstates of the system will not be *extended* anymore, but *localized*. The general picture is that an electron occupying a localized state is confined to a certain region of the crystal, so it cannot travel around freely and hence cannot contribute to the conductivity of the material. At a critical amount of disorder, all states will be localized, and the material becomes an insulator. This transition is known as the *Anderson metal-insulator transition* (AMIT).

It has been proven that at a certain energy within the spectrum, either all states are extended or all states are localized [KM93]. There can be no mixture of localized and extended states at a particular energy. It turns out that the localized states are grouped together in the band tails, or more precisely, in band regions of low density of states (DOS). The critical energies dividing such regions of localized states and regions of extended states in the energy band are called *mobility edges* E_{M} [Mot67]. They bound the energy regions outside of which the electrons are immobalized. The sketch in figure 2.5 illustrates the concept of mobility edges. Due to the simple shape of the DOS in the Anderson model, only two mobility edges exist. They vanish above the critical disorder W_{c}, where they collapse in the band center, and only localized eigenstates remain.

The existence of mobility edges can be understood by the following considerations [KM93]: States deep in the tails of an electronic band are expected to have the greatest chance to become localized for increasing disorder, as they are formed from localized orbitals bound in the deepest valleys of the potential fluctuations. In the band center, the chance for a state to remain extended with increasing disorder is greatest, as there are still enough orbitals with similar energy to overlap with. If the Fermi energy E_{F} lies in a region of localized states, the conductivity vanishes in the limit of zero temperature, whereas in the metallic regime, it approaches some positive value. The mobility edges mark the transition from metal to insulator if not the disorder but instead the energy is varied.

2.2.3. The phase diagram of disorder

As the disorder parameter is increased in the Anderson model (2.12), the mobility edges move towards the center of the band, until at a critical disorder W_c, they finally collapse in the center of the band, and the entire band consists of localized states. This point marks the AMIT at half filling ($E_\mathrm{F} = 0$). It is common to depict the AMIT in the *phase diagram of disorder*, which shows the *phase trajectory* in the disorder-energy plane (see figure 2.6). It can be viewed as a visualization of the disorder-dependence of the mobility edges E_M, or the other way around, as a visualization of the energy dependence of the critical disorder W_c.

It should be pointed out that in general, there might exist more than one system parameter influencing the amount of disorder, so the phase diagram might become multidimensional. It is then favourable to show only a slice of the complete phase diagram, which can then be presented in a 2D plot like figure 2.6. Examples are our phase diagrams for constant exchange coupling J and constant impurity concentration n_M in section 4.4. Figure 2.6 shows the phase trajectories for the three abovementioned continuous PDF for the site potentials ε_i [BSK87], as well as the value of the critical disorder strength W_c for each case.

For the two PDF that possess a well-defined standard deviation (normal and box distribution), the so-called *reentrance behavior* is observed: There are energy regions (here: $\left|E/t\right| > 6$) in which the phase trajectory is crossed twice for increasing W: From localized to extended and then again from extended to localized. This is not observed for the Cauchy distribution (2.15), which decays very slowly for $E \to \infty$ and hence does not lead to a sharply measurable band edge. Even for energies far away from the band center, the probability to find an eigenvalue is still appreciably different from zero.

It should be noted that by introducing random parameters in the Hamiltonian (2.12), all physical quantities have to be statistically averaged over different disorder configurations [KM93] in all analytical and numerical investigations that consider systems with finite dimensions.

2.3. The scaling theory of conductivity

The theoretical understanding of the Anderson transition received a boost when Abrahams et al. formulated the *scaling theory of localization* [Abr79]. It assumes that the critical behaviour of the DC conductivity σ_DC and the localization length ξ_loc close to the transition can be described by only one *scaling variable* [KM93].

The theory consideres a generalized dimensionless conductance g,

$$g(L) = \frac{G(L)}{e^2/2\hbar} \tag{2.19}$$

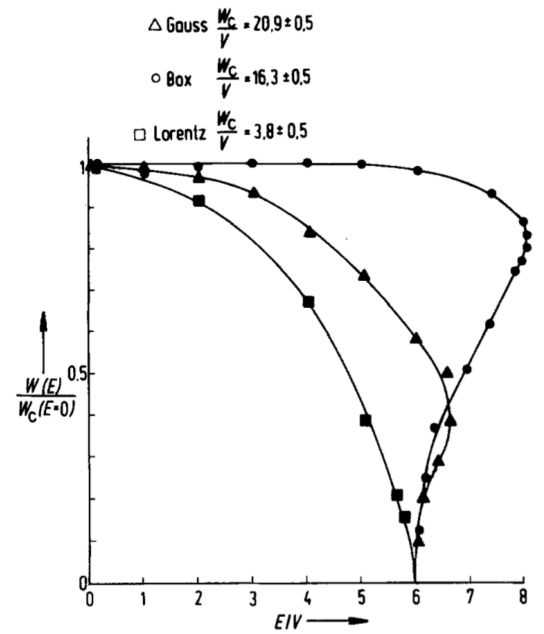

Figure 2.6.: Phase diagram of disorder for three different continuous probability distributions for the random site potentials ε_i. From [BSK87].

and defines the quantity

$$\beta(g(L)) = \frac{\mathrm{d}\ln g(L)}{\mathrm{d}\ln L} \quad , \tag{2.20}$$

which is sometimes called *Thouless number* [LT78]. L is the longitudinal system size of a d-dimensional hybercubic lattice with $N = L^d$ lattice sites (lattice constant $a \equiv 1$). g is understood as a measure for the amount of disorder here, being large when disorder is small, and conversely [LT85].

In the limit of large g (vanishing disorder), the classical relation between conductance G and conductivity σ_{DC} is recovered (given a cubic system, $N = L \times L \times L$):

$$G(L) = \sigma_{\mathrm{DC}} L^{d-2} \quad . \tag{2.21}$$

So for $\beta(g)$ it follows

$$\lim_{g \to \infty} \beta_d(g) = d - 2 \quad . \tag{2.22}$$

For small g (large disorder), the wavefunctions are assumed to be exponentially localized. The dimensionless conductance is then

$$g = g_{\mathrm{a}} e^{-\alpha L} \quad , \tag{2.23}$$

and $\beta(g)$ becomes

$$\lim_{g \to \infty} \beta_d(g) = \ln \frac{g}{g_{\mathrm{a}}(d)} \quad , \tag{2.24}$$

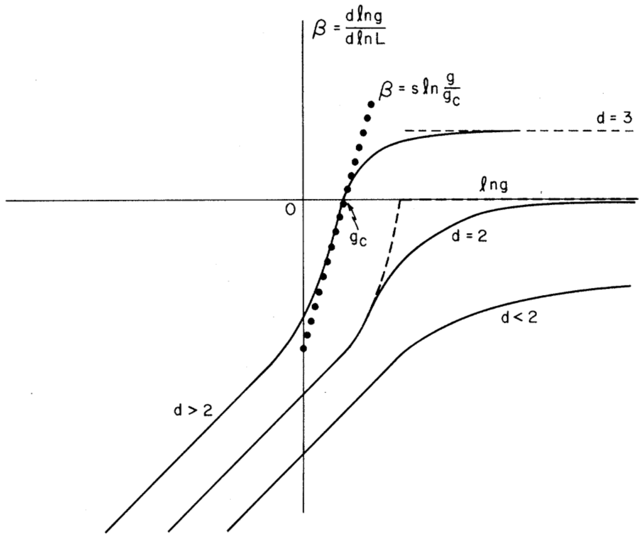

Figure 2.7.: The function $\beta(g)$ for 1D, 2D and 3D systems. From [Abr79].

with the constant $g_{\mathrm{a}} \approx 1$.

The curve $\beta(g)$ is sketched in figure 2.7 as a function of g for 1D, 2D and 3D systems. A positive value of β reflects a metallic scaling behavior, where the conductivity increases with system size L, while a negative value indicates the expected scaling behavior in the presence of localized states. Only the curve for systems with $d > 2$ dimensions crosses the x-axis at a critical value g_{c} (*fixed point*), indicating a phase transition from metal to insulator. This means that at least for systems belonging to the orthogonal symmetry class (see section 2.4), systems of lower dimensionality than $d = 3$ do not show an AMIT, which is one of the most important results of the scaling theory of localization.

The second important conclusion is that the Anderson transition is a second order phase transition. The localization length ξ_{loc} of a state is the exponential (asymptotic) decay length of its envelope [KM93, EM08],

$$\left|\psi^2(\mathbf{r})\right| \sim \mathrm{e}^{-\frac{|\mathbf{r}-\mathbf{r}_0|}{\xi_{\mathrm{loc}}}} \psi(\mathbf{r}) = f(r)\mathrm{e}^{-r/\xi_{\mathrm{loc}}} \quad . \tag{2.25}$$

In analogy with second-order phase transitions known from thermodynamics, the DC conductivity σ_{DC} (on the metallic side) and the localization length ξ_{loc} (on the insulating side) behave like

$$\sigma_{\mathrm{DC}} \propto (E - E_{\mathrm{M}})^{s} \tag{2.26}$$

$$\xi_{\mathrm{loc}} \propto |E - E_{\mathrm{M}}|^{-\nu} \tag{2.27}$$

near the mobility edge E_{M}. It has been confirmed that the two exponents s and ν are equal in three-dimensional systems [EM08]. This is consistent with *Wegner's scaling law*

[vL00],

$$s = \nu(d-2) \quad . \tag{2.28}$$

2.4. Symmetry classification of random systems

Based on the ideas of *random matrix theory* (RMT) [Wig51], Dyson introduced a classification scheme (*Wigner-Dyson scheme*) for ensembles of random Hamiltonians [Dys62]. It is immediately clear that RMT is closely related to the physics of disordered electronic systems, as the matrix representation of a random Hamiltonian contains random matrix elements. The Wigner-dyson scheme consideres the invariance of the system under time-reversal symmetry (TRS) and under spin symmetry, leading to three symmetry classes: *Orthogonal*, *unitary* and *symplectic* [EM08]. For fixed dimensionality d, Hamiltonians belonging to the same symmetry class share important features, especially do their critical exponents ν agree (*universality class*).

If the Hamiltonian is invariant under time-reversal and spin symmetry, as it is the case for the Anderson model (2.12), its matrix representation is a real symmetric matrix,

$$\hat{H} = \hat{H}^{\mathrm{T}} \quad . \tag{2.29}$$

The T here corresponds to the transpose of the matrix. Thus, it is said to belong to the *orthogonal symmetry class*, and the Hamiltonian to be invariant with respect to the orthogonal group $\mathrm{SO}(N)$.

If the Hamiltonian contains terms breaking TRS, for example describing the coupling to an external magnetic field or magnetic impurities, the matrix representation will contain complex matrix elements. Hence, the matrix becomes hermitian,

$$\hat{H} = \hat{H}^{\dagger} \quad . \tag{2.30}$$

So the Hamiltonian is invariant with respect to the unitary group $\mathrm{SU}(N)$. This is the case for our effective model (5.2) for a non-zero exchange coupling, $J > 0$.

If the Hamiltonian breaks spin-rotation symmetry, for example by introducing spin-orbit coupling, but does not break TRS, it belongs to the *symplectic symmetry class*, so that its matrix representation fulfills the symmetry relation

$$\hat{H} = \sigma_{\mathrm{y}} \hat{H}^{\mathrm{T}} \sigma_{\mathrm{y}} \quad . \tag{2.31}$$

σ_{y} is the second Pauli matrix (5.3). The Hamiltonian is then invariant with respect to the symplectic group $\mathrm{Sp}(2N)$. Even 2D systems can show a metal-insulator transition if they belong to the symplectic class [ASO04, ASO06].

Not all disordered electronic systems conform to one of the three Wigner-Dyson classes (only if a constant energy shift does not alter the dynamics of the system). Examples have been found which fall into different, “non-conventional” symmetry classes, like *chiral classes* and *Bogoliubov-de-Gennes classes* [EM08].

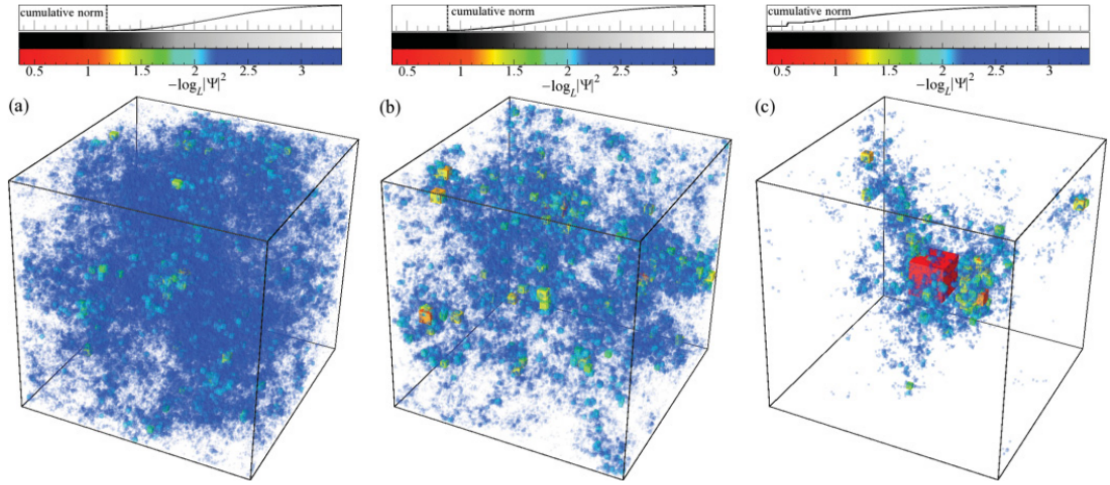

Figure 2.8.: Examples for numerically calculated wave functions of the Anderson model (2.12) near the band center $E = 0$ on large lattices $L = 120$. (a) An extended state, $W/t = 15$. (b) A critical state, $W/t = 16.5$. (c) A localized state, $W/t = 18$. The volume of the small cubes is proportional to $|\psi|^2$, their color and opacity is proportional to $-\log_L|\psi^2|$. With kind permission of the authors [RVSR11].

2.5. Multifractal behavior of critical states

It has been found that at the critical point of the AMIT, the wave functions show multifractal behavior [CP86, SG91, GS92]. This means that scaling exponents depend on the moment q of the wave function intensity (WFI), $\langle|\psi_{\mathbf{k}}(r)|^{2q}\rangle$. The moments are closely related to the generalised *inverse participation ratios* (IPR) [EM08, Jun10],

$$P_q = \int \mathrm{d}^d\, r\, |\psi(r)|^{2q} \quad , \tag{2.32}$$

so that

$$\langle P_q \rangle = L^d \left\langle |\psi(r)|^{2q} \right\rangle \quad , \tag{2.33}$$

where the angle brackets $\langle \ldots \rangle$ represent the ensemble average. It has been found that the IPR show an *anomalous scaling behavior* at criticality,

$$\langle P_q \rangle \sim L^{-\tau_q} \quad . \tag{2.34}$$

The τ_q are sometimes called *mass exponents* and represent a continuous set of exponents. Figure 2.8b shows an example of a critical eigenstate of the Anderson model (2.12) which shows multifractal behavior. Using *multifractal analysis* (MFA), the MIT can be studied in great detail, yielding the critical parameters with high precision [RVSR11].

One can introduce *fractal dimensions* D_q via [EM08]

$$\tau_q = D_q(q-1) \quad . \tag{2.35}$$

A perfectly extended state (similar to a plane wave) has $D_q = d$, and a perfectly localized state $D_q = 0$, i.e. there is no q-dependence and hence no multifractality. Near the critical point, D_q is a function of q with values between 0 and d, so the wave functions are showing multifractal behavior. It can be helpful to “split off” the normal dimensions d from the *anomalous dimensions* Δ_q [EM08], by defining

$$\tau_q = d(q-1) + \Delta_q \quad . \tag{2.36}$$

By definition, $\Delta_0 = \Delta_1 = 0$ [EM08].

2.5.1. The singularity spectrum

The singularity spectrum $f(\alpha)$ is the Legendre transform of the mass exponents[5] $\tau(q)$ [EM08],

$$\tau(q) = q\alpha_q - f(\alpha_q) \quad , \quad \alpha_\mathrm{q} = \frac{\mathrm{d}\tau(\mathrm{q})}{\mathrm{dq}} \quad . \tag{2.37}$$

From basic properties of the Legendre transformation it follows

$$q = \frac{\mathrm{d}f(\alpha_q)}{\mathrm{d}\alpha_q} \quad . \tag{2.38}$$

In the following, the index q of the quantity α_q is not written explicitely. Nevertheless it should be remembered that α is related to q via the Legendre transform (2.37). α is also the negative ratio of the logarithmic WFI and the logarithmic system size L [EM08],

$$\alpha = -\frac{\log|\psi|^2}{\log L} \quad . \tag{2.39}$$

It is important to understand the meaning of the singularity spectrum: $f(\alpha)$ is the fractal dimension of those points $\mathbf{r}$ in space where the WFI scales like [EM08]

$$\left|\psi(\mathbf{r})\right|^2 \sim L^{-\alpha} \quad . \tag{2.40}$$

At every point $\mathbf{r}$ of the system (e.g., the sites of a lattice), the WFI of a critical state may scale with another exponent α. There is a whole distribution of values α, each corresponding to another fractal dimension $D_q \in [0, d]$. For an insulator, $D_q = 0$, so the singularity spectrum should become one with the x-axis, $f(\alpha) = 0$ for all α. Another viewpoint is that on a lattice, the number of lattice sites where (2.40) is fulfilled is equal to $L^{f(\alpha)}$ (for a lattice spacing $a \equiv 1$) [EM08].

---

[5] As the mass exponents τ_q form a continuous set of exponents, they can be regarded as a continuous function of q.

2.5.2. Weak multifractality limit

In the weak multifractality limit, the anomalous dimensions can be approximated as [EM08]

$$\Delta_q \approx \gamma q(q-1) \quad , \quad \gamma \ll 1 \quad , \tag{2.41}$$

so that the mass exponents become

$$\tau_q \approx d(q-1) - \gamma q(q-1) \quad . \tag{2.42}$$

Via the Legendre transformation (2.37) it follows

$$f(\alpha) \approx d - \frac{(\alpha - \alpha_0)^2}{4(\alpha_0 - d)} \tag{2.43}$$

and

$$\alpha_0 = d + \gamma \quad . \tag{2.44}$$

So in the weak multifractality limit, the singularity spectrum is exactly parabolic, with the maximum at the point (α_0, d). The distribution of α is then [KMV09]

$$P(\alpha) = L^{-\frac{(\alpha-\alpha_0)^2}{4(\alpha_0-d)}} \quad . \tag{2.45}$$

Figure 2.9 shows a schematic plot of the singularity spectrum in the weak multifractality limit. For a perfect metal, the singularity spectrum is a δ-function at $\alpha = d$. For increasing disorder, the δ-function turns into a parabola, and the position of the maximum α_0 shifts to higher values $\alpha_0 > d$. The maximal value is $f(\alpha_0) = d$. So at least in the weak multifractality limit, there are always points $\mathbf{r}$ (lattice sites) where the intensity scales like

$$|\psi|^2 \sim L^{-\alpha_0} \quad , \tag{2.46}$$

and the fractal dimension at these points is $D_q = f(\alpha_0) = d$, like it is for a metal. $L^{-\alpha_0}$ is also called the *typical value* of the WFI, as it is the most probable one according to (2.45).

The ε-expansion has been used by Wegner to estimate the anomalous dimensions Δ_q in $d = 2 + \varepsilon$ dimensions [Weg87b]. The 4-loop results for the orthogonal and the unitary symmetry classes read [EM08]

$$\begin{aligned} \Delta_q^{\mathrm{O}} &= q(1-q)\varepsilon + \frac{\zeta(3)}{4} q(q-1)(q^2-q+1)\varepsilon^4 + \mathcal{O}\left(\varepsilon^5\right) \quad , \\ \Delta_q^{\mathrm{U}} &= q(1-q)\sqrt{\frac{\varepsilon}{2}} - \frac{3}{8} q^2(1-q)^2 \zeta(3)\varepsilon^2 + \mathcal{O}\left(\varepsilon^5\right) \quad , \end{aligned} \tag{2.47}$$

with $\zeta(3) \approx 1.202$ being Riemann's zeta function [BSMM00]. Keeping only the leading terms, the approximate parabolic form of Δ_q is retained, with $\gamma = \varepsilon$ for orthogonal symmetry and $\gamma = \sqrt{\frac{\varepsilon}{2}}$ for unitary symmetry.

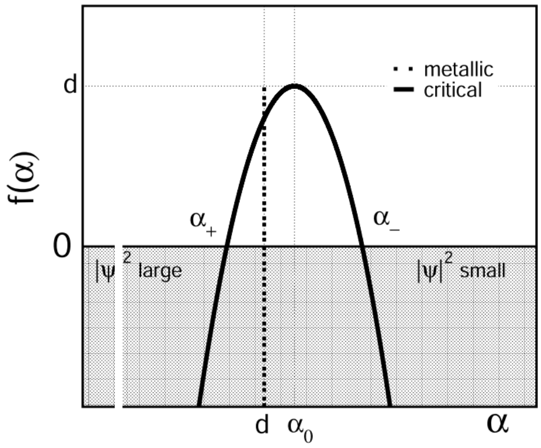

Figure 2.9.: Schematic plot of the singularity spectrum $f(\alpha)$ in the weak multifractality limit. From [EM08].

2.6. Metal-insulator transition in phosphorus-doped silicon

Various physical systems are known today to exhibit an AMIT, including even classical wave systems like light and microwaves in resonators [LvTW09]. Also localization of electronic wave functions in solids has been seen in a variety of materials. The standard example for a transition driven by the combined effects of disorder and interactions is *phosphorus-doped silicon* (Si:P) [SL97]. The transport properties near the transition in this doped semiconductor are additionally influenced by the existence of local magnetic moments. The MIT is expected at a certain critical dopant density n_c [BK94]. There is still no satisfying theory for such materials taking into account both disorder and interaction, further complicated by the existence of local magnetic moments. In the following, the physical situation in Si:P is illuminated, mostly in the picture offered by Löhneysen [vL00], and selected experimental results are reviewed.

2.6.1. Classification of metals and insulators

Relevant for the conduction properties of a solid is the energetic position of the chemical potential in relation to the electronic eigenstates (band structure) of the system. The highest completely occupied band is called the *valence band*, the uppernext band the *conduction band*. At zero temperature, the chemical potential is given by the *Fermi energy*[6] E_F. Up to E_F, all electronic states are occupied. If E_F lies within a bandgap, the material is an insulator at zero temperature (*band insulator*, see figure 2.10b), whereas if it lies inside a band, it can generally be regarded as a metal (see figure 2.10a).

There are other cases for which a material can become insulating: If the electron-electron interaction (Coulomb repulsion) is strong, electrons repell each other, and it is

---

[6] For non-zero temperatures, the chemical potential is usually referred to as the *Fermi level* in semiconductor physics.

unfavorable for them to occupy the same orbital (i.e., electrons with different spin). This effect gives rise to the *Mott-Hubbard transition* [Mot67, Mot68], which is a correlation-driven quantum phase transition. A simple method to describe the problem is given by the *Hubbard model* [Hub63],

$$\hat{H}_{\mathrm{H}} = t \sum_{\langle ij \rangle, \sigma} (c^{\dagger}_{i\sigma} c_{j\sigma} + c^{\dagger}_{j\sigma} c_{i\sigma}) + U \sum_{i} c^{\dagger}_{i\uparrow} c_{i\uparrow} c^{\dagger}_{i\downarrow} c_{i\downarrow} \quad , \tag{2.48}$$

where $\langle i, j \rangle$ captures all pairs of neighboring lattice sites between electrons may "hop" with a probability proportional to $|t|^2$, and $c_{i\sigma}$ denotes the annihilation operator of an electron with spin σ at site i. U defines the strength of the local (on-site) interaction. The effect of the strong local Coulomb repulsion on the band structure is illustrated in figure 2.10c: For sufficiently strong interaction parameter U, a bandgap is opening around the Fermi energy E_{F} (Hubbard splitting), causing the material to become a *Mott insulator*.

Yet another type of insulator is the *Anderson insulator*. For sufficiently strong disorder, there exist band regions which are populated by localized states. If the Fermi energy E_{F} happens to lie in one of those regions, the material is insulating (see figure 2.10d). Regions of localized and extended states are separated by mobility edges E_{M}. A simple model to describe the AMIT is given by the Anderson model (2.12) discussed above in section 2.2.

2.6.2. Conduction properties of semiconductors

A semiconductor is similar to a band insulator in the way that E_{F} lies in between the valence band and the conduction band, but is characterized by a rather small bandgap of typically a few eV (see figure 2.11a). For $T > 0\,\mathrm{K}$, thermally activated electrons are easily raised from the valence to the conduction band to allow for charge transport. However, at $T = 0\,\mathrm{K}$ a semiconductor is a perfect insulator.

By *doping* the semiconductor with atoms of another element, it is possible to tune its transport properties. Two kinds of dopings are distinguished:

n-doping A certain concentration x of the host atoms is replaced by atoms providing one or more excess electrons (donor atoms). This creates *donor levels* slightly below the conduction band, which are occupied by electrons at zero temperature (see figure 2.11b). At nonzero temperatures, these electrons are easily excited into the conduction band, contributing to the charge carrier density of the material.

p-doping A certain concentration x of the host atoms is replaced by atoms missing one or more electrons compared to the host atoms. This creates *acceptor levels* slightly above the valence band, which are unoccupied at zero temperature (see figure 2.11c). At nonzero temperatures, these levels are easily filled with valence band electrons, leaving behind *electron holes*, contributing to the charge carrier density of the material.

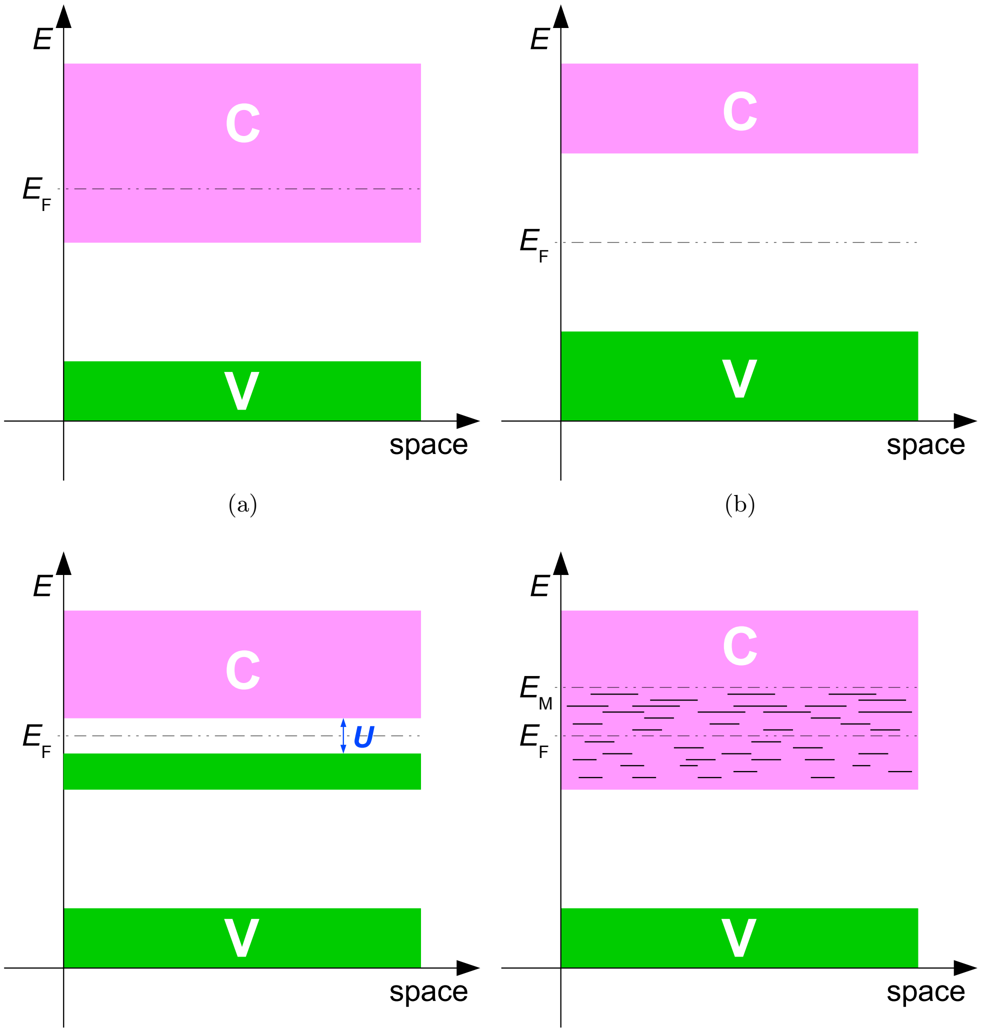

(a) (b) (c) (d)

Figure 2.10.: Schematical band diagrams for (a) a metal and different types of insulators: (b) Band insulator, (c) Mott insulator, (d) Anderson insulator.

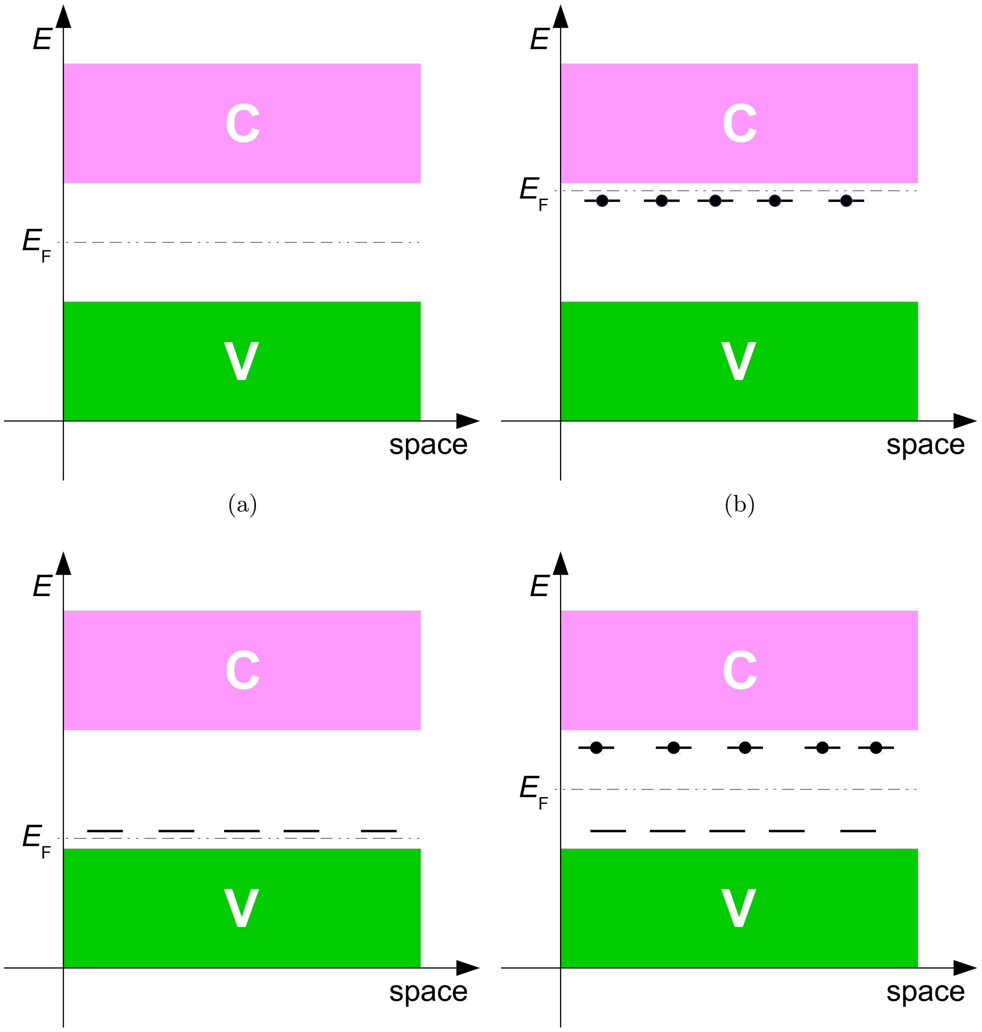

(a) (b) (c) (d)

Figure 2.11.: Schematical band diagrams for different types of semiconductors: (a) Undoped semiconductor, (b) n-doped semiconductor, (c) p-doped semiconductor, (d) compensated semiconductor.

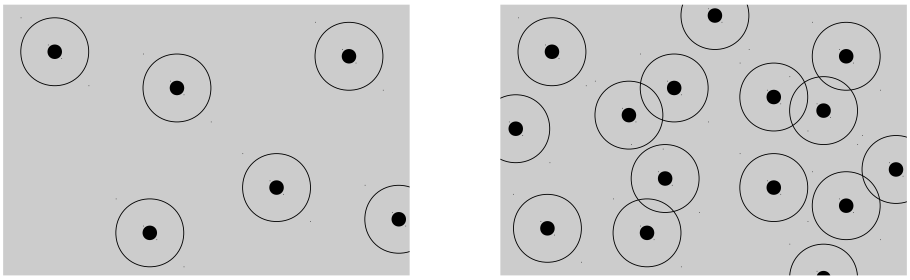

Figure 2.12.: Schematical plot of the hydrogen-like orbitals of phosphorus donors, for (a) low and (b) high dopant concentration, at random positions within the silicon bulk (gray).

If both types of dopants are present in a material, it can be *compensated* (see figure 2.11d). In a compensated semiconductor, the effects of donor and acceptor levels cancel each other, so that the Fermi energy stays in the middle of the bandgap, just as it is the case for undoped semiconductors.

2.6.3. Heavily doped semiconductors

In certain doped semiconductors, the additional electronic states introduced by the donor atoms (donor levels) are situated close to the conduction band. If the concentration of donors is low, the donor levels are strongly localized states, with similar energy but far apart in space (see figure 2.12a). The overlap between them is exponentially small [BK94]. In heavily doped semiconductors however, the distance between the donor states is small, and the states are overlapping (see figure 2.12b). The situation is illustrated in figure 2.12, where s-type (hydrogen-like) orbitals are assumed. This is a valid picture for phosphorus dopants inside a silicon host (Si:P), which form exactly one additional singly-occupied s-shell per dopant in the groundstate [BK94].

When the overlap between the hydrogenic donor states becomes intense, the *Pauli exclusion principle* causes the donor levels to hybridize, and a so called *impurity band* is forming (see figure 2.13b). This conforms to the common picture of band formation in solids [Czy08]. The Fermi energy E_F lies in the center of the impurity band, i.e. the impurity band is half filled. Similar to the band of the Anderson model (see figure 2.2), the impurity band may contain extended states in its center as well as localized states in its tails, separated by mobility edges E_M.

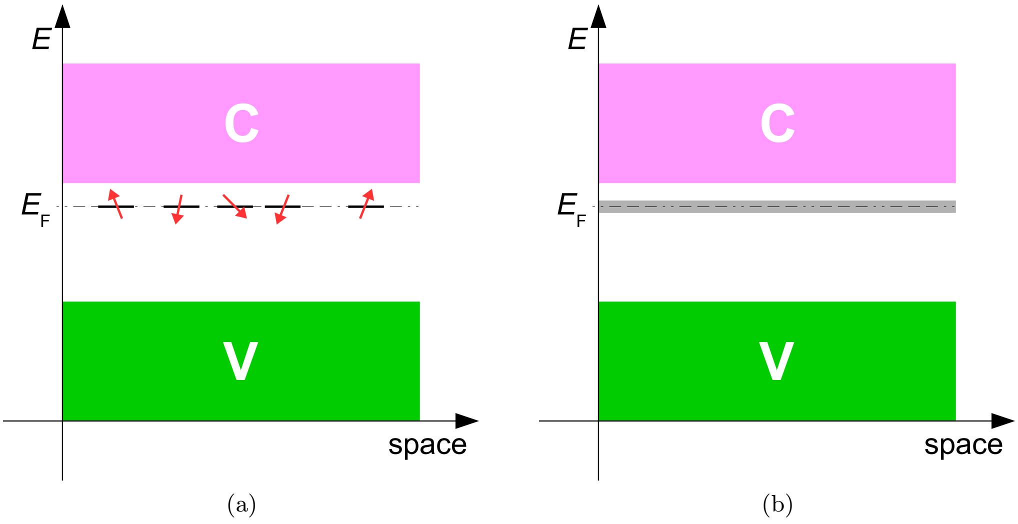

Figure 2.13.: Schematical band diagrams for phosphorus-doped silicon: (a) For low donor concentration, the singly-occupied donor states cause spin-1/2 moments (red arrows). (b) For high donor concentration, an impurity band is forming. Far enough on the metallic side of the transition, the moments have vanished.

2.6.4. Emergence of magnetic moments in phosphorus-doped silicon

Phosphorus possesses one more valence electron than silicon. So in phosphorus-doped silicon (Si:P), each P atom introduces one additional electron to the host material. The Coulomb repulsion is sufficiently strong to account for a Hubbard-like splitting of the energy levels, as it is known from the Hubbard model (2.48). This makes double occupancy of the donor levels energetically unfavorable, and explains why the donors are mostly occupied by a single electron in Si:P [BK94]. Thence, the localized singly-occupied donor levels give rise to local magnetic spin-1/2 moments. The existence of magnetic moments can be proven experimentally by observing the magnetic susceptibility $\chi(T)$ [SL97] (see figure 2.14).

The formation of a single magnetic moment can be studied in the *Anderson impurity model* [And61, Phi12]. It describes a single electronic band, which by itself contains the usual (extended) Bloch states $\psi_{\mathbf{k}\sigma}(\mathbf{r})$ (cf. section 2.1) with spin σ. Furthermore, a single impurity is considered, having a single impurity level d with energy ε_{d}. Hopping from and to the lattice sites surrounding the impurity site is allowed by a hopping matrix element $V_{\mathbf{k}\mathrm{d}}$. The impurity can either be singly or doubly occupied. The latter costs an extra energy U, exactly like in the Hubbard model (2.48). The Hamiltonian of the

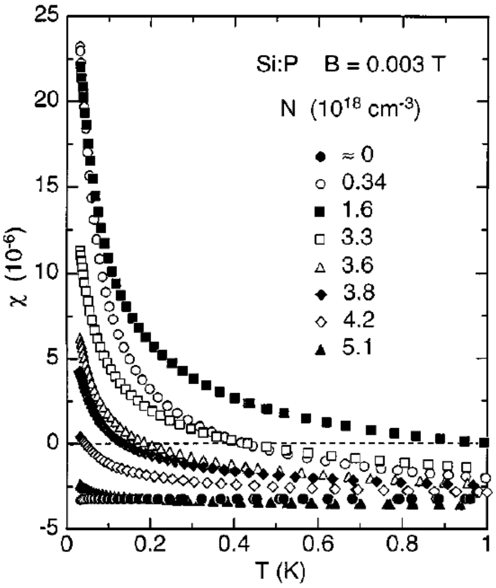

Figure 2.14.: Measurements of the temperature dependence of the magnetic susceptibility of phosphorus-doped silicon in a magnetic field of $B = 3\,\mathrm{mT}$, for different dopant concentrations N. From [SL97].

Anderson impurity model reads [Phi12]

$$\begin{aligned}\hat{H}_{\mathrm{AI}} &= \sum_{\mathbf{k}\sigma} \varepsilon_{\mathbf{k}} c^{\dagger}_{\mathbf{k}\sigma} c_{\mathbf{k}\sigma} + \sum_{\sigma} \varepsilon_{\mathrm{d}} c^{\dagger}_{\mathrm{d}\sigma} c_{\mathrm{d}\sigma} \\ &+ \sum_{\mathbf{k}\sigma} V_{\mathbf{k}\mathrm{d}} \left(c^{\dagger}_{\mathbf{k}\sigma} c_{\mathrm{d}\sigma} + c^{\dagger}_{\mathrm{d}\sigma} c_{\mathbf{k}\sigma} \right) + U c^{\dagger}_{\mathrm{d}\uparrow} c_{\mathrm{d}\uparrow} c^{\dagger}_{\mathrm{d}\downarrow} c_{\mathrm{d}\downarrow} \quad . \end{aligned} \tag{2.49}$$

$c_{\mathbf{k},\sigma}$ and $c_{\mathrm{d},\sigma}$ are annihilation operators for electrons with spin σ in the band and in the impurity level, respectively. Depending of the value of U in relation to the hopping matrix element $V_{\mathbf{k}\mathrm{d}}$ and the position of the impurity level ε_{d}, the system may favorize single occupancy and hence the formation of a local magnetic moment or not [Phi12].

Under heavy doping (high donor concentration), the donor states hybridize and form an impurity band. For strong Coulomb repulsion, the whole impurity band is splitted into two sub-bands (see figure 2.15), separated by a *soft Hubbard gap* [vL00]. The random positioning of the dopant atoms increases the disorder. Both, the occupied sub-band below the Fermi energy and the unoccupied sub-band above it, contain localized as well as extended states, separated through mobility edges. This explains why the number of magnetic moments observed in Si:P is usually smaller than the number of donor levels [vL00] and depends on the dopant density n.

For experiments, the random distribution of dopants is essential. Clustering or short-range ordering would affect the MIT. The statistical distribution of donor atoms in Si:P can be checked by scanning tunneling microscopy (STM) [vL00]. To prove the existence

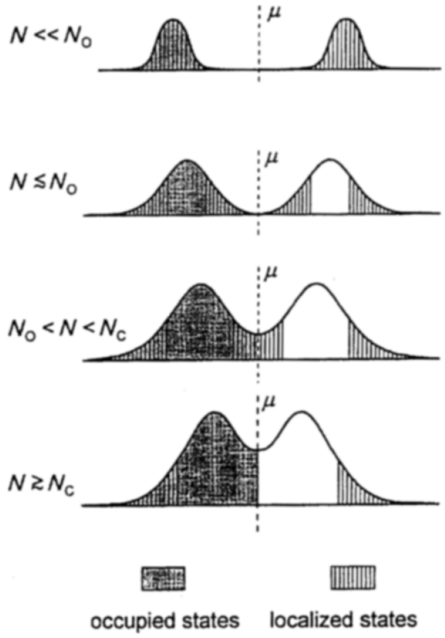

Figure 2.15.: Evolution of the impurity band density of states when crossing the metal-insulator transition in phosphorus-doped silicon. From [vL00].

local magnetic moments, different quantities like the magnetization, magnetic resonance or the specific heat are experimentally accessible [PSBR86, vL00].

2.6.5. MIT in phosphorus-doped silicon

Figure 2.15 sketches the process that leads to the MIT in Si:P as envisioned by Löhneysen [vL00]. This situation does not occur in compensated semiconductors like Si:(P,B) (additional boron-doping), as there the Fermi energy does not lie within one of the impurity bands. For low dopant density n, the two Hubbard sub-bands are well separated. The Fermi energy lies in the gap between the sub-bands, hence the material is insulating at $T = 0\,\mathrm{K}$ like in a band insulator. As n is increased, the sub-bands have to accomodate a rising number of impurity states, thus they broaden.

At a certain dopant density $n_0 \approx 2.7 \cdot 10^{18}\,\mathrm{cm}^{-3}$ [vL00], the broadening sub-bands start to overlap. At this point, the Fermi energy no longer lies in the bandgap, but nevertheless the material is still insulating, as in the shallow band tails, only localized states exist (Anderson insulator). The gap is a soft Coulomb gap, with a DOS behaving like $\rho(E) \sim |E - E_\mathrm{F}|^2$ [vL00]. At n_0, the density of magnetic moments is highest.

Reaching the critical dopant density $n_\mathrm{c} \approx 3.52 \cdot 10^{18}\,\mathrm{cm}^{-3}$ [vL00], the overlap between the two sub-bands has reached an extent for which the region of localized states around the Fermi energy has disappeared, as the value of the DOS at the Fermi energy has increased, and the mobility edges surrounding the Fermi energy have converged on its position. The Fermi energy now resides within a region of conducting impurity states, and thus the MIT has been crossed. However, there still exist localized impurity states in the outer tails of the impurity band, which still carry magnetic moments. This explains why magnetic moments have been found experimentally even on the metallic side of the MIT in Si:P, up to dopant densities of $n \approx 2n_\mathrm{c}$ [MSB89, SL97] (cf. figure 2.14).

Silicon solidifies in the diamond structure, with a lattice spacing of $a = 0.543\,\mathrm{nm}$. There are eight lattice sites in the conventional unitcell of the diamond structure. The particle density of silicon is therefore $n_\mathrm{Si} = 5.000 \cdot 10^{22}\,\mathrm{cm}^{-3}$. The critical dopant density has been experimentally determined to $n_\mathrm{c} \approx 3.52 \cdot 10^{18}\,\mathrm{cm}^{-3}$ [SL97]. This corresponds to a fraction of 0.007 at% of the silicon atoms being replaced by phosphorous atoms. For comparison, the solubility limit of phosphorus in silicon is 2.4 at% [vL00] (at standard pressure).

The density of dopants carrying a localized moment lies in the range $10^{17}..10^{18}\,\mathrm{cm}^{-3}$ in the insulating regime ($n < n_\mathrm{c}$), and can drop down to about $10^{16}\,\mathrm{cm}^{-3}$ in the metallic regime ($n > n_\mathrm{c}$) [vL00]. So, realistic values for the fraction n_M of dopants carrying a local moment range from a few percent on the metallic side to several tens of percent on the insulating side of the transition. In our calculations (see chapter 5), we assume a fixed fraction of $n_\mathrm{M} = 5\,\%$.

Experimentally, it can be difficult to vary the dopant concentration n homogeneously across the critical disorder strength, for it requires the synthesis of different samples. An alternative approach is given by the application of *uniaxial stress* to a specimen that is slightly on the insulating side of the critical donor density n_c [vL00]. The MIT can then be obtained by considering various experimentally accessible quantities. Figure 2.16 shows the result of measurements of the temperature-dependence of the conductivity for very small temperatures [RMP+83] and different dopant densities n. Here, a critical dopant density of $n_\mathrm{c} \approx 3.74 \cdot 10^{18}\,\mathrm{cm}^{-3}$ was found. The positive slope of the curve for $n = 7.0 \cdot 10^{18}\,\mathrm{cm}^{-3}$ in the double-log plot clearly indicates metallic behavior. The curves for $n = 3.84 \cdot 10^{18}\,\mathrm{cm}^{-3}$ and $n = 3.75 \cdot 10^{18}\,\mathrm{cm}^{-3}$ feature a negative slope, but still converge to a finite value for $T \to 0$, and are therefore still identifyable as metallic, with the latter being very close to the MIT. For $n = 3.70 \cdot 10^{18}\,\mathrm{cm}^{-3}$, the behavior has changed drastically, showing a diverging curve as $T \to 0$, which is attributed to an insulator.

Experimentally, the localization length exponent ν on the insulating side and the conductivity exponent s on the metallic side of the transition (2.27) have both been determined to values close to 1 [LvTW09]. In the past, the exponents for uncompensated doped semiconductors have first been found to be rather 0.5 (the "exponent puzzle") [KM93], but these results were later be clarified to lead to an exponent of 1 as well [LvTW09].

The MIT in Si:P has still not been fully understood on theoretical grounds. The most promising approach consists in the *Anderson-Hubbard model* [vL00], which features the essential elements of both disorder and on-site Coulomb interaction:

$$\hat{H}_\mathrm{AH} = \sum_{i\sigma} (\varepsilon_i - \mu)\, c^\dagger_{i\sigma} c_{i\sigma} + \sum_{ij\sigma} t_{ij}\, c^\dagger_{i\sigma} c_{j\sigma} + U \sum_i c^\dagger_{i\uparrow} c_{i\uparrow} c^\dagger_{i\downarrow} c_{i\downarrow} \quad . \tag{2.50}$$

$c_{i\sigma}$ is the annihilation operator for an electron with spin σ in the groundstate of the

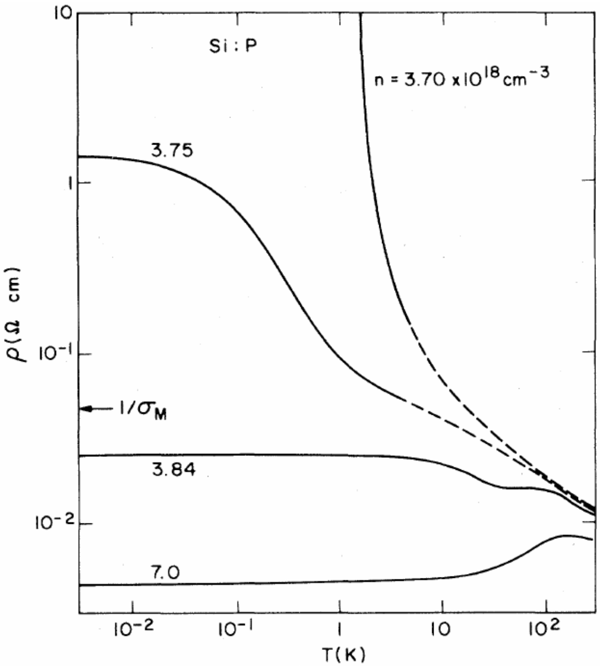

Figure 2.16.: Experimental results for the temperature-dependent resistivity ρ in phosphorous-doped silicon, for different donor densities n. From [RMP+83].

dopant atom at site i. As before, ε_i is a random site potential, and t_{ij} is a hopping amplitude. μ is the chemical potential here, and U is the energy that has to be paid for double occupancy of a site, just as in the Hubbard model (2.48).

In order to simplify the description, we consider a variant of the Anderson-Hubbard model (see chapter 5), replacing the Hubbard term by one describing an exchange coupling to classical magnetic spin-1/2 impurities. We have thus chosen to separate the dynamics of the itinerant impurity band electrons from the local moments (*two-fluid model*) [MSB89, Sac89], while in real Si:P, the local moments are caused by the itinerant electron spins themselves [PGBS88].

3. Numerical methods

Studies of the problem of localization and metal-insulator transitions have to rely largely on numerical simulations, as adequate analytical techniques are still rare in this field of research [Nob77]. In this chapter, the numerical methods used in this thesis to study the effective model for the impurity band electrons in Si:P are described (see chapter 5).

In section 3.1, a data structure for defining effective tight binding supercells is introduced, including an explanation of the algorithm to obtain the tight binding matrix. Such a matrix can then be used within the kernel polynomial method (KPM) [WWAF06] to calculate the local density of states (LDOS) and the average density of states (ADOS). The KPM algorithms used in this work are explained in section 3.2.

The LDOS is used to obtain two ensemble averages: The geometric average (GLDOS) and the arithmetic average (ALDOS) of the LDOS. The algorithms used to obtain these ensemble averages are illustrated in section 3.3, including the method used to account for the statistical error. The chapter concludes with some test calculations and performance checks in section 3.4, where we compare our results with those by others who have also used the KPM to calculate the GLDOS and the ADOS [SF09].

In appendix B, a few additional remarks regarding the numerical methods and further implementation details are given.

3.1. Hierarchical data structure for effective tight binding supercells

Effective tight binding models (ETBM), written in site-diagonal basis, have the potential to describe any microscopic structure (nanostructure) that consists of single “atomic” sites (not necessarily the sites of a lattice). At every site, one or more states can be defined, each characterized by a certain potential energy. Hopping transport is allowed by defining hopping matrix elements between the states.

In general, it is sufficient to be able to place sites at specific coordinates somewhere within the supercell, and to define hoppings between them. However, both organization and performance are greatly improved if some or all of the sites are arranged on a periodic grid. By placing as many sites as possible on a lattice, which is defined by repeating a small unitcell a specific number of times in each spatial dimension, not only memory usage is minimized, but also computational effort to retrieve the tight binding matrix.

This is why we decided to include the concept of finite lattices into the object-oriented framework used to define tight binding supercells, which is implemented by the classes `Lattice` and `SparseLattice` as described below. The usage of unitcells that are repeated periodically in space does however not exclude the ability to define random potentials

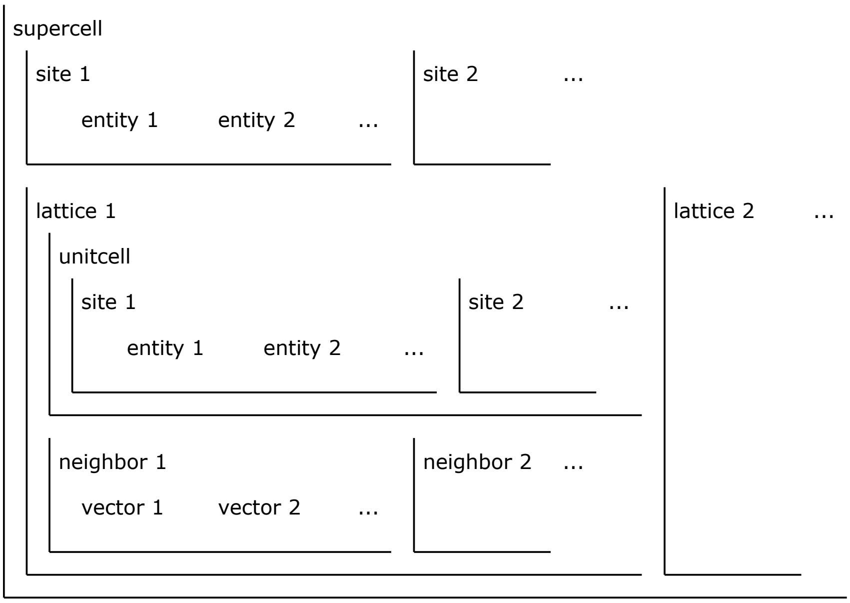

Figure 3.1.: Illustration of the hierarchical data structure for defining effective tight binding nanostructures.

and hopping parameters. These can still be defined by defining rules for the generation of random numbers from a probability distribution instead of setting the matrix elements with constant values. For the most part, the performance gain by considering sites sitting on a lattice can be preserved even in the presence of disorder.

3.1.1. General data layout

Any nanostructure on the atomic level can naturally be described by a hierarchical data structure. The root element of this structure is the `SuperCell` object, which holds all information about the system. The `SuperCell` object can hold any number of single `Site` objects, which can be placed anywhere inside the d-dimensional supercell, and any number of `Lattice` or `SparseLattice` objects. In the supercell object, also the number of spatial dimensions d is specified, as well as the kind of boundary conditions that should be applied to each of the dimensions (static, periodic, or antiperiodic boundary conditions). Figure 3.1 illustrates the hierarchical layout of the data structure.

In most solid state problems, a periodic lattice is considered. The lattice objects ease the description of the system considerably. On most occasions (like in our work), there is no need to define anything but a single `Lattice` object within the `SuperCell` object. However, defining multiple `Lattice` objects could have its applications when ETBM for solid state nanostructures are investigated, e.g. *quantum wells*, *quantum dots* [Mou07], *nanorods*, or when interfaces between different kinds of lattice structures are of interest.

Adding single `Site` objects to the supercell could be practical if one is interested in surface effects including *adatoms*, or in interstitial impurities.

`Lattice` and `SparseLattice` objects are defined by a unique `UnitCell` object, which defines a *convential unitcell* (in general of rhomboidal shape) within the d-dimensional supercell. Furthermore, the lattice object has to contain the information about how often the unitcell is repeated in space in each of the spatial dimensions. The unitcell can hold any number of `Site` objects. As usual, the position of the sites is defined here in relative terms to the shape of the unitcell (the basis vectors spanning the lattice). Each `Site` object can hold any number of `Entity` objects, which stand for the states located at that site (i.e., orbitals), as it is usual for an ETBM written in site-diagonal basis.

The so defined data structure is still missing information about the existing hopping matrix elements. To allow for hopping transport between the orbitals (to be more specific, between any pair of `Entity` objects), different facilities exist to store that kind of information on various levels within the hierarchical data structure. First, the `SuperCell` object allows for the definition of hoppings between the states at different single sites that are defined directly within it. Far more important for most applications is a special facility of the `Lattice` object, which is the so called `Neighbor` object. It defines a whole class of interactions between certain copies of the unitcell within a lattice. Each `Neighbor` object is characterized by some integer vectors specifying the direction of hopping, i.e. to which neighboring unitcells the hopping shall occur (nearest neighbors, next-nearest neighbors etc.). To be complete, also hoppings within `UnitCell` and `Site` objects can be defined, the latter to allow for a local (on-site) interaction.

As mentioned earlier, each site potential and each hopping can be set with either a constant value, or with a rule specifying how random values should be drawn from a probability distribution. Each time the tight binding matrix is requested from the `SuperCell` object, a set of random values is generated, which are placed on the corresponding matrix elements accordingly. In this way, a separation is achieved between the abstract definition of the ETBM and the generation of disorder configurations in form of corresponding tight binding matrices. The `SuperCell` object can be stored (e.g. in a file) and is an abstract description of a tight binding system in the sense that an arbitrary number of disorder realizations can be drawn from it at any time.

To complete the description, the difference between `Lattice` and `SparseLattice` objects has to be mentioned. While the `Lattice` objects assumes that the unitcell is repeated uniformly in space, i.e. placed at every position where a lattice vector is pointing, in a sparse lattice, the unitcell is only placed on a certain subset of these positions. Example applications are percolation problems [SF09], or the effective dilute Heisenberg model [CB10, CBB11, CBKB12], or in general all problems where only a certain fraction of lattice sites is occupied by a state.

3.1.2. Constructing the tight binding matrix

In most numerical applications, the goal of the definition of a tight binding supercell is the generation of the corresponding tight binding matrix, which is the matrix representation of the underlying Hamiltonian. Usually many quantities of interest can be deduced from the matrix, using various approximative numerical methods. One example is the KPM, which we use to calculate the DOS and the LDOS (see section 3.2). Using the hierarchical data structure described above, the construction of the matrix follows a clear scheme, which is illustrated in figure 3.2.

The matrix is constructed using a top-to-bottom approach. When the tight binding matrix is requested from the `SuperCell` object, it cycles all its site and lattice definitions and requests their corresponding submatrices. Each `Lattice` object requests the submatrix of its unitcell, and then stacks them on the main diagonal, corresponding to the specified number of times the unitcell is repeated in space. Certain off-diagonal blocks are filled with hopping matrices originating from the `Neighbor` objects, which naturally share its size and structure with those of the unitcell matrices. The `SuperCell` object then again stacks all submatrices from the lattices and single sites on the main diagonal, and again fills off-diagonal blocks with possibly defined hoppings between different objects in the supercell.

The mapping of the matrix indices to the corresponding states is fixed by the order in which the sites and lattices are defined in the `SuperCell` object, as well as by the order of the dimensions used in the `Lattice` object. It is important to know the precise mapping in systems which are not completely homogeneous to ensure the identification of important microscopic features (nanostructures etc.). The recommended output format of the matrix is one of the available sparse-matrix formats, as tight binding matrices are usually sparsely occupied. The most convenient format for methods including a matrix-vector multiplication (as it is the case for the KPM) is the compressed-sparse row (CSR) format.

Using only `Lattice` objects, the performance generating the matrix scales linearly with the system size N (number of unitcells), even when random potentials are included (see figure 3.3). Deviations are only seen for very small system sizes, as every computer algorithm possesses a certain overhead which does not depend on the system size. In figure 3.3, OPT stands for an optimized algorithm which is specialized on one-band tight binding models on a d-dimensional hypercubic lattice with the restriction to nearest neighbor hoppings[1]. STD is the standard algorithm that can handle any kind of ETBM, including long-range hoppings etc.

3.2. The kernel polynomial method

The kernel polynomial method (KPM) is a polynomial expansion technique based on *Chebychev polynomials* [WWAF06]. The latter come in two flavors, first kind and second kind. For the calculation of the local density of states (LDOS) and the density of states (DOS), only the first kind is of interest. On a lattice with lattice sites i, the LDOS reads

$$\rho_i(E) = \sum_{k=1}^{N_\mathrm{k}} \left|\langle k|i\rangle\right|^2 \delta(E - E_k) \quad , \tag{3.1}$$

---

[1] The matrix elements can nevertheless be set with random numbers.

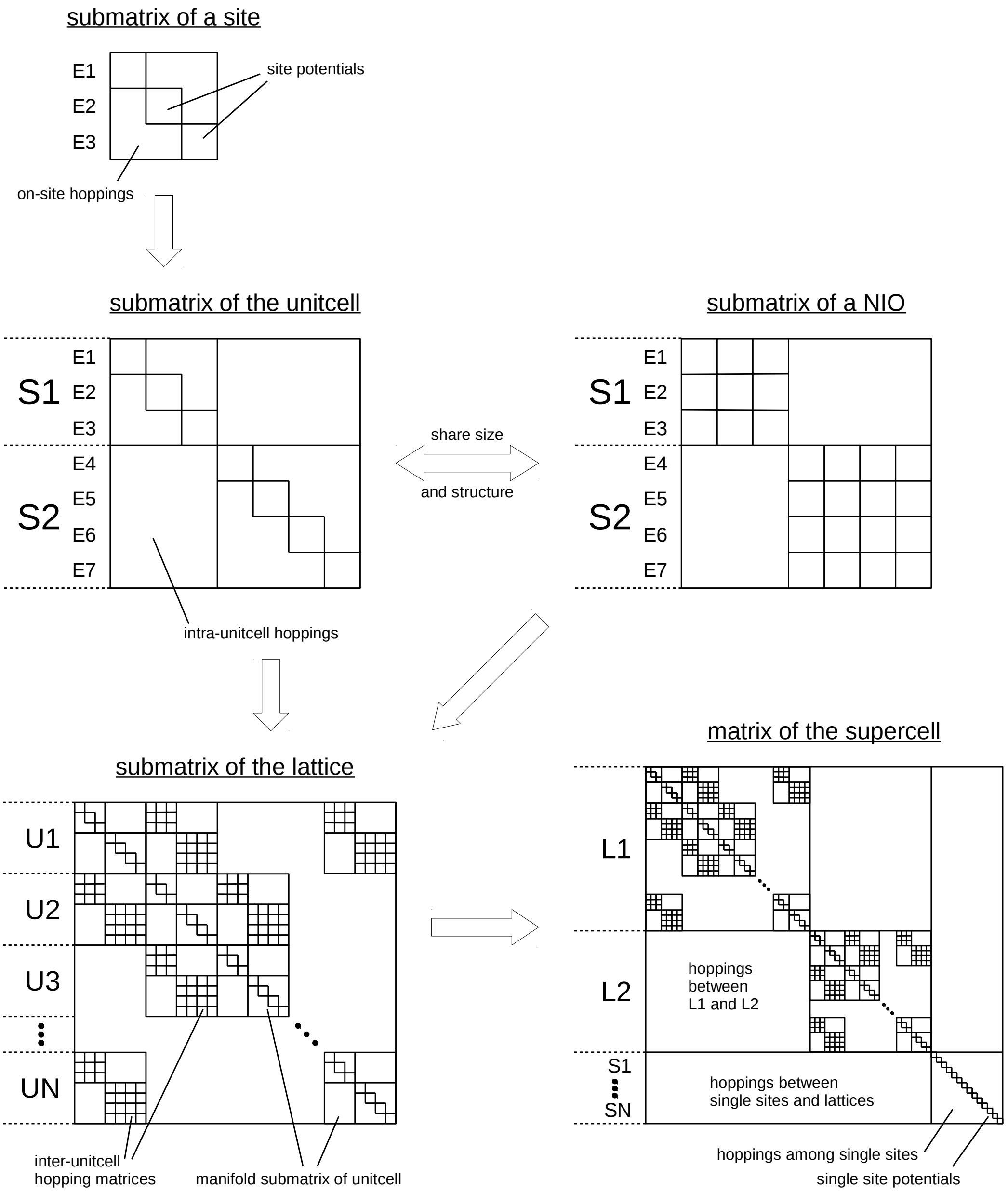

Figure 3.2.: Scheme illustrating the generation of the tight binding matrix from the hierarchical data structure.

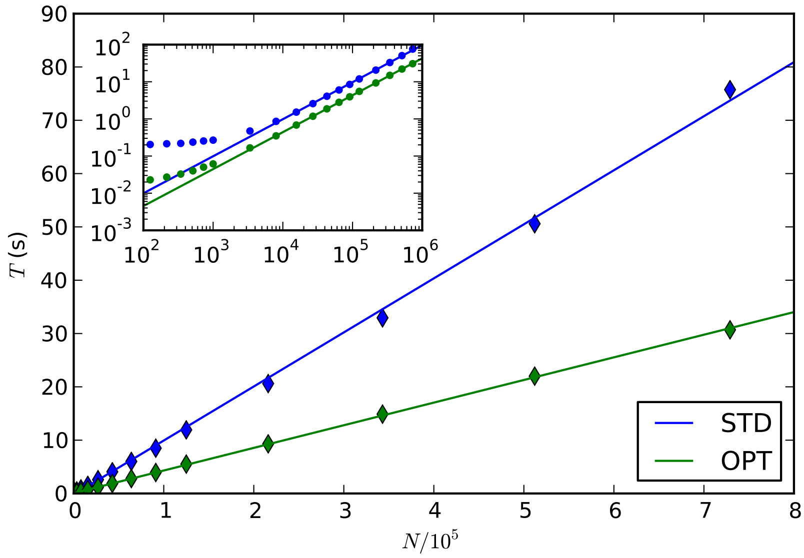

Figure 3.3.: Performance check of the algorithm for constructing the tight binding matrix, using either the standard algorithm (STD) or the optimized algorithm (OPT). The inset is showing a double-logarithmic plot of the same data.

where N_k is the number of eigenstates. Note that in a one-band tight binding model without spin, $N_\mathrm{k} = N$, where N is the number of lattice sites. The Chebychev polynomials $T_m(x)$ of first kind are defined as [WWAF06]

$$T_m(x) = \cos(m \arccos x) \quad . \tag{3.2}$$

They are defined on the interval $[-1, 1]$ only. Using the expansion

$$f(x) = \frac{1}{\pi\sqrt{1-x^2}} \left(\mu_0 + 2 \sum_{m=1}^{M} \mu_m \, T_m(x) \right) \quad , \tag{3.3}$$

the function $f(x)$ can be approximated to arbitrary order, by taking into account a finite number M of coefficients μ_m (the *truncation limit*). The expansion (3.3) approaches the exact result for $M \to \infty$, but often, a reasonable result is already obtained for $M \approx 100..1000$, depending on the problem.

The coefficients μ_m of the expansion (*Chebychev moments*) depend on the *target function* $f(x)$, i.e. the spectral quantity to approximate, which in our case is either the LDOS or the DOS, as detailed in section 3.2.4. The moments are defined as [WWAF06]

$$\mu_m = \int\limits_{-1}^{1} \tilde{f}(\tilde{x}) \, T_m(\tilde{x}) \, \mathrm{d}\tilde{x} \quad , \tag{3.4}$$

where $\tilde{f}(\tilde{x})$ is the rescaled version of the spectral quantity $f(x)$ so that its spectrum fits into the interval $\tilde{x} \in [-1, 1]$.

The KPM scheme – and with it the algorithm – can be devided into several consecutive steps:

1. Rescale the matrix H so that its spectrum fits into the interval $[-1, 1]$.
2. Choose a suitable start vector.
3. Iterative calculation of the Chebychev moments (up to the truncation limit M).
4. Kernel damping.
5. Reconstruction of the target function.
6. Inversly rescale the target function.

The steps are explained in more detail in the following sections.

3.2.1. General code layout

Below is an example of what an actual implementation of a KPM algorithm could look like. Like all code examples showed in this thesis, it resembles “almost” working Python code [Oli07] that originates from our actual implementation[2], but has been stripped from anything that is not totally necessary for understanding the algorithm itself (issues like datatype conversion, error handling, documentation, parallelization directives etc.).

```
def ldos(mat, state, limit, enum, erange):
    rank = mat.shape[0]
    rmat, rparams = rescale(mat, erange)
    renerg = get_energ(enum, rparams)
    start = svect(rank, state)
    moments = mom(rmat, start, limit)
    moments = kernel(moments)
    dens = rcstr(moments, enum)
    energ = inverse_rescale(renerg, rparams)
    return energ, dens
```

The first step is to rescale the Hamiltonian matrix `mat` according to the given energy range `erange` so that the original spectrum fits into the interval $[-1, 1]$. `rparams` contains the two parameters a and b that define the rescaling (see section 3.2.2 for details). Knowing these parameters, also the rescaled energy values `renerg` can be created, which also depend on the required number of energy intervals `enum`.

The next step is to choose the start vector. `rank` defines its length, and `state` selects one of the eigenstates of the Hamiltonian, i.e. the lattice site for which the LDOS is to be calculated.

---

[2] The full source code can be found at `http://github.com/proggy/kpm/`.

The most time consuming part is usually the calculation of the Chebychev moments `moments`. The algorithm does not only depend on the rescaled matrix `rmat` and the start vector `start`, but also on the chosen truncation limit `limit`. As soon as the list of moments has been obtained, the Jackson kernel can be applied. Now the LDOS `dens` is reconstructed using the standard reconstruction formula (3.3) (we do not use the fast-Fourier transform (FFT) for optimization) and the energy values `energ` are scaled back to the original spectrum of the matrix using the rescaling parameters `rparams`.

3.2.2. Rescaling the matrix

The Chebychev polynomials (3.2) are defined only on the interval $[-1, 1]$. To be able to approximate a function using the Chebychev expansion (3.3), it must be made sure that the argument does not exceed this interval. In case of the spectral quantities of a matrix (or operator) H, this means that its spectrum must be rescaled to fit into the interval $[-1, 1]$. This may be done by a simple linear transformation [WWAF06],

$$\tilde{H} = \frac{H - Ib}{a} \quad , \tag{3.5}$$

$$\tilde{E} = \frac{E - b}{a} \quad , \tag{3.6}$$

$$\tag{3.7}$$

where I is the identity matrix. Given a certain spectral range $[E_{\text{min}}, E_{\text{max}}]$, the *rescaling factors* a and b can be obtained using [WWAF06]

$$a = \frac{E_{\text{max}} - E_{\text{min}}}{2 - \epsilon} \quad , \tag{3.8}$$

$$b = \frac{E_{\text{max}} + E_{\text{min}}}{2} \quad . \tag{3.9}$$

$$\tag{3.10}$$

Note that a and b may have to possess the dimension of energy to make $\tilde{E}$ a dimensionless quantity, i.e. we may measure it in terms of the constant hopping parameter t.

Since the spectrum is generally unknown, one can either make an “educated guess”, or use existing methods to determine the extremal eigenvalues of a matrix, for example the *Lanczos method* [Lan51]. To be entirely sure that the (numerically estimated) spectrum will not exceed the interval $[-1, 1]$, a small value ϵ can be introduced that should be adjusted to the smallest representable floating point value of the computer system, or to the accuracy of the estimated spectral range. Alternatively, an overestimation of the spectral range is usually a good idea, also to avoid unwanted effects by the spectral dependence of the resolution (see section 3.2.7). In our calculations, we choose $a = 24t$ and $b = 0$ for all our calculations. This also assures that the densities of all systems possess the same energy discretization, which simplifies the subsequent data analysis.

3.2.3. The start vector

This step is especially simple in the case of the KPM algorithm for the LDOS, applied to the case of a simple tight binding system (2.1). As such a tight binding Hamiltonian is usually written in terms of a basis with states each located at one of the lattice sites, the start vector just has to be a vector containing only one nonzero element at the index i of the respective lattice site (which is equal to one due to normalization). So the start vector is of the form

$$\phi_0 = (0, 0, \dots, 1, \dots) \quad . \tag{3.11}$$

Considering a model with spin, the index needs to include both site and spin index, i.e. $\phi_0 \equiv |i\sigma\rangle$. The index mapping must be unambiguous, but the general form of the start vector remains the same.

For the calculation of the DOS, a random state is chosen, which is explained below (section 3.2.4).

3.2.4. Calculation of Chebychev moments

The recursive algorithm to calculate the Chebychev moments is the central part of every KPM algorithm. At least for Chebychev expansions in one variable, and for typical matrix sizes and truncation limits, it is also the numerically most expensive calculation step.

It can be shown (see appendix A.1) that the recursive relations

$$\begin{aligned} &T_0(x) = 1 \quad , \quad \mathrm{T_1(x) = x} \quad , \\ &T_{m+1}(x) = 2x\, T_m(x) - T_{m-1}(x) \quad , \end{aligned} \tag{3.12}$$

hold for the Chebychev polynomials of first kind (3.2) [WWAF06]. So the state

$$|\phi_m\rangle = T_m(\tilde{H})\, |\phi_0\rangle \tag{3.13}$$

can be obtained iteratively using

$$|\phi_1\rangle = \tilde{H}\, |\phi_0\rangle \quad , \quad |\phi_{\mathrm{m+1}}\rangle = 2\tilde{\mathrm{H}}\, |\phi_{\mathrm{m}}\rangle - |\phi_{\mathrm{m-1}}\rangle \quad , \tag{3.14}$$

up to the desired truncation limit M [WWAF06].

For moments of the form of an expectation value of Chebychev polynomials in $\tilde{H}$, like it is the case for the LDOS (3.20) or the DOS (3.25), a more efficient variant of the recursive relations (3.14) exists [WWAF06],

$$\begin{aligned} \mu_0 &= \langle\phi_0|\phi_0\rangle \quad , \\ \mu_1 &= \langle\phi_1|\phi_0\rangle \quad , \\ \mu_{2m} &= 2\,\langle\phi_m|\phi_m\rangle - \mu_0 \quad , \\ \mu_{2m+1} &= 2\,\langle\phi_{m+1}|\phi_m\rangle - \mu_1 \quad , \end{aligned} \tag{3.15}$$

which yields two moments per loop. So a factor of two is gained in terms of efficiency. Here is a pseudo-code example to evaluate (3.15):

```
mu[0] = dot(phi0, phi0)  # dot product
phi1 = matvec(mat, phi0)  # matrix-vector multiplication
mu[1] = dot(phi1, phi0)
for m in range(1, limit/2):  # assume an even truncation limit
    phi2 = matvec(mat, phi1) - phi0[k]
    mu[m*2] = 2 * phi1[k] * phi1[k] - mu[0]
    mu[m*2+1] = 2 * phi2[k] * phi1[k] - mu[1]
    temp = phi0; phi0 = phi1; phi1 = phi2; phi2 = temp  # swap pointers
```

This again is just a brief example for the general form of the algorithm to compute the Chebychev moments, which leaves out many possible improvements in terms of efficiency which may be applied to the code. Most of all, an actual implementation should store the matrix in compressed sparse-row (CSR) format for the matrix-vector multiplication to be most efficient.

From the above code example it becomes apparent that using an iterative algorithm based on the recursive relations (3.15), the memory usage can be kept to a minimum. Only three state vectors `phi0`, `phi1` and `phi2` of length N (the rank of the matrix) have to be stored, plus the list of moments `mu` with length M and the matrix `mat`. If the tight binding matrix `mat` or the start vector `phi0` contain complex elements, also the vectors `phi0`, `phi1` and `phi2` have to be able to hold complex numbers, which roughly doubles the memory demands.

Chebychev moments for the LDOS

The Chebychev moments for the rescaled LDOS $\tilde{\rho}_i(\tilde{E})$ (normalized with respect to the rescaled spectrum $\tilde{E}$) at lattice site i read [WWAF06]

$$\mu_m^{(i)} = \int_{-1}^{1} \tilde{\rho}_i(\tilde{E})\, T_m(\tilde{E})\, \mathrm{d}\tilde{E} \tag{3.16}$$

$$= \frac{1}{N} \sum_{k=0}^{N-1} \left|\langle i|k\rangle\right|^2 \int_{-1}^{1} T_m(\tilde{E})\, \delta(\tilde{E} - \tilde{E}_k)\, \mathrm{d}\tilde{E} \tag{3.17}$$

$$= \frac{1}{N} \sum_{k=0}^{N-1} \left|\langle i|k\rangle\right|^2 T_m(\tilde{E}_k) \tag{3.18}$$

$$= \frac{1}{N} \sum_{k,k'=0}^{N-1} \langle i|k\rangle \, \langle k|T_m(\tilde{H})|k'\rangle \, \langle k'|i\rangle \tag{3.19}$$

$$= \frac{1}{N} \langle i|T_m(\tilde{H})|i\rangle \quad , \tag{3.20}$$

where the system size N is identical to the rank of the rescaled tight binding matrix $\tilde{H}$ and the number of its eigenvalues $\tilde{E}_k$. So the KPM algorithm for moments of the form of simple expectation values (3.15) can be used to calculate the Chebychev moments for the LDOS. Note that for a non-disordered system, the LDOS at any site i is identical to the DOS, so in that case, the calculation of the DOS breaks down to the calculation of a single LDOS at an arbitrary lattice site.

Chebychev moments for the DOS

The Chebychev moments for the rescaled DOS $\tilde{\rho}(\tilde{E})$ (normalized with respect to the rescaled spectrum $\tilde{E}$) read [WWAF06]

$$\begin{aligned}
\mu_m &= \int_{-1}^{1} \tilde{\rho}(\tilde{E})\, T_m(\tilde{E})\, \mathrm{d}\tilde{E} && (3.21)\\
&= \frac{1}{N} \sum_{k=0}^{N-1} \int_{-1}^{1} T_m(\tilde{E})\, \delta(\tilde{E} - \tilde{E}_k)\, \mathrm{d}\tilde{E} && (3.22)\\
&= \frac{1}{N} \sum_{k=0}^{N-1} T_m(\tilde{E}_k) && (3.23)\\
&= \frac{1}{N} \sum_{k=0}^{N-1} \langle k | T_m(\tilde{H}) | k \rangle && (3.24)\\
&= \frac{1}{N} \mathrm{Tr}\, T_m(\tilde{H}) \quad , && (3.25)
\end{aligned}$$

so it comes down to the calculation of a trace of expectation values, over all eigenstates $|k\rangle$ of the system, i.e. over the whole Hilbert space. To avoid this, it is advantageous to use an approximation to evaluate the trace, by averaging the moments over a small number $R \ll N$ of random states $|r\rangle$ (*stochastic evaluation of the trace*) [WWAF06],

$$\mu_m \approx \frac{1}{NR} \sum_{r=0}^{R-1} \langle r | T_m(\tilde{H}) | r \rangle \quad , \tag{3.26}$$

where for the random states $|r\rangle$, *random-phase vectors* of the form

$$|r\rangle = \sum_{i=0}^{N-1} \xi_{ri}\, |i\rangle \quad , \quad \xi_{\mathrm{ri}} = \mathrm{e}^{\mathrm{i}\phi} \quad , \quad \phi \in [0, 2\pi] \tag{3.27}$$

are an excellent choice [WWAF06]. The number of random vectors R can often be kept to a small fixed number, while the additional ensemble averaging which is needed anyway for disordered systems can then be carried out to arbitrary accuracy. For the efficient calculation of the expectation values, again the recursive relations (3.15) can be used, using a random vector (3.27) as start vector. Note that to calculate the average density of states (ADOS) of a disordered system, an ensemble averaging (arithmetic mean) over densities of different disorder configurations has still to be added.

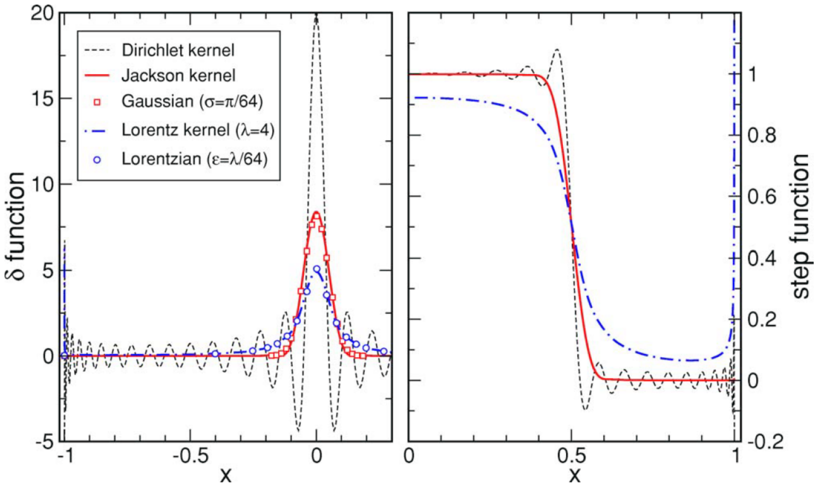

Figure 3.4.: Damping effect of different kernels on spectra containing δ-functions (left) or step functions (right). The truncation limit is $M = 64$. With kind permission by the authors [WWAF06].

3.2.5. Kernel damping

If the Chebychev moments calculated above were used directly to reconstruct the target function, the result would still suffer from oscillations near sharp features (discontinuities or singularities), so called *Gibbs oscillations* [WWAF06]. To get rid of these oscillations, it is possible to apply a *kernel* to the Chebychev expansion in order to smoothen the target function. Formally, this concept corresponds to a convolution of the target function $f(x)$ with a kernel [WWAF06]. For our present situation this means that the Chebychev moments μ_m are multiplied by certain *kernel factors* g_m that usually depend on the truncation number M and on the order of the Chebychev moment m (and sometimes on additional parameters).

The *Dirichlet kernel* resembles the trivial case where all kernel factors are equal to 1,

$$g_m^{\mathrm{D}} = 1 \tag{3.28}$$

i.e. the Chebychev moments are not modified. Beyond the different choices, the best known kernel for the calculation of the LDOS and the DOS is the *Jackson kernel* [WWAF06],

$$g_m^{\mathrm{J}} = \frac{(M-m+1)\cos\frac{\pi m}{M+1} + \sin\frac{\pi m}{M+1}\cot\frac{\pi}{M+1}}{M+1} \quad . \tag{3.29}$$

Figure 3.4 illustrates the damping effect of different kernels on spectra containing δ-functions or step functions.

3.2.6. Reconstruction of the target function

An outstanding property of the KPM is given by the fact that as soon as the Chebychev moments μ_m are calculated, the spectral quantity of interest can be evaluated across the whole spectrum at once, without much additional computational effort. We use the standard form of the expansion (3.3) to reconstruct the target function, although there exist ways to further improve the efficiency of this part of the algorithm [WWAF06]. Using the cosine-like form of the Chebychev polynomials, it is possible to use a fast cosine transform (FCT) algorithm for the reconstruction of the target function by choosing a cosine-like spectral variable. If no FCT algorithm is at hand, the problem can also be mapped to an alternative form, so that a fast Fourier transform (FFT) can be used instead. However, in the case of an expansion in only one variable, the performance gain is negligible, as the dominant part of the calculation lies in the determination of the Chebychev moments. So, we decided to use the standard form of the expansion (3.3) to retrieve the LDOS. In (Python-based) pseudo-code, an example for the reconstruction algorithm implementing equation (3.3) reads:

```
def std(moments, disc):
    out = numpy.empty(len(disc))
    for i in range(ndisc):
        o[i] = mom[0]
        for j in range(1, limit):
            o[i] += 2 * mom[j]*cos(j * acos(dis[i]))
            o[i] /= pi * sqrt(1 - dis[i] * dis[i])
    return out
```

The energy discretization `disc` can be of any form, in contrast to FCT variants of the reconstruction algorithm, which are usually based on cosine-like discretizations [WWAF06].

3.2.7. Spectral dependence of the energy resolution

Using the Jackson kernel (3.29), a δ-peak at $\tilde{E} = (E - b)/a$ (position within the interval $[-1, 1]$ corresponding to the rescaled spectrum) is well approximated by a Gaussian of width (half width at half maximum, HWHM) [WWAF06, SF09]

$$\tilde{\eta} = \sqrt{\frac{M - \tilde{E}^2(M-1)}{2(M+1)}(1 - \cos(2\phi))} \approx \frac{\pi}{M}\sqrt{1 - \tilde{E}^2 + \frac{4\tilde{E}^2 - 3}{M}} \quad , \tag{3.30}$$

with $\phi = \pi/(M+1)$. Note that for $\tilde{E} = 0$ (also the band center of our models) we have

$$\tilde{\eta} \approx \frac{\pi}{M} \quad , \tag{3.31}$$

so most of the finite-size scaling (FSS) analysis in the coming chapters is not affected by the exact form of (3.30). If one is interested in spectral positions away from $\tilde{E} = 0$, like

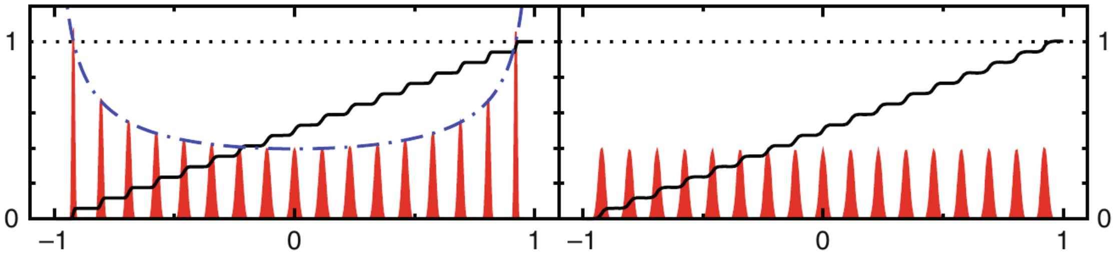

Figure 3.5.: Demonstration of the dependence of of the energy broadening $\tilde{\eta}$ on the spectral position $\tilde{E}$. Shown is the KPM approximation of a series of δ-functions, which are broadened according to (3.30) (left). Using the VMKPM approach, the broadening is kept constant throughout the spectrum (right). The dash-dotted curve is proportional to $1/\tilde{\eta}(\tilde{E}, M)$. From [SF09].

it is the case with the calculation of complete phase diagrams (see section 4.4), one must be aware that $\tilde{\eta}$ may be decreased by up to a factor of about 5 close to the boundaries of the rescaled spectrum, depending on the truncation limit M (see figure 3.5). For some applications, this increase of energy resolution ($\sim 1/\tilde{\eta}$) provided by the KPM may be appreciated, but for our FSS analysis (see chapt. 4), a precise control of the energy broadening η is essential, which is related to the rescaled broadening $\tilde{\eta}$ by the same rescaling relations (3.7) as for the energy E,

$$\eta = a\tilde{\eta} \quad . \tag{3.32}$$

Schubert and Fehske suggested a procedure known as the variable-moment kernel polynomial method (VMKPM) to avoid the $\tilde{E}$-dependence of $\tilde{\eta}$ by using a smaller number of Chebychev moments μ_m for energies away from $\tilde{E} = 0$ [SF09], in correspondence to (3.30). In other words, the truncation limit M becomes a function of the position within the rescaled spectral position, $M(\tilde{E})$. In this way, $\tilde{\eta}$ is kept constant throughout the spectrum.

In this work, the spectral dependence of $\tilde{\eta}$ is ignored. To partly compensate for this, the spectrum boundaries are overestimated by a considerable amount, so that the rescaled spectrum occupies only a small part in the center of the interval $[-1, 1]$. To be specific, we use a fixed energy range of $E/t \in [-24, 24]$ in our calculations ($a = 24t$). The energy spectra of our Hamiltonians usually do not cover more than half of this energy range, so that the variation of $\tilde{\eta}$ towards the band edges due to (3.30) is never greater than about 10 % compared to its value at the band center.

3.3. Ensemble averages

If the model of interest is not describing a strictly periodic lattice, i.e. if it considers some kind of randomness, the significance of using periodic boundary conditions (PBC) (2.5) lies in the fact that the same configuration of random features is repeated in the neighboring supercells. By dividing the crystal into small copies of the supercell, a new periodic symmetry is superimposed to the lattice that does not exist in the real material. To compensate for this lack of randomness that would exist in the thermodynamic limit, $N \to \infty$, the quantity of interest must be ensemble-averaged over a sufficient number N_S of disorder configurations. For large N_S, the same values of observables that would have been measured in the macroscopic material (where the number of lattice sites is quasi-infinite, $N \to \infty$) are then approached in the limit of large sample counts $N_\mathrm{S} \to \infty$.

3.3.1. The arithmetic average of the local density of states

In the absense of disorder, the LDOS is the same at every lattice site of a tight-binding model, and equals the DOS due to the perfect translational symmetry of the lattice. Introducing some form of disorder, this symmetry is broken, and the LDOS at different lattice sites will differ from each other. The DOS can still be approached by obtaining the ensemble average of the LDOS, which is the same as the *arithmetic average* of the LDOS (ALDOS) over different disorder configurations s,

$$\rho_\mathrm{av}(E) = \langle \rho_i(E) \rangle_\mathrm{conf.} = \lim_{S\to\infty} \frac{1}{S} \sum_{s=1}^{S} \rho_i^{(s)}(E) \quad . \tag{3.33}$$

If the correlation of the LDOS between different lattice sites can be neglected, the sample count N_S can be enhanced by considering different lattice sites of the same disorder configuration. The sample count is then the product of the number of disorder configurations S and the number of lattice sites R, $N_\mathrm{S} = SR$.

To be able to estimate the uncertainty of our data, we calculate the sample variance,

$$\sigma_\rho^2(E) = \frac{1}{N_\mathrm{S} - 1} \sum_{i=1}^{N_\mathrm{S}} (\rho_i(E) - \rho_\mathrm{av}(E))^2 \quad . \tag{3.34}$$

As a measure of how good the sample average (3.33) estimates the true average (the population mean), the (sample) standard error (SSE) is considered,

$$s_\rho(E) = \sqrt{\frac{\sigma_\rho^2}{N_\mathrm{S}}} \quad . \tag{3.35}$$

3.3.2. The geometric average of the local density of states

For our analysis it is neccessary to distinguish energy regions of localized states from those of extended states. However, the average density of states (3.33) is not sensitive to the localization character of the electronic eigentstates. Instead, the *typical density of states* can be used, which is the *geometric average* of the LDOS (GLDOS),

$$\rho_\mathrm{typ}(E) = \exp\langle \log \rho_i(E) \rangle_\mathrm{conf.} = \lim_{S\to\infty} \exp \frac{1}{S} \sum_{i=1}^{S} \log \rho_i(E) \quad . \tag{3.36}$$

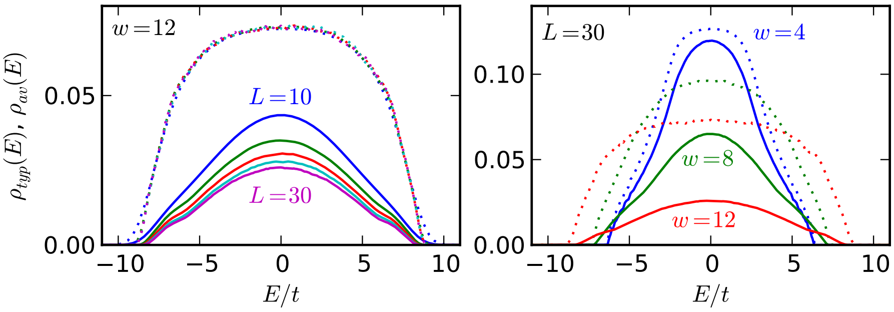

Figure 3.6.: Dependence of the ALDOS and the GLDOS on the truncation limit M and on the system size L, for the 3D Anderson model (2.12) with disorder strength $w = W/t$.

Figure 3.6 shows that it is reduced by both increasing disorder and increasing system size within the whole energy spectrum [JCK12]. In the thermodynamic limit, the GLDOS vanishes in energy regions of localized states, and takes a positive value in energy regions of extended states [SF09]. For finite system sizes however, to which our numerical analysis is limited, the GLDOS will stay positive, even in the case of perfectly localized states.

As a first approximation, one can distinguish energy regions of extended and localized states by defining a cutoff $\rho_{\mathrm{typ}}^{\mathrm{c}}$, like it was done by Schubert and Fehske [SF09], but then the cutoff has to be either chosen arbitrarily, or adjusted to external calibration parameters. This external knowledge could consist of the critical value of one of the disorder parameters of the model, or of the position of one of the mobility edges. Considering a completely new model Hamiltonian that has not been studied before, or being interested in verifying critical values of the model parameters, it is obviously not possible to consider this approach. Because of this, we chose to obtain the GLDOS for different system sizes $N = L^d$ and conduct a FSS analysis, as described in chapter 4.

Again, the sample variance and the standard error are calculated, to assess the numerical error of our findings. The sample variance of the geometric mean can be estimated as (see appendix A) [Nor40]

$$\sigma^2_{\rho_{\mathrm{typ}}}(E) \approx \exp\left(\frac{2}{N_{\mathrm{S}}}\sum_{i=1}^{N_{\mathrm{S}}} \log\rho_i(E)\right)\sigma^2_{\log\rho_i(E)} \quad , \tag{3.37}$$

and for the SSE follows

$$s_{\rho_{\mathrm{typ}}}(E) = \sqrt{\frac{\sigma^2_{\rho_{\mathrm{typ}}}}{N_{\mathrm{S}}-1}} \quad . \tag{3.38}$$

3.3.3. Online algorithms

Our numerical methods are limited to lattices of finite dimensions, as they are based on effective tight binding supercells (see section 2.1). We confine ourselves to cubic lattices with $N = L^d$ sites throughout this work, and measure L in units of the lattice constant $a \equiv 1$, so that L is identical to the number of lattice sites in each dimension. On the other hand, our physical interest lies in the properties of a specimen of macroscopic (quasi-infinitely large) dimensions. To approximate its properties, it is popular in numerical solid state theory to simulate a small snippet of the macroscopic crystal and let it repeat periodically in all spatial dimensions. This is done by applying PBC (2.5) to the small snippet, which allows the electronic wavefunctions $\psi(\mathbf{r})$ to be both extended and normalizable at the same time. The small snippet of the large crystal is what we refer to as a *supercell* (cf. section 2.1).

The formulas (3.33), (3.34), (3.36) and (3.37) assume that the complete set of sample values is already present at the moment of evaluation. However, we decided to use *online versions* of these formulas, which add up values successively in a loop[3]. The average value and variance can be obtained at any point during execution, or after exiting the loop.

By looking carefully at formulas (3.33), (3.34), (3.36) and (3.37), it is apparent that the only values that are neccessary to evaluate to obtain the arithmetic or geometric average including their variance are the four sums,

$$A_1 = \sum_{i=1}^{N_\mathrm{S}} \rho_i \quad , \tag{3.39}$$

$$A_2 = \sum_{i=1}^{N_\mathrm{S}} \rho_i^2 \quad , \tag{3.40}$$

$$B_1 = \sum_{i=1}^{N_\mathrm{S}} \log \rho_i \quad , \tag{3.41}$$

$$B_2 = \sum_{i=1}^{N_\mathrm{S}} (\log \rho_i)^2 \quad , \tag{3.42}$$

plus the sample count N_S[4]. After these five quantities have been obtained successively in a loop, the quantities of interest can easily be calculated,

$$\rho = \frac{A_1}{N_\mathrm{S}} \quad , \tag{3.43}$$

$$\sigma_\rho^2 = \frac{A_2}{N_\mathrm{S} - 1} - \frac{A_1^2}{N_\mathrm{S}(N_\mathrm{S} - 1)} \quad , \tag{3.44}$$

$$\rho_\mathrm{typ} = \exp \frac{B_1}{N_\mathrm{S}} \quad , \tag{3.45}$$

$$\sigma_{\rho_\mathrm{typ}}^2 = \exp \frac{2B_1}{N_\mathrm{S}} \left(\frac{B_2}{N_\mathrm{S} - 1} - \frac{B_1^2}{N_\mathrm{S}(N_\mathrm{S} - 1)} \right) \quad . \tag{3.46}$$

---

[3] Source code at `http://github.com/proggy/oalg/`.

[4] We have left out the energy argument of the densities of states here to avoid clutter. It is clear that all these formulas are valid at every energy independently.

To initialize an averaging process with values from a previously stopped calculation, the quantities A_1, A_2, B_1 and B_2 can be recovered by inverting equations (3.39) til (3.42),

$$A_1 = N_{\mathrm{S}}\,\rho \quad , \tag{3.47}$$

$$A_2 = (N_{\mathrm{S}} - 1)\sigma_\rho + \frac{A_1^2}{N_{\mathrm{S}}} \quad , \tag{3.48}$$

$$B_1 = N_{\mathrm{S}} \log \rho_{\mathrm{typ}} \quad , \tag{3.49}$$

$$B_2 = (N_{\mathrm{S}} - 1)\sigma_{\rho_{\mathrm{typ}}} \exp\left(-\frac{2B_1}{N_{\mathrm{S}}}\right) + \frac{B_1^2}{N_{\mathrm{S}}} \quad . \tag{3.50}$$

In this way, new random variates can simply be added to the sum, i.e. the summands $N_{\mathrm{S}}^{\mathrm{old}} + 1, \ldots, N_{\mathrm{S}}^{\mathrm{new}}$.

Online algorithms possess several advantages:

- Memory usage is minimized, as there are only two floating point values (the sum of values and the sum of squared values) and one integer value (the sample count) that have to be stored. This is especially important when either the sample count is very large, or when many averages have to be computed at the same time (e.g., at different energies of a spectral quantity).

- The averaging process may be stopped at any time, e.g. when the user presses a certain key, a system interrupt occurs, a signal to terminate (e.g. the unix TERM signal) is sent to the process (by either the user or by the administrator), or certain abort criterions are met, like reaching a predefined relative accuracy, a certain date, or an execution time limit.

- The averaging process may be continued at any time, by initializing the process with a previously obtained set of values (average, variance and sample count), for example if a higher accuracy is desired, or to continue after an unwanted system interrupt etc. No data and hence no computation time is wasted.

- Various monitoring features are possible. A measure for the current data accuracy and the current sample count can be monitored in real time. In a future application, a dynamical plot could be shown where the current result (e.g. the density of states) could be monitored, which is updated in real time.

- If the random variates (the LDOS in our case) are calculated first and stored on the hard disc, the additional performance loss due to the disc access times (reading and writing) must be considered[5].

One disadvantage of online algorithms consists in the fact that the random data itself are not preserved. The latter might be of interest for later analysis, for example if an

---

[5] Note that the performance of many computer clusters is often limited just by the network traffic that the processes are causing.

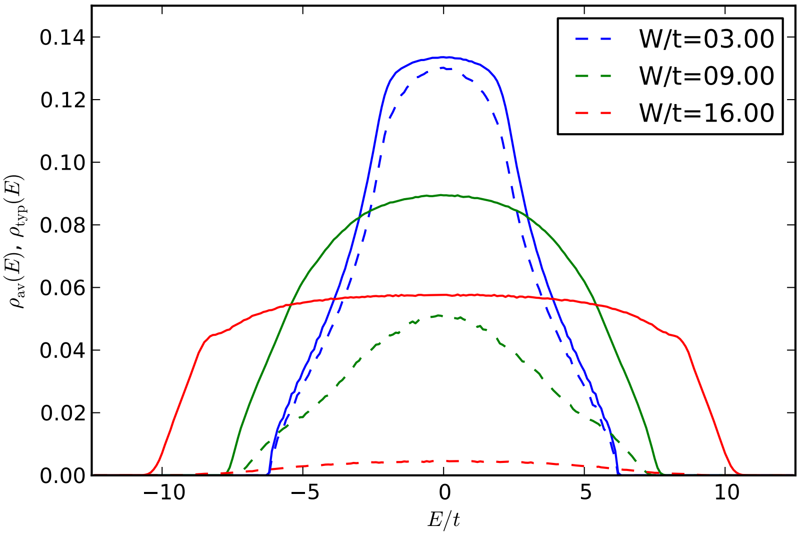

Figure 3.7.: ADOS (continuous line) and GLDOS (dotted line) of the Anderson model for $L = 50$ and $W/t \in \{3, 9, 16\}$. For the ADOS, $R = 10$ start vectors and $S = 240$ disorder realizations have been used. For the GLDOS, the numbers are $R = 32$ and $S = 200$.

analysis of the underlying probability distribution is of interest[6], or possibly for better methods to estimate the statistical error. This depends on the given problem and should be considered carefully before beginning any large scale computations.

3.4. Test results and performance

To validate our implementation of the KPM (section 3.2) as well as of the averaging algorithms (section 3.3), we consider the test case shown in [WWAF06]: For the Anderson model with a fixed system size $N = L^3 = 50^3$ and disorder parameters $W/t \in \{3, 9, 16\}$, we obtain the GLDOS and ADOS shown in figure 3.7 which are very similar to those shown in [WWAF06]. From this observation we conclude that other computations obtained with our implementation can be trusted as well.

The overall performance has been tested in a realistic test calculation for the 3D Anderson model with disorder strength $W/t = 10$. This includes the online algorithms for the GLDOS and the ALDOS (which are executed side by side within the same loop), the creation of a new matrix for each disorder configuration, and the KPM algorithm to obtain the LDOS that is fed to both averaging algorithms in each loop. The system sizes are varied in the range $L \in \{10, 15, \dots, 55\}$. For this test calculation, the local densities of 1 % of the lattice sites are taken into account before a new disorder configuration

---

[6] Although it is possible to formulate online algorithms for histograms just as well.

Table 3.1.: Performance data for a realistic test calculation of 3D Anderson systems. The overall execution time T is measured for different system sizes $N = L^3$. T is averaged over N_C independent calculations, resulting in the standard error s_T.

L	$T[s]$	$s_T[s]$	N_C
10	0.661	0.077	10
15	5.18	0.070	10
20	21.7	3.84	10
25	91.0	16.2	10
30	352	41.8	10
35	1224	23.4	10
40	3290	101	10
45	8326	289	10
50	21295	1112	10
55	48106	776	10

is created and its matrix is constructed. The total sample count is fixed to 2000 for each system size, which means that the larger the system size L, the fewer times a new disorder configuration has to be considered. The results of the timings are presented in table 3.1. To increase accuracy, the timings have been averaged over 10 independent calculations for each system size.

In figure 3.8, the data from table 3.1 is plotted. A fit using the model function

$$T(N) = AN^P \tag{3.51}$$

yields an exponent of $P = 2.86$. At least a quadratic behavior is expected, as the KPM itself should be approximately linear in N, but at the same time the truncation limit M is increased linearly with N in our calculations, which is neccessary for our FSS analysis (see chapter 4). The double-log plot in figure 3.8 reveals that indeed the exponent P appears to be approximately 2 for small system sizes, and is then further increased for large system sizes.

To save some numerical effort, we also take into account the LDOS at different lattice sites of every disorder configuration. This is justified because the correlation of the LDOS values between random sites in a big sample should be small. For the present work, we average over the LDOS of 10 % of the lattice sites of one disorder configuration, so for a system size of $N = L^3 = 1000$, we consider the LDOS of $R = 100$ random sites.

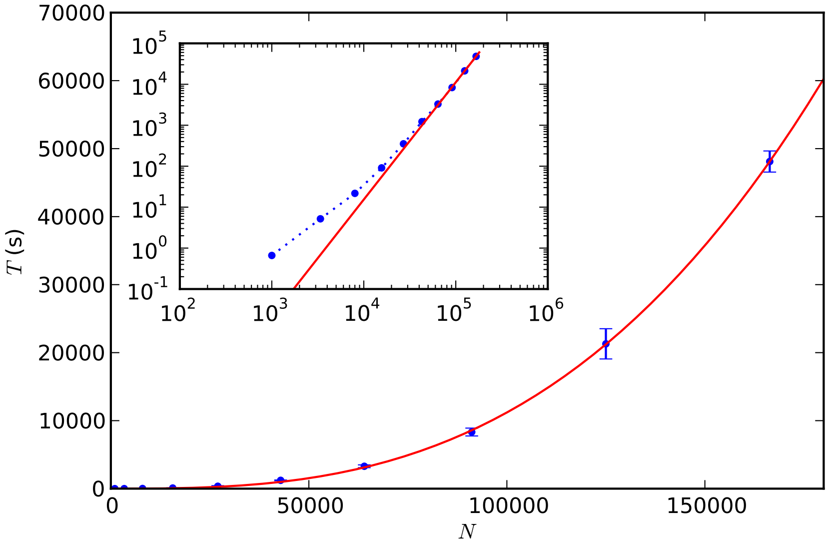

Figure 3.8.: Overall performance of our algorithms when calculating the geometrically and the arithmetically averaged density of states, both in the same loop. For every system size $L \in \{10, 15, \ldots, 55\}$, the local densities of 1% of the lattice sites were taken into account. The truncation limit has been set to $M(L) = L^3/20$. To minimize the error, each execution time T is the average of 10 independent measurements. The errorbars correspond to 95 % confidence intervals. The inset shows a double-log plot of the same data.

4. Finite size scaling of the typical density of states

This chapter tries to answer the question of how the typical density of states $\rho_{\text{typ}}(E)$, i.e. the geometric average of the local density of states (GLDOS), can be used to determine the critical point of a metal-insulator transition (MIT) forming in a disordered electronic system using a finite size scaling (FSS) analysis. The expected scaling of $\rho_{\text{typ}}(E)$ with system size L is thus explored. In essence, we try to motivate a scaling ansatz used by Asada et al. [ASO06] for fitting GLDOS data of a 2D disordered model with symplectic symmetry [ASO04]. The scaling ansatz is then applied to our model of interest in chapter 5.

4.1. Scaling behavior of the wave function intensity

The wave function intensity (WFI) $\left|\psi_k(\mathbf{r})\right|^2$ is known to scale differently with system size L, depending on the localization character of the corresponding states at a particular energy E. Three cases must be distinguished:

1. On the insulating side of the critical point, all states are localized. For a perfectly localized state, the WFI being a δ-function at a certain point $\mathbf{r}$, the WFI is

   $$\left|\psi_k(\mathbf{r})\right|^2 = 1 \tag{4.1}$$

   in the thermodynamic limit. For a general localized state, the envelope of the wave function $\psi_k(\mathbf{r})$ is decaying exponentially in space with a finite decay length (2.25), the *localization length* ξ_{loc}. The WFI scales like[1]

   $$\left|\psi_k(\mathbf{r})\right|^2 \sim \xi_{\text{loc}}^{-\alpha} \quad . \tag{4.2}$$

   The localization length diverges like

   $$\xi_{\text{loc}} \sim |\varepsilon|^{-\nu} \tag{4.3}$$

   at the critical point, with the *localization length exponent* ν. The *critical regime* is entered as soon as ξ_{loc} exceeds the system dimensions, $\xi_{\text{loc}} > L$.

   ε is some dimensionless measure of the distance to the critical point in the energy-disorder space. In terms of the mobility edge E_{M} (at fixed disorder W), it may be replaced by the *reduced energy*,

   $$\varepsilon = \frac{E_{\text{M}} - E}{E_{\text{M}}} \quad . \tag{4.4}$$

---

[1] For the meaning of α, see section 2.5.

In terms of the critical disorder strength W_c (at fixed energy E), it may be replaced by the *reduced disorder*,

$$\varepsilon = \frac{W_\mathrm{c} - W}{W_\mathrm{c}} \quad . \tag{4.5}$$

2. On the metallic side of the critical point, all states are extended. For a maximally extended state (like a plane wave), the WFI scales like

$$\left|\psi_k(\mathbf{r})\right|^2 \sim L^{-d} \quad . \tag{4.6}$$

Introducing some form of disorder, the states are still extended on the metallic side of the critical point, but there is a *correlation length* ξ_corr, so that the WFI scales like

$$\left|\psi_k(\mathbf{r})\right|^2 \sim L^{-d}\xi_\mathrm{corr}^{d-\alpha} \quad . \tag{4.7}$$

The correlation length diverges like

$$\xi_\mathrm{corr} \sim |\varepsilon|^{-\nu} \tag{4.8}$$

at the critical point. In case of the Anderson metal-insulator transition (AMIT), both the correlation length ξ_corr and the localization length ξ_loc (4.3) scale with the same exponent ν. Both diverge at the critical point. Coming from the metallic side of the transition, the critical regime is entered as soon as ξ_corr exceeds the system dimensions, $\xi_\mathrm{corr} > L$.

3. In the critical regime, the states are multifractal. When ξ_loc and ξ_corr are replaced by L in equations (4.2) and (4.7), the critical regime is entered and the WFI scales like [KMV09]

$$\left|\psi_k(\mathbf{r})\right|^2 \sim L^{-\alpha} \quad , \tag{4.9}$$

with a broad distribution of exponents α at different positions $\mathbf{r}$ [KMV09],

$$P(\alpha) = L^{-\frac{(\alpha-\alpha_0)^2}{4(\alpha_0-d)}} \quad . \tag{4.10}$$

The typical (most probable) value of the WFI scales like [KMV09]

$$\left|\psi_k(\mathbf{r})\right|^2 \sim L^{-\alpha_0} \quad . \tag{4.11}$$

The multifractality is also visible in the moments of the WFI. The qth moment of the WFI scales like [EM08]

$$\left\langle \left|\psi_k(\mathbf{r})\right|^{2q} \right\rangle \sim L^{-d-\tau_q} \quad , \tag{4.12}$$

as can be seen from (2.33) and (2.34), with τ_q being the *mass exponents*. The angle brackets $\langle \ldots \rangle$ denote the ensemble average over different disorder configurations.

Under the assumption that $\Delta_q \approx -\gamma q(q-1)$ with $\gamma \ll 1$ (parabolic singularity spectrum) (2.41), it can be deduced that

$$\left\langle \left|\psi_k(\mathbf{r})\right|^{2q} \right\rangle \sim L^{-d-D_q(q-1)} \approx L^{-dq+(\alpha_0-d)q(q-1)} \tag{4.13}$$

and [KMVS12]

$$D_q \approx d - q(\alpha_0 - d) \quad . \tag{4.14}$$

In the following, we simply write ξ as a replacement for both ξ_{loc} and ξ_{corr}, depending on which side of the Anderson transition is considered (insulating or metallic phase).

4.2. Asymptotic behavior of the typical density of states

In this section, we write the LDOS (3.1) in the continuous space form,

$$\rho(E, \mathbf{r}) = \sum_k \left|\psi_k(\mathbf{r})\right|^2 \delta(E - E_k) \quad , \tag{4.15}$$

where $\mathbf{r}$ is a point in d-dimensional space. For the δ-function we consider a Lorentzian[2] with finite broadening η [ASO06],

$$\delta(E - E_k, \eta) = \frac{1}{\pi} \frac{\eta}{(E - E_k)^2 + \eta^2} \quad . \tag{4.16}$$

The GLDOS generally depends on two scales:

- The length scale L/ξ, set by the extent of the localization/correlation length in relation to the system size L. For $L/\xi < 1$, the critical regime is entered, while for $L/\xi > 1$, the system is either in the metallic or in the insulating regime.
- The energy scale η/Δ, measuring the energy resolution η in relation to the level spacing Δ,

  $$\Delta(E) = \frac{1}{\rho_{\mathrm{av}}(E)\, L^d} \quad . \tag{4.17}$$

  $\rho_{\mathrm{av}}(E)$ is the total density of states (DOS), i.e. the arithmetic average of the LDOS (ALDOS) (4.15) in the thermodynamic limit.

4.2.1. The high-resolution limit

We first consider the limit $\eta/\Delta \to 0$, i.e. the limit of high energy resolution, and the critical region, $L/\xi \to 0$. The energy resolution is inversely proportional to the energy broadening η. In the limit $\eta/\Delta \to 0$, the eigenenergies can be viewed as sharp peaks in the LDOS (4.15), compared to the distance Δ between two of the peaks (see figure 4.1).

---

[2] Within the KPM using the Jackson kernel, a δ-peak is actually best approximated by a Gaussian (see section 3.2.5) [WWAF06], but a Lorentzian is easier to handle analytically.

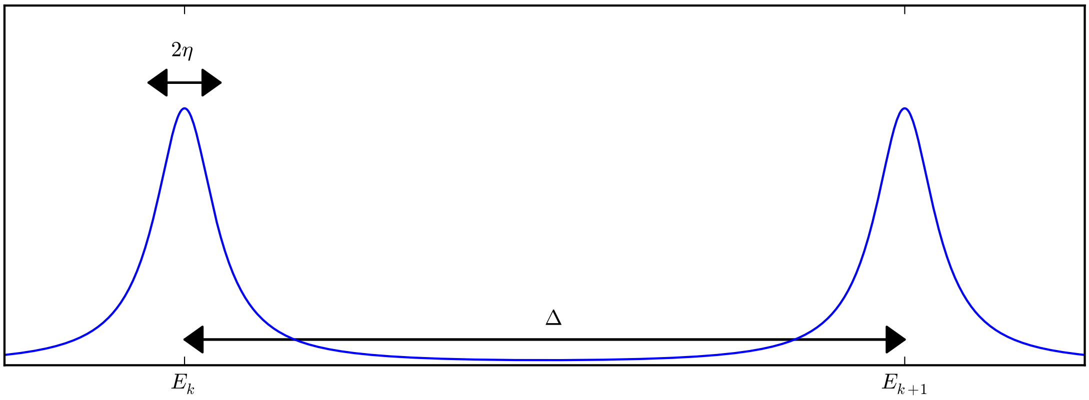

Figure 4.1.: Sketch of the situation in the limit $\eta/\Delta \to 0$.

If we probe a specific energy E, the probability to hit an eigenstate E_k within the interval $[E_k - \eta, E_k + \eta]$ is $2\eta/\Delta$. We make the assumption that as soon as E lies within a radius η around an eigenenergy E_k, the broadened δ-function (4.16) can be replaced by its maximum value,

$$\delta(0,\eta) = \frac{1}{\pi\eta} \quad . \tag{4.18}$$

If E lies outside the radius η (between two eigenstates), we assume the value of the broadened δ-function at a distance of $\Delta/2$ from the eigenstate (i.e., half-way to the next eigenstate),

$$\delta(\Delta/2,\eta) = \frac{1}{\pi}\frac{4\eta}{\Delta^2 + 4\eta^2} \approx \frac{4\eta}{\pi\Delta^2} \quad . \tag{4.19}$$

The last term is an approximation that should be valid in the limit $\eta \ll \Delta$.

The geometric average of the LDOS (GLDOS) is given by

$$\rho_{\mathrm{typ}}(E,\mathbf{r}) = \exp\langle\log\rho(E,\mathbf{r})\rangle \quad , \tag{4.20}$$

i.e. it includes the ensemble average over the LDOS $\rho(E,\mathbf{r})$. Following the above assumptions, we can evaluate the ensemble average and get

$$\log\rho_{\mathrm{typ}}(E,\mathbf{r}) \sim \frac{2\eta}{\Delta}\log\left(L^{-\alpha_0}\frac{1}{\pi\eta}\right) + \left(1 - \frac{2\eta}{\Delta}\right)\log\left(L^{-\alpha_0}\frac{4\eta}{\pi\Delta^2}\right) \quad . \tag{4.21}$$

Here, we assume that on average, the WFI $\left|\psi_k(\mathbf{r})\right|^2$ scales like $L^{-\alpha_0}$ (4.11), which is reasonable because we consider the ensemble average over many LDOS. Equation (4.21) can be further simplified,

$$\rho_{\text{typ}}(E,\mathbf{r}) \sim \exp\left(\frac{2\eta}{\Delta}\log\left(L^{-\alpha_0}\frac{1}{\pi\eta}\right)\right)\exp\left(\left(1-\frac{2\eta}{\Delta}\right)\log\left(L^{-\alpha_0}\frac{4\eta}{\pi\Delta^2}\right)\right) \tag{4.22}$$

$$= \left(L^{-\alpha_0}\frac{1}{\pi\eta}\right)^{\frac{2\eta}{\Delta}}\left(L^{-\alpha_0}\frac{4\eta}{\pi\Delta^2}\right)^{1-\frac{2\eta}{\Delta}} \tag{4.23}$$

$$= L^{-\alpha_0}\frac{1}{\pi}\eta^{1-\frac{4\eta}{\Delta}}\Delta^{-2+\frac{4\eta}{\Delta}} \tag{4.24}$$

$$\approx L^{-\alpha_0}\frac{\eta}{\pi}\frac{1}{\Delta^2} \tag{4.25}$$

$$= \frac{1}{\pi}L^{2d-\alpha_0}\eta\rho_{\text{av}}^2(E) \quad . \tag{4.26}$$

The last two lines should again be a valid approximation in the limit $\eta/\Delta \to 0$.

4.2.2. Medium energy resolution

Before considering the low-resolution limit, $\eta/\Delta \to \infty$, we must turn our attention to the case of “medium” energy resolution. By this we mean the case where $4\eta/\Delta \gtrsim 1$, so that the quantity $2\eta/\Delta$ can be seen as the approximate number of states contained within the interval $[E_k - 2\eta, E_k + 2\eta]$ around an eigenstate E_k. Those states are the only ones that contribute considerably to the value of the LDOS (4.15). On the other hand, we still want η/Δ to be small enough so that a Lorentzian of width η at the critical point is only covering critical states. The case where the Lorentzian is exceeding than the critical region – so that localized and extended states mix in – will be covered in the next section. We still consider the critical point, i.e. $L/\xi \to 0$.

As soon as $4\eta/\Delta \gtrsim 1$, the probing energy E can never lie “between two Lorentzians”, due to the strong overlap between adjacent Lorentzians. So the GLDOS should scale like

$$\rho_{\text{typ}}(E,\mathbf{r}) \sim \exp\left\langle \log\left(\frac{2\eta}{\Delta}L^{-\alpha_0}\frac{1}{\pi\eta}\right)\right\rangle \tag{4.27}$$

$$= \frac{2\eta}{\Delta}L^{-\alpha_0}\frac{1}{\pi\eta} \tag{4.28}$$

$$= \frac{2}{\pi}L^{d-\alpha_0}\rho_{\text{av}}(E) \quad . \tag{4.29}$$

So, the GLDOS is approximately decreasing like L^{-1}, as $d = 3$ and $\alpha_0 \approx 4$ [RVSR11].

4.2.3. The low-resolution limit

In the low resolution limit, the width η of a broadened eigenenergy peak within the LDOS becomes infinitely large. At a certain value η_c, it covers the whole critical region. Beyond this value, it even covers localized and extended states that lie outside the critical region. So the value of the LDOS assumed in section 4.2.1 for a critical state is not sufficient

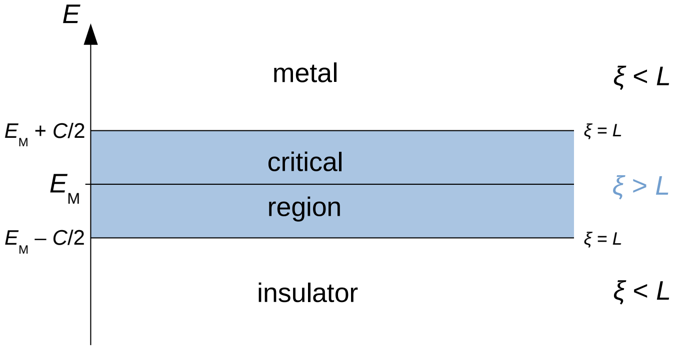

Figure 4.2.: The situation for large η/Δ. If the width of the Lorentzian centered at the mobility edge E_M is larger than the width C of the critical region, it also captures localized and extended states below and above the critical region.

anymore. In fact, because the sum is to take over all states k in the definition of the LDOS (4.15), it is tedious to estimate its value in the low resolution limit in this way[3]. In the following, we try to estimate the critical width η_c for which non-critical states start to mix into the value of the LDOS at the mobility edge E_M. Figure 4.2 illustrates the situation in form of an energy level diagram.

To estimate the critical energy broadening η_c, we first note that the number N_c of critical states (number of states within the critical region) is given by

$$N_\mathrm{c} = \frac{C}{\Delta} \quad , \tag{4.30}$$

where we assumed that Δ does not change much within the critical region around E_M. C is the width of the critical region which is assumed to extend symmetrically around the mobility edge E_M (see figure 4.2). Directly at the boundary of the critical region, we know that $\xi = L$. As ξ diverges at the mobility edge (4.3), we can conclude that

$$\begin{aligned} \left|\frac{C}{2}\right|^{-\nu} &\sim L \quad , \\ C &\sim 2L^{-\frac{1}{\nu}} \quad , \\ N_\mathrm{c} = \frac{C}{\Delta} &\sim 2L^{d-\frac{1}{\nu}} \quad . \end{aligned} \tag{4.31}$$

In our calculations (chapter 5), we keep the product ηL^d fixed (we use $\tilde{\eta}L^d = 20\pi$). To know if η is already large enough to cover also localized and extended states, which would then contribute to the value of the LDOS, we have to compare our value ηL^d with the theoretical value $\eta_\mathrm{c}L^d$. To be able to provide an absolute number would require knowledge about the absolute localization length in equation 4.3.

---

[3] One can however argue that by taking the sum over all energies, the classical result is approached, which suggests a scaling like $\Gamma L^{\alpha_0 - d} \sim L^{\alpha_0 - d}$.

As $\nu \approx 1.6$ [RVSR11], we know that[4]

$$\eta_{\mathrm{c}} L^d \sim 2L^{2.4} \quad . \tag{4.32}$$

In general, it is advisable to not go far beyond the value $4\eta/\Delta \gtrsim 1$, because then, the assumptions of the medium resolution regime (section 4.2.2) can still be used. For our calculations, we fix $L^3/M = 20$, so

$$\frac{4\eta}{\Delta} = \frac{4 \cdot 24t\tilde{\eta}}{\Delta} = 4 \cdot 24t\pi\rho_{\mathrm{av}}\frac{L^d}{M} \approx 4 \cdot 24\pi \approx 300 \tag{4.33}$$

For this estimate, we use equation (3.31) by considering a Chebychev expansion (3.3) with M moments at $E = 0$, and for the value of the DOS near the critical disorder we assume $\rho_{\mathrm{av}}(0) \cdot t \approx 0.05$ (see figure 2.3). η is related to the rescaled $\tilde{\eta}$ via (3.32). As (4.33) shows, our calculated data lies far beyond $4\eta/\Delta = 1$, and we therefore cannot exclude the possibility that we are already mixing in localized and extended states from outside the critical region. We recommend that future calculations should consider a lower value of $4\eta/\Delta$, by at least one order of magnitude. On the other hand, it must be kept in mind that the numerical effort would be increased by the same factor.

4.3. Scaling ansatz for the typical density of states

As already stated in section 4.2, the GLDOS should only depend on the length scale L/ξ and on the energy scale η/Δ. Further, it is known that at the critical point, the GLDOS scales like [Jan98]

$$\rho_{\mathrm{typ}} \sim L^{d-\alpha_0} \quad . \tag{4.34}$$

Based on this, we consider a scaling ansatz for the GLDOS also used by Asada et al. [ASO06], who successfully applied it to the two-dimensional SU(2) model [ASO04, ASO05] which also exhibits an AMIT[5]. The scaling ansatz reads

$$\Gamma = L^{d-\alpha_0} F(L/\xi, \eta/\Delta) \quad , \tag{4.35}$$

which is equivalent to

$$\Gamma = L^{d-\alpha_0} \bar{F}(\varepsilon L^{\frac{1}{\nu}}, \rho_{\mathrm{av}}\eta L^d) \quad . \tag{4.36}$$

$\Gamma(E)$ is the ratio of typical and average density of states,

$$\Gamma(E) = \frac{\rho_{\mathrm{typ}}(E)}{\rho_{\mathrm{av}}(E)} \quad . \tag{4.37}$$

ε can be the reduced energy (4.4) or the reduced disorder (4.5). $F(x, y)$ is in general an unknown function, but we can at least assume continuity. To substantiate the scaling ansatz (4.36), we are going to confirm its validity numerically for the case of the three-dimensional Anderson model (2.12) at half filling in the coming sections.

---

[4] L is measured in units of the lattice spacing a, i.e. it corresponds to the number of lattice sites in one dimension.

[5] This is possible in 2D for systems belonging to the symplectic symmetry class (see section 2.4).

Table 4.1.: Fit results for the scaling ansatz (4.39) considering the Anderson model at $E = 0$ and for $15 \leq W/t \leq 18.5$ and $10 \leq L \leq 50$. The GLDOS is averaged over $N_\mathrm{S} = 160000$ LDOS spectra, while for the ADOS, $R = 10$ random-phase vectors are used and it has been averaged over $S = 2500$ disorder realizations. The fit parameters are given together with the standard deviation estimated by the fit algorithm. To assess the quality of the fit, the reduced χ^2 statistic is given.

F_0	F_1	F_2	W_c/t	α_0	ν
0.06 ± 0.01	0.95 ± 0.07	5.12 ± 0.14	16.19 ± 0.10	4.01 ± 0.01	1.17 ± 0.03
$\chi^2_\mathrm{red} = 5.07$					

4.3.1. Verification of the scaling ansatz: The first argument

We consider the Anderson model (2.12) in the following, using a box distribution (2.11) of width W for the random site potentials. To verify the dependence of the scaling ansatz (4.36) on its first argument $x = \varepsilon L^{\frac{1}{\nu}}$, it seems natural to keep the second argument $y = \rho_\mathrm{av}\eta L^d$ fixed to a constant value. However, to be able to calculate the GLDOS and the ALDOS at the same time, we decide to only keep the product ηL^d fixed. To be more specific, we fix $L^d/M = 20$, using M Chebychev moments within the KPM (see section 3.2). So $\eta L^d = 24t\tilde{\eta}L^d = 24t\pi L^d/M = 24t\pi \cdot 20 \approx 1500t$. For a future work, the ADOS should be calculated in advance using the efficient KPM algorithm for the DOS (see section 3.2.4), and then the truncation limit M should be adjusted when calculating the GLDOS so that the whole argument $y = \rho_\mathrm{av}\eta L^d$ is kept constant.

The ALDOS $\rho_\mathrm{av}(E)$, which is approaching the value of the total DOS in the thermodynamic limit, depends not only on the energy E, but also on the disorder strength W. Within the considered range of disorder values, $W/t \in \{15 \dots 18.5\}$, the value of $\rho_\mathrm{av}(0)$ is changed by about 20 % (see figure 4.3). Still, we neglect the disorder dependence for now[6], and are then left only with the first argument of the function $F(x, y) \equiv \tilde{F}(x)$. We expand $\tilde{F}(x)$ in a power series to second order in x [ASO06],

$$\tilde{F} = F_0 + F_1 x + F_2 x^2 \quad . \tag{4.38}$$

Fitting our data for $\rho_\mathrm{typ}(0)$ and $\rho_\mathrm{av}(0)$ at $E = 0$ for different system sizes $L \in \{10, \dots, 50\}$ and different disorder values $W/t \in \{15, \dots 18.5\}$, we can apply a least-squares (χ^2) fitting procedure to the function

$$\Gamma(W, L) = L^{\alpha_0 - d}\tilde{F}(\varepsilon L^{\frac{1}{\nu}}) \tag{4.39}$$

with the six fitting parameters $(F_0, F_1, F_2, W_\mathrm{c}, \alpha_0, \nu)$ and $d = 3$. The fitting results are summarized in table 4.1.

Figure 4.4 shows a plot of the data, rescaled to $\Gamma L^{\alpha_0 - d}$ versus $\varepsilon L^{\frac{1}{\nu}}$ or $|\varepsilon| L^{\frac{1}{\nu}}$, respectively, using the fit parameters shown in table 4.1. As predicted by the scaling

---

[6] The results appear to be only mildly influenced if we consider the disorder-dependence of $\rho_\mathrm{av}(E)$ to linear order in the fit.

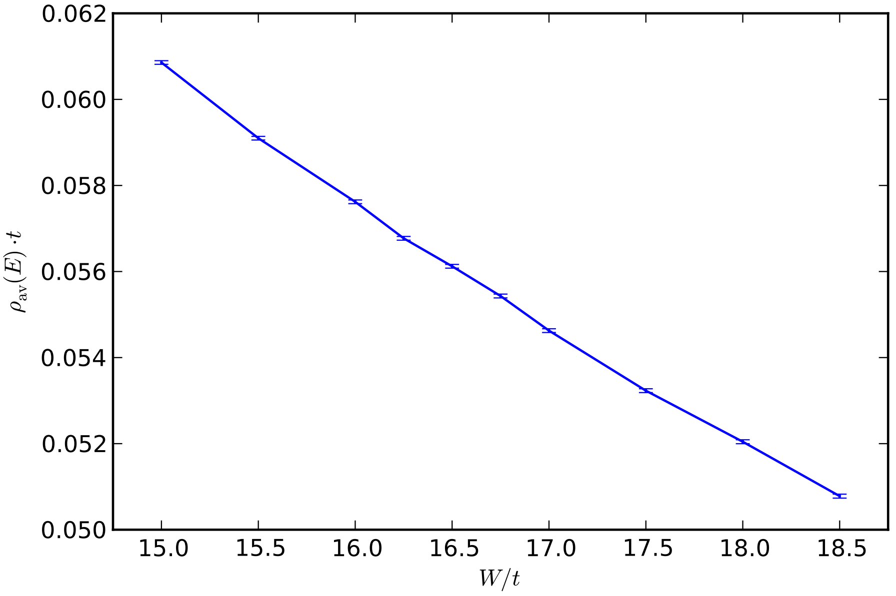

Figure 4.3.: Disorder-dependence of the ADOS at $E = 0$ within the considered range of disorder values W/t around the expected critical disorder $W_\mathrm{c}/t \approx 16.5$. The system size is $L = 50$, and the truncation limit is $M = L^3/20 = 6250$.

ansatz (4.36), the data indeed falls onto one curve. So, the general applicability of equation (4.36) with respect to the first argument of $F(x, y)$ is verified for the 3D Anderson model at half filling. Also, the second-order expansion for $\tilde{F}(x)$ (4.38) seems to be sufficient. However, the precision of some data points could be further improved.

4.3.2. Verification of the scaling ansatz: The second argument

We now consider the case where we are directly at the critical point, so ξ is diverging, $\xi \to \infty$, and hence the first argument in equation (4.36) is identical to zero. Only the second argument remains, $F(x, y) \equiv \tilde{f}(y)$, and equation (4.36) becomes

$$\Gamma(L, M) = L^{d-\alpha_0} \tilde{f}(\rho_{\mathrm{av}} \eta L^d) \quad . \tag{4.40}$$

Calculating data for the 3D Anderson model (2.12) at $E = 0$ and $W/t = 16.5$, which should be close to the critical point [RVSR11], results in figure 4.5. Note that $\rho_{\mathrm{av}} = \mathrm{const}$ for $E = \mathrm{const}$ and $W = \mathrm{const}$, and $\eta \approx \pi/M$ at $E = 0$ (3.31). Evidently, the data points form a continuous function of L^d/M or, alternatively, ηL^d. We thereby conclude that the scaling ansatz (4.36) is also valid for scaling with its second argument, and can confirm its applicability to the 3D Anderson model at criticality and half filling.

Furthermore, by plotting the data in a double-logarithmic form in figure 4.5, it becomes evident that the unknown function $f(\log y)$,

$$\log(\Gamma L^{\alpha_0 - d}) = f(\log(\rho_{\mathrm{av}} \eta L^d)) \quad , \tag{4.41}$$

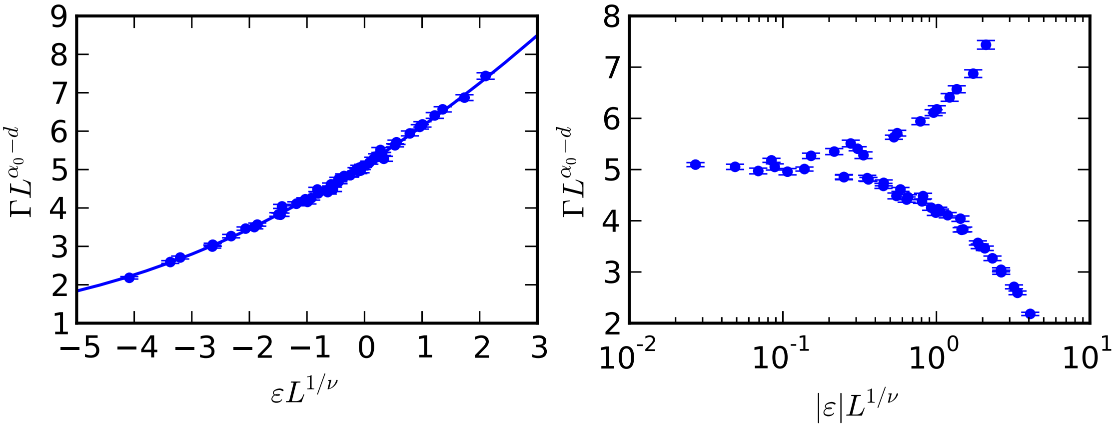

Figure 4.4.: Demonstration of the scaling ansatz (4.36) with respect to the first argument of the function $F(x, y)$, applying it to the Anderson model at $E = 0$ for $15 \leq W/t \leq 18.5$ and $10 \leq L \leq 50$. The GLDOS is averaged over $N_S = 160000$ LDOS spectra, while for the ADOS, $R = 10$ random-phase vectors and $S = 2500$ disorder realizations are used.

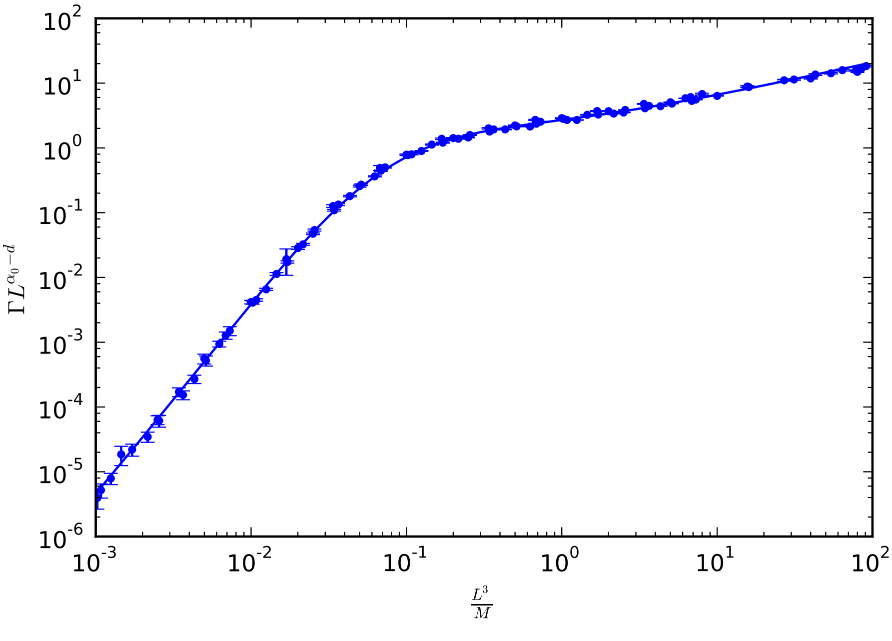

Figure 4.5.: Demonstration of the scaling ansatz (4.36) with respect to the second argument of the function $F(x, y)$.

has two slant asymptotes with the slopes Θ_L for $L^d/M \ll 1$ and Θ_R for $L^d/M \gg 1$. This suggests a fit model describing a smooth transition between two intersecting straight lines [BW71],

$$f(\tilde{y}) = a_0 + a_1(\tilde{y} - \tilde{y}_0) + a_2(\tilde{y} - \tilde{y}_0)\, T(\tilde{y} - \tilde{y}_0) \quad , \tag{4.42}$$

where a_1 is the average slope,

$$a_1 = \frac{\Theta_\mathrm{L} + \Theta_\mathrm{R}}{2} \quad , \tag{4.43}$$

and a_2 is half the difference between the slopes Θ_L and Θ_R,

$$a_2 = \frac{\Theta_\mathrm{L} - \Theta_\mathrm{R}}{2} \quad , \tag{4.44}$$

$T(\tilde{y})$ is the *transition function.* If the sign function is used, $T(\tilde{y}) = \mathrm{sgn}(\tilde{y})$, with

$$\mathrm{sgn}(\tilde{y}) = \begin{cases} 1 & , \quad \tilde{y} > 0 \\ 0 & , \quad \tilde{y} = 0 \\ -1 & , \quad \tilde{y} < 0 \end{cases} \quad , \tag{4.45}$$

a sharp transition at $\tilde{y}_0$ between the two straight lines is obtained. To smoothen the transition, smoothed estimates of the sign function (4.45) have to be found. There are several good choices for such a function [BW71]. We favorize the hyperbolic tangent $\tanh(\kappa x)$, as it approaches ±1 for $x \to \pm\infty$. The parameter κ is a measure for the “smoothness” of the transition and has to be fitted to the data. In figure 4.6, our choice for the transition function $T(\tilde{y})$ is compared to the sign function (4.45) and to a Lorentzian of the form $m\kappa/(\tilde{y}^2 + \kappa^2)$ with an additional parameter m.

The total fit model reads

$$\Gamma(L, M) = L^{d-\alpha_0} \exp \tilde{f}(\log \frac{L^d}{M}) \quad . \tag{4.46}$$

The complete set of fit parameters is $(a_0, a_1, a_2, \alpha_0, \kappa, \tilde{y}_0)$, and $d = 3$ is a constant. The fit results are summarized in table 4.2. From the fit parameters, the slopes of the two slant asymptotes can easily be calculated,

$$\Theta_\mathrm{L} = a_1 + a_2 \quad , \quad \Theta_\mathrm{R} = a_1 - a_2 \quad . \tag{4.47}$$

In this way, we obtain the slopes $\Theta_\mathrm{L} = 2.74 \pm 0.11$ and $\Theta_\mathrm{R} = 0.54 \pm 0.11$. The value $\alpha_0 = 4.23 \pm 0.02$ agrees quite well with the established numerical value $4.048(4.045, 4.050)$ [RVSR11], as well as with the analytic prediction (2.44).

At this point, a comparison of the slopes with the analytical predictions from sections 4.2.1 and 4.2.2 seems appropriate. Rearranging (4.26) yields

$$\Gamma L^{\alpha_0 - d} \sim \rho_\mathrm{av} \eta L^d \quad , \tag{4.48}$$

so according to this estimate, in a double-logarithmic plot, the left slope should be $\Theta_\mathrm{L} = 1$. Unfortunately, we find a much higher slope of $\Theta_\mathrm{L} = 2.74 \pm 0.11$. At least, our

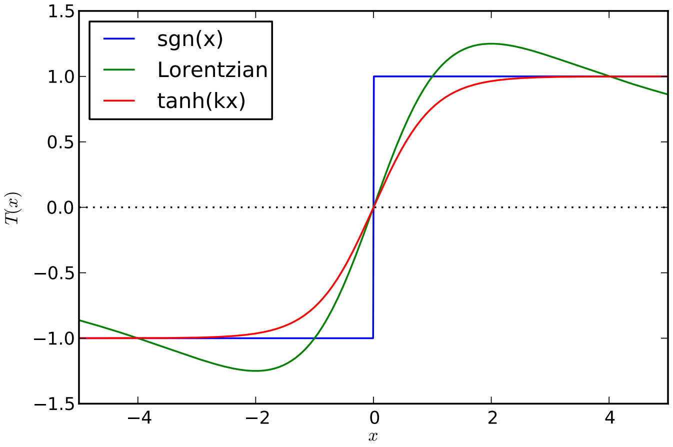

Figure 4.6.: Comparison between different choices for the transition function $T(\tilde{y})$. The signum function $\mathrm{sgn}(\tilde{y})$ corresponds to the non-smoothed limit of the transition functions. The shown Lorentzian has the parameters $\kappa = 2$ and $m = 5$, and the hyperbolic tangent has $\kappa = 1$.

Table 4.2.: Fit results of the fit model (4.46).

a_0	a_1	a_2	α_0	κ	$\tilde{y}_0$
-0.88 ± 0.14	1.64 ± 0.06	1.10 ± 0.05	4.23 ± 0.02	-2.12 ± 0.14	-2.69 ± 0.09

$\chi^2_{\mathrm{red}} = 87.5$

analytic estimation is able to explain the slope in the findings of Asada et al. for a 2D system with symplectic symmetry [ASO06], where they indeed find a slope close to 1.

For medium resolution, equation (4.29) seems to suggest a constant,

$$\Gamma L^{\alpha_0 - d} \sim \frac{2}{\pi} \quad . \tag{4.49}$$

Anyway, we obtain a steadily increasing function in the double-logarithmic plot, as well as Asada et al. does [ASO06]. For the low resolution limit (section 4.2.3) we approach the classical result $\Gamma L^{\alpha_0 - d} \sim L^{\alpha_0 - d}$, so the slope in the double-logarithmic plot $\Gamma L^{\alpha_0 - d}$ vs. ηL^d should be $(\alpha_0 - d)/d$. This seems to be realized quite well in our case of the 3D Anderson model, as well as in the 2D symplectic case investigated by Asada et al. [ASO06].

4.4. Empirical scaling ansatz

If the value of the second argument $y = \rho_{\mathrm{av}} \eta L^d$ is kept constant and we consider a position in phase space directly at the critical point, i.e. $\varepsilon = 0$, then both arguments of the unknown function $F(x, y)$ are constant. Hence, also the function value of $F(x, y)$ is a constant, $F(x, y) = F_0$. The only remaining part in the scaling ansatz (4.36) then is [Jan98]

$$\Gamma(L) = L^{d - \alpha_0} F_0 \quad . \tag{4.50}$$

So at least directly at the critical point, the scaling of Γ (or ρ_{typ}) with system size L is known to have this simple form. However, away from the critical point ($\varepsilon \neq 0$), the scaling with L is generally unknown, and may be non-trivial, as it enters both function arguments of $F(x, y)$. Also, in the metallic regime, the GLDOS is expected to approach a non-zero value in the thermodynamic limit $L \to \infty$, which the simplistic scaling ansatz (4.50) does not allow for.

Nevertheless, we try to use the empirical scaling ansatz [JCK12]

$$\rho_{\mathrm{typ}}(L) = F_0 L^{-p} \tag{4.51}$$

for fixed W and fixed E to estimate the phase transition in the whole energy-disorder plane, i.e. to obtain the whole phase diagram of disorder [JCK12]. According to (4.50), directly at the critical point, it should be fulfilled for $p = \alpha_0 - d$. So by obtaining data for different system sizes L, one should be able to identify the mobility edges E_{M} for every fixed W using the cutoff

$$p_{\mathrm{c}} = \alpha_0 - d \quad . \tag{4.52}$$

However, because of the non-trivial scaling form away from the critical point, there is no guarantee that the same exponent $p = \alpha_0 - d$ is not found again at energies away from the mobilitiy edge E_{M}, which could lead to ambiguities in the determination of the phase trajectory in certain parts of the phase diagram. Another caveat is that we only keep the product $\eta L^d = \text{const}$ in our calculations, whereas we neglect the dependence of $\rho_{\mathrm{av}}(E)$ on disorder and energy. At least the latter is of course not justifiable, as the DOS even drops to zero towards the band edges (see figure 2.3).

Accepting the above restrictions, the whole phase diagram of disorder can easily be obtained when the two-dimensional function $p(E,W)$ is evaluated for the full range of energy and disorder values. Then, the phase trajectory is given by the contour

$$p(E,W) = p_{\mathrm{c}} \tag{4.53}$$

i.e. the contour emerging when cutting the two-dimensional function $p(E,W)$ with a horizontal plane at $p = p_{\mathrm{c}}$.

This procedure has been applied to the Anderson model in figure 4.7. The 95 % confidence region is depicted by the gray shaded area, which can be approximated by the area between the two contours

$$p(E,W) \pm 1.96\,\sigma_p(E,W) = p_{\mathrm{c}} \quad , \tag{4.54}$$

where $\sigma_p(E,W)$ is the estimated standard deviation of the parameter p provided by the fit algorithm, at position (E,W) in the phase diagram. Intriguingly, despite the vigorous assumptions above, our result for the quantum phase diagram for the Anderson model already reveals many expected properties when comparing it to established results [BSK87, KM93, SF09] (cf. figure 2.6):

- For zero disorder, $W = 0$, the mobility edges E_{M} coincide with the band edges.
- For increasing disorder, the band broadens, and localized states appear in the band tails.
- The *reentrance behavior* is reproduced.
- The critical disorder at half filling ($E = 0$) is found roughly at $W_{\mathrm{c}}/t \approx 16.5$.

On the downside, the phase diagrams in the literature are not accurately reproduced. Differences include:

- We do not quite find the expected value for the critical disorder in the band center $E = 0$, which is known to be close to $W_{\mathrm{c}}/t \approx 16.5$ [BSK87, KM93]. A recent investigation found $W_{\mathrm{c}}/t = 16.530(16.524, 16.536)$ with high precision [RVSR11]. We usually find values below, e.g. $W_{\mathrm{c}}/t \approx 16.3$, although the overall accuracy of this method is not high enough to make a more accurate statement.
- The turning points of the phase trajectory at high absolute energy are somewhat different from previous calculations [BSK87, SF09], which appear around $E/t = [-8, 8]$ in our case. As the energy-dependence of the DOS $\rho_{\mathrm{av}}(E)$ is hardly negligible, the results far away from the band center are expected to be highly unreliable anyway.

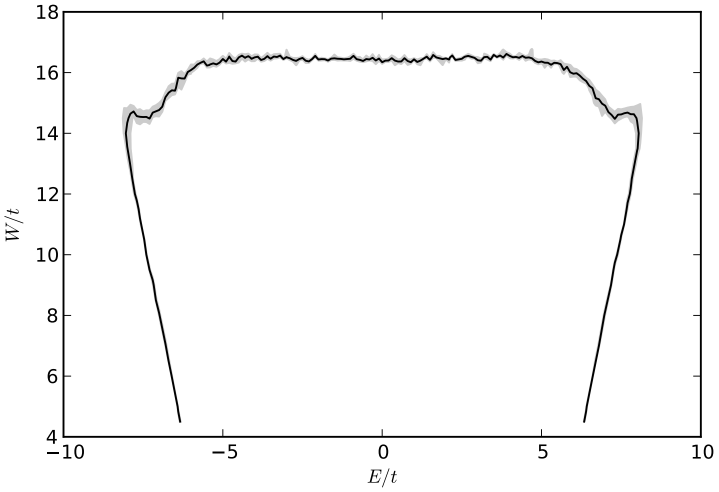

Figure 4.7.: Quantum phase diagram of the Anderson model (2.12) in the disorder-energy plane as obtained by the empirical scaling ansatz (4.51) and the condition (4.53). The shaded region depicts the 95 % confidence region according to (4.54).

- There are some kind of plateaus forming near the high energy turning points, which has also been found by Schubert and Fehske [SF09] using KPM but no FSS analysis. These plateaus are not found in any other predictions for the phase diagram of the Anderson model [BSK87, ETT$^+$14].

  The plateaus show the tendency to form small peaks, splitting the phase diagram into three regions (six mobility edges) for certain values of W. This behavior seems to disappear as soon as the accuracy of the data reaches a certain level. As discussed above, there is no guarantee that the cutoff value p_c is not crossed again away from the critical point, which could cause this phenomenon.

In section 5.4, this approximative method to estimate the phase diagram based on the empirical scaling ansatz (4.51) is applied to the Anderson-Heisenberg model (5.2).

5. Effective model for the impurity band electrons of phosphorus-doped silicon

To study the metal-insulator transition (MIT) in phosphorus-doped silicon (Si:P), which is driven by both interaction and disorder, the Anderson-Hubbard model (2.50) can be considered, as it possesses all the necessary ingredients: It describes interacting electrons in a disordered potential, and the interaction may give rise to the formation of magnetic moments if the parameters are chosen correctly. However, theoretical studies often have to compromise between completeness of a model and numerical effort. Hence, we choose a variant of the Anderson-Hubbard model that gets along with a single-particle description. The model is described in the following section. Later in this chapter, results for the model will be presented, which have been obtained using the numerical methods and concepts introduced in the previous chapters.

5.1. The Anderson-Heisenberg model

The local magnetic moments in Si:P emerge from impurity states that are occupied by only one electron in the groundstate. In some theoretical approaches, the local moment formation is separated from the itinerant electrons in the impurity band by considering localized spins (*two-fluid model*) [PGBS88, MSB89, Sac89]. We build on this idea by replacing the Hubbard term in equation (2.50) by a term describing an exchange coupling between the impurity band electrons and a finite concentration of classical magnetic impurities. We further place the donor states on a regular grid (3D simple-cubic lattice), while in real Si:P, the donor atoms are randomly distributed within the silicon host, as illustrated in figure 5.1. Considering only hoppings to nearest neighbors, we assume a situation in which the overlap is only considerably different from zero in the distance to the nearest neighbors, and negligible for any larger distances.

In essence, the above assumptions come down to an extension of the Anderson model [And58] (cf. section 2.2),

$$\hat{H}_0 = t \sum_{\langle i,j \rangle, \sigma} |j,\sigma\rangle \langle i,\sigma| + \sum_{i,\sigma} \varepsilon_i \, |i,\sigma\rangle \langle i,\sigma| \quad . \tag{5.1}$$

Here, $|i,\sigma\rangle$ denotes an electron state with spin σ located at site i of a 3D cubic lattice with $N = L^3$ sites and periodic boundary conditions (we usually consider $L \in \{10, 20, 30, 40, 50\}$). For the local potentials ε_i, random values are drawn from a box distribution (2.11) of width W, $\varepsilon_i \in [-W/2, W/2]$, while the hopping amplitude t between neighboring lattice sites remains constant. Note that in the pure Anderson model

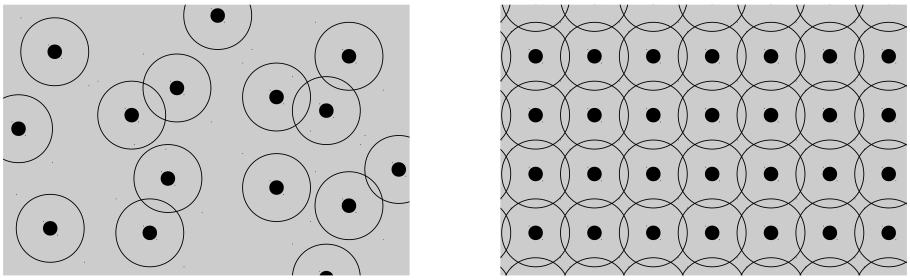

Figure 5.1.: Schematical plot of the hydrogen-like orbitals of phosphorus donors, (a) positioned randomly in the silicon host, and (b) placed on the sites of a lattice, as assumed by the Anderson-Heisenberg model.

(5.1), the spin index σ is redundant as the two spin channels are not connected by off-diagonal (hopping) matrix elements. Hence, each energy eigenvalue will exist twice (double degeneracy).

We add a second term $\hat{H}_\mathrm{s}$ to the Hamiltonian

$$\hat{H} = \hat{H}_0 + \hat{H}_\mathrm{s} \quad , \tag{5.2}$$

which describes a local coupling (at site i) of the electron spin σ_i to a classical magnetic moment $\mathbf{S}_i$ with constant norm $S = 1$, but random orientation (Heisenberg-like), given by the (polar and azimuth) angles θ_i and φ_i. The angles are drawn uniformly from the intervals $\cos\theta_i \in [-1, 1]$ and $\varphi_i \in [0, 2\pi]$. Each σ_i is a vector containing the three Pauli matrices,

$$\sigma_\mathrm{x} = \begin{pmatrix} 0 & 1 \\ 1 & 0 \end{pmatrix} \quad , \quad \sigma_\mathrm{y} = \begin{pmatrix} 0 & -i \\ i & 0 \end{pmatrix} \quad , \quad \sigma_\mathrm{z} = \begin{pmatrix} 1 & 0 \\ 0 & -1 \end{pmatrix} \quad , \tag{5.3}$$

so the general form of the coupling term,

$$\hat{H}_\mathrm{s} = \sum_i J_i \sigma_i \cdot \mathbf{S}_i \quad , \tag{5.4}$$

can be written as

$$\hat{H}_\mathrm{s} = S \sum_{i=1}^{N} J_i \left(\cos\theta_i \sum_{\sigma=\pm 1} \sigma \left| i, \sigma \right\rangle \left\langle i, \sigma \right| + \sin\theta_i \sum_{\sigma=\pm 1} \exp(i\sigma\varphi_i) \left| i, \sigma \right\rangle \left\langle i, -\sigma \right| \right) \quad . \tag{5.5}$$

For this work, we fix the concentration of dopant sites carrying a magnetic moment to $n_\mathrm{M} = 5\,\%$ and only vary the exchange coupling strength J. We note that $n_\mathrm{M} = 5\,\%$ is a realistic value for real materials like Si:P [Sac89, BR81, BL82, MSB89] (cf. section 2.6.5).

J_i is drawn from a binary probability distribution, $J_i \in \{J, 0\}$, taking a nonzero value with probability n_M, for which it conforms to the exchange coupling strength J.

By adding the term (5.5) to the Anderson model (5.1), the spin index σ is no longer redundant. The matrix representation of (5.2) is a $N \times N$ grid of small 2×2 submatrices which represent the two spin states of each impurity band electron. In a matrix representation for the spin, the coupling term (5.5) can be written in the alternative form

$$\hat{H}_\mathrm{s}^\mathrm{M} = S \sum_{i=1}^{N} J_i \begin{pmatrix} \cos\theta_i & e^{i\varphi_i} \sin\theta \\ e^{-i\varphi_i} \sin\theta & -\cos\theta_i \end{pmatrix} |i\rangle \langle i| \quad . \tag{5.6}$$

For comparison, we also study the effect of Ising impurities, substituting the uniform distribution for $\cos\theta_i$ by a uniform binary distribution, $\theta_i \in \{0, \pi\}$. In this case, the complex interaction terms in (5.5) vanish and the Hamiltonian still belongs to the orthogonal symmetry class:

$$\hat{H}_\mathrm{s} = S \sum_{i=1}^{N} J_i \cos\theta_i \sum_{\sigma=\pm 1} \sigma \, |i, \sigma\rangle \langle i, \sigma| \quad . \tag{5.7}$$

Thus, the off-diagonal matrix elements in (5.6) vanish. The Ising impurities only introduce an additional form of disorder, which is expected to lower the critical disorder potential W_c, but not lead to a change of the symmetry class of the model.

5.2. Calculation of the spin-resolved local density of states

To determine the critical point for various combinations of the system parameters (n_M, J, W, L), the numerical methods from chapter 3 are applied to the Hamiltonian (5.2) for both cases, Heisenberg and Ising impurities, independently. Now, the spin-resolved local density of states (SLDOS),

$$\rho_{i,\sigma}(E) = \sum_{k=1}^{2N} \left| \langle i, \sigma | k \rangle \right|^2 \delta(E - E_k) \quad , \tag{5.8}$$

has to be taken into account, i.e. there is an additional index σ for the spin of the impurity band electrons that can take the two values $+1$ and -1 (spin-up and spin-down). The full Hamiltonian (5.2) has $2N$ eigenstates, resulting in a $2N \times 2N$ tight binding matrix.

Note that because of the additional spin index, the calculation of the SLDOS for the Anderson model including Ising impurities doubles the numerical effort for fixed system size L, compared to the pure Anderson model. Including Heisenberg impurities, there is another factor of two in memory demand and computation time, as the matrix elements are now complex, so that there is a total factor of four in the numerical effort compared to the pure Anderson model.

5.3. Shift of the critical disorder due to the exchange coupling

Using the finite size scaling (FSS) approach described in chapter 4, the critical disorder W_c is determined for different exchange coupling strengths J. For this analysis, we fix the energy to the band center, $E = 0$, which is also chosen as the center of the rescaled energy interval used by the KPM, so that (3.31) is an excellent approximation for the energy broadening η, and side effects caused by neglecting the energy-dependency of η do not occur (cf. section 3.2.7). In the scaling form (4.36) [ASO06] we fix the ratio $L^d/M = 20$. Neglecting the disorder-dependence of the ALDOS $\rho_{\mathrm{av}}(\mathrm{E})$, the function $F(x, y)$ then depends only on its first argument, $x = \varepsilon L^{1/\nu}$. In general, ε can be any dimensionless measure for the distance to the critical point within the disorder-energy space (phase space), but here it is taken as the reduced disorder potential (4.5), while the other three contemplable parameters E, J and n_{M} are kept constant.

We expand the unknown function $F(x)$ to second order in x using a power series (4.38), so in total our fit model (4.36) contains one dependent variable $\Gamma = \rho_{\mathrm{typ}}/\rho_{\mathrm{av}}$, two independent variables W and L, and six fit parameters $(W_{\mathrm{c}}, \alpha_0, \nu, F_0, F_1, F_2)$, plus the constant $d = 3$. For three different exchange coupling strengths J, the scaling ansatz (4.36) is demonstrated in figure 5.2.

Table 5.1 summarizes the fit results for all considered values J. Figure 5.3 shows how the fitted parameters W_{c}, α_0 and ν depend on the coupling strength J. While for Ising impurities $W_{\mathrm{c}}(J)$ decreases monotonically, in the case of Heisenberg impurities, W_{c} first increases to a maximum of $W_{\mathrm{c}}/t = 19.79 \pm 0.13$ at $J/t = 6$, before it eventually follows the Ising curve down to smaller values. This tendency is expected, as the symmetry class is changing from orthogonal to unitary. Other studies considering an external magnetic field (also in the unitary symmetry class) have found a value of $W_{\mathrm{c}}/t = 18.35 \pm 0.11$ [DBZK98]. We conclude that the additional spin symmetry breaking of the magnetic impurities causes a further increment.

It should be noted that our result for W_{c} at $J = 0$ (i.e., the pure Anderson model), is $W_{\mathrm{c}}/t = 16.20 \pm 0.06$, which is considerably smaller than established values like $W_{\mathrm{c}}/t = 16.530(16.524, 16.536)$ [RVSR11] or $16.536(16.531, 16.543)$ [SO14]. A possible reason is the neglectance of irrelevant scaling variables [SO14] in our scaling ansatz (4.35), which might be neccessary for our chosen system sizes $L \in \{10, 20, 30, 40, 50\}$. Noting that the computational effort is already quite high for our present calculations (about three months), it might however not be feasible to turn to larger system sizes.

To assess the quality for each fit, the reduced χ^2_{red} statistic is given in table 5.1. The values are all smaller than one, suggesting that the data has been *overfitted* by the fit model (4.36), given the standard error (SSE) that was calculated as described in appendix A.2. Alternatively, the SSE might have been overestimated for some unknown reason.

As can be seen in figure 5.3, also the value of α_0 appears to undergo a gradual transition to another value (i.e., its unitary value) by tuning up the concentration of Heisenberg impurities, whereas for Ising impurities, it stays fairly constant and is about compatible with recent numerical studies for its orthogonal value, $\alpha_0 = 4.048(4.045, 4.050)$ [RVSR11].

Our results for the localization length exponent ν remain rather inconclusive. Overall, at least for the orthogonal symmetry class, a much higher value $\nu = 1.590(1.579, 1.602)$ [RVSR11] is expected. As already mentioned above, the unusual small values for W_{c} and ν in case of the pure Anderson model ($J = 0$) could mean that our system sizes are not

Table 5.1.: Resulting fit parameters W_c, α_0 and ν for the different exchange coupling strengths J, including their standard deviation estimated by the fit algorithm. To assess the quality of the fit, the reduced χ^2 statistic is given.

	J/t	W_c/t	α_0	ν	χ^2_red
	0	16.20 ± 0.06	4.01 ± 0.01	1.14 ± 0.02	0.43
Heisenberg	0.1	16.73 ± 0.08	4.08 ± 0.01	1.14 ± 0.01	0.31
	0.3	17.34 ± 0.10	4.13 ± 0.01	1.15 ± 0.02	0.53
	0.5	17.64 ± 0.08	4.15 ± 0.01	1.15 ± 0.01	0.52
	0.7	17.93 ± 0.10	4.18 ± 0.01	1.14 ± 0.01	0.65
	0.9	17.96 ± 0.10	4.16 ± 0.01	1.15 ± 0.01	0.61
	1	18.11 ± 0.10	4.18 ± 0.01	1.15 ± 0.01	0.56
	2	18.80 ± 0.12	4.23 ± 0.02	1.16 ± 0.02	0.75
	3	19.08 ± 0.12	4.24 ± 0.01	1.19 ± 0.02	0.60
	4	19.69 ± 0.13	4.31 ± 0.02	1.19 ± 0.05	0.39
	5	19.44 ± 0.09	4.29 ± 0.01	1.13 ± 0.01	0.64
	6	19.79 ± 0.13	4.33 ± 0.02	1.15 ± 0.03	0.40
	7	19.52 ± 0.12	4.31 ± 0.01	1.15 ± 0.02	0.70
	8	19.58 ± 0.16	4.33 ± 0.02	1.19 ± 0.04	0.56
	9	19.40 ± 0.19	4.35 ± 0.02	1.25 ± 0.05	0.61
	10	18.08 ± 0.15	4.26 ± 0.02	1.19 ± 0.03	0.66
Ising	0.1	16.37 ± 0.07	4.03 ± 0.01	1.14 ± 0.01	0.31
	0.3	16.30 ± 0.08	4.03 ± 0.01	1.12 ± 0.02	0.44
	0.5	16.30 ± 0.08	4.03 ± 0.01	1.14 ± 0.02	0.47
	0.7	16.40 ± 0.09	4.04 ± 0.01	1.15 ± 0.02	0.55
	0.9	16.28 ± 0.08	4.02 ± 0.01	1.17 ± 0.02	0.44
	1	16.29 ± 0.08	4.02 ± 0.01	1.14 ± 0.02	0.44
	2	16.40 ± 0.07	4.04 ± 0.01	1.13 ± 0.01	0.33
	3	16.31 ± 0.11	4.03 ± 0.02	1.15 ± 0.02	0.79
	4	16.16 ± 0.07	4.01 ± 0.01	1.13 ± 0.02	0.25
	5	16.34 ± 0.08	4.04 ± 0.01	1.14 ± 0.02	0.43
	6	16.07 ± 0.09	4.01 ± 0.01	1.14 ± 0.02	0.54
	7	15.99 ± 0.08	4.02 ± 0.01	1.18 ± 0.02	0.34
	8	15.63 ± 0.05	4.00 ± 0.01	1.15 ± 0.01	0.17
	9	15.56 ± 0.08	4.01 ± 0.01	1.13 ± 0.02	0.44
	10	15.54 ± 0.09	4.02 ± 0.01	1.11 ± 0.01	0.66

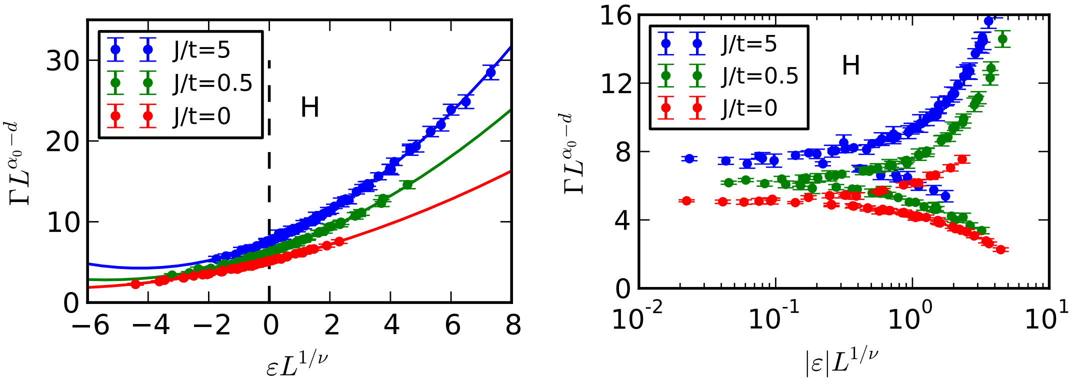

Figure 5.2.: Demonstration of the scaling ansatz (4.36) at half filling ($E = 0$) for three different values J, for the case of Heisenberg impurities. The vertical dashed line corresponds to the critical disorder, $\varepsilon = 0$.

large enough to be able to neglect irrelevant scaling variables [SO14]. Another possible reason is the large energy broadening η due to our choice of the ratio $L^3/M = 20$.

Nevertheless, the scaling of W_c with J for small $J \in [0, 1]$ is analyzed. The results are shown in figure 5.4. A scaling like

$$W_\mathrm{c} = W_\mathrm{c}^0 + W_\mathrm{c}^0 \left(\frac{a_\mathrm{c}^2}{D_\mathrm{e} \tau_\mathrm{s}^0} \right)^{\frac{1}{\varphi}} \tag{5.9}$$

has been suggested for the shift of the critical disorder W_c in the presence of local magnetic moments [KMV09, KMVS12]. W_c^0 is the critical disorder of the pure Anderson model (2.12), D_e is the diffusion constant, and $(\tau_s^0)^{-1}$ is the *magnetic relaxation rate* at zero temperature [KMVS12],

$$(\tau_\mathrm{s}^0)^{-1} = 2\pi\, n_\mathrm{M}\, S^2 \frac{J^2}{D^2}\, \rho(E_\mathrm{F}) \quad . \tag{5.10}$$

Here, $D = 12t$ is the band width in die absence of disorder. Thus, a scaling like

$$W_\mathrm{c}(J) \sim J^{2/\varphi} \tag{5.11}$$

is expected. We use the fit model $W_c(J) = aJ^\mu + b$, where $\mu = 2/\varphi$. The fitting results are summarized in table 5.2.

Scaling theory predicts $\varphi = 2\nu$ [KL81], while it has been argued that in the presence of local magnetic moments, it should rather be $\varphi = 2\nu + 3$ [Weg87b]. We test both hypotheses on our data. Figure 5.4 shows that neither of the two analytic predictions agrees perfectly with our best fit, which lies somewhere in between. On the other hand, fixing φ to one of the analytic formulas, using either the established value for ν [RVSR11] or the average value found in our FSS analysis ($\bar{\nu} = 1.15 \pm 0.02$), results in curves still

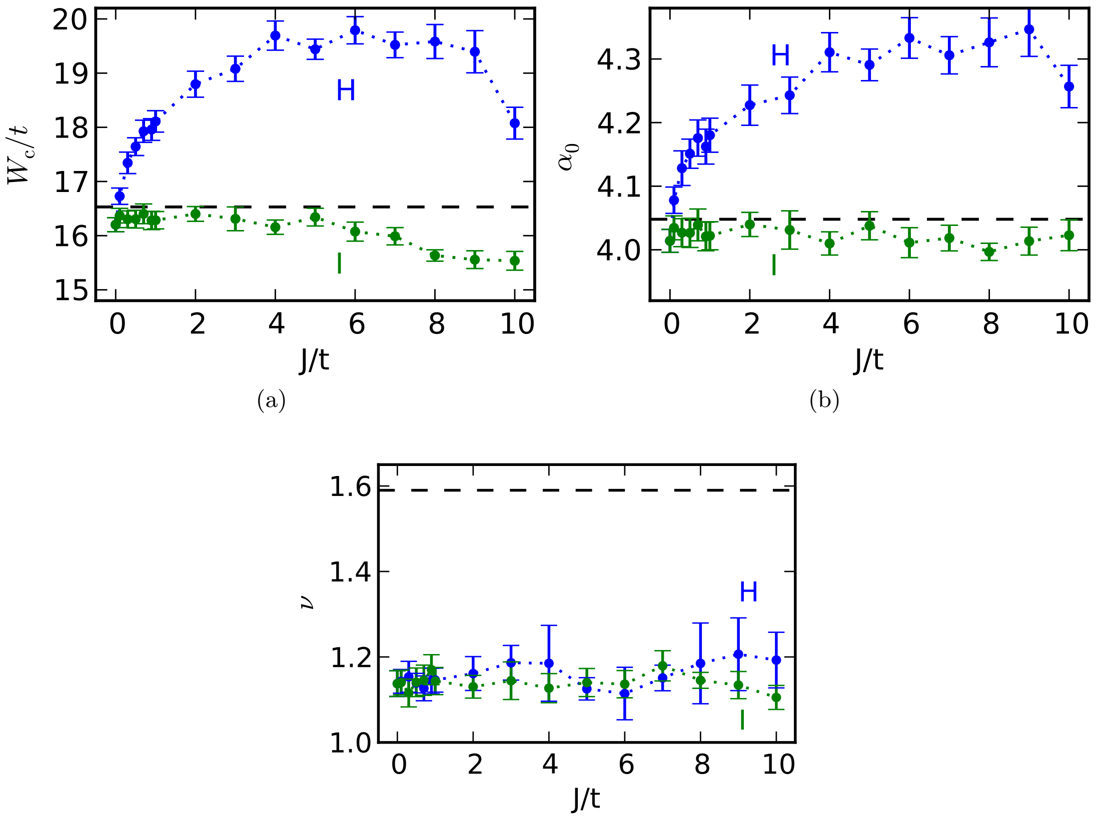

(a) (b)

(c)

Figure 5.3.: The dependence of the fit parameters (a) W_c, (b) α_0 and (c) ν on the exchange coupling J, for Heisenberg (H) as well as Ising (I) impurities. The dashed lines mark values from [RVSR11] (for the orthogonal symmetry class).

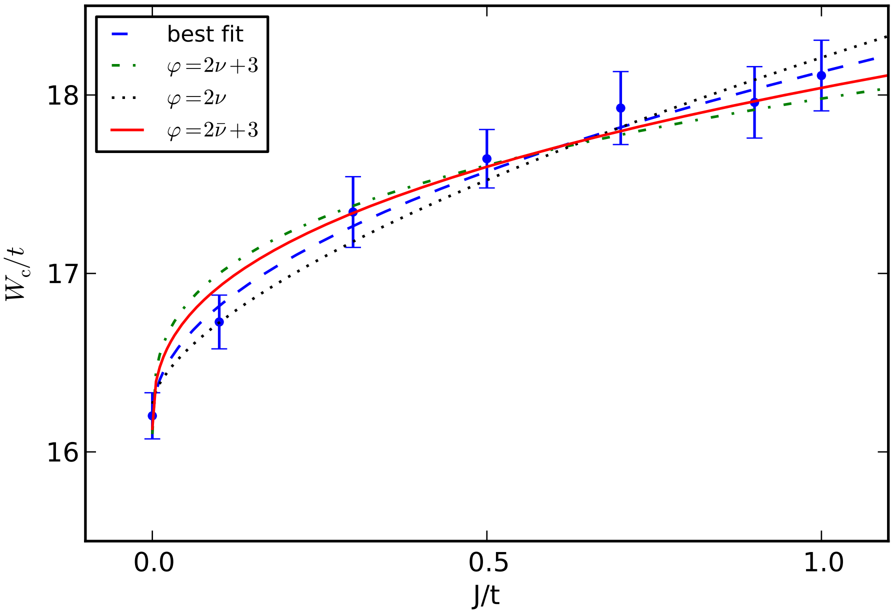

Figure 5.4.: Fitting $W_c(J)$ for small $J/t \in [0, 1]$ (Heisenberg impurities).

fitting the data quite well within the errorbars, although the quality of the fit is somewhat diminished ($\chi^2_{\mathrm{red}} > 1$). The free fit however, which yields $\mu = 2/\varphi = 0.49 \pm 0.05$, has the only decent fit quality with a reduced χ^2 statistic close to one (see table 5.2).

5.4. Influence on the phase diagram

Using the empirical scaling ansatz (4.51) and the contour finding method described in section 4.4, the phase diagram of disorder in the E-W plane can be estimated for fixed J. We show the phase trajectories for a few selected values of J in figures 5.5 and 5.6. As our data resolution on the W-axis is limited for $J > 0$, the fluctuations of the phase trajectory are higher than those obtained in the case of the Anderson model (cf. figure 4.7). Also, we have not acquired data below the range of interest for the parameter W.

Even under the above restrictions, it is interesting to analyze the tendencies of the critical disorder W_c in dependence of J for energies away from the band center. In the case of Heisenberg impurities (figure 5.5), first the shallow valley that exists in the phase trajectory for $J = 0$ around $E = 0$ dissolves for increasing J. After reaching the maximum value at about $J/t = 6$, the whole trajectory decreases to smaller values of W_c, but around $E = 0$, the drop is progressing more rapidly than in other band regions, forming a deep valley around $E = 0$ at $J/t = 10$.

Also in the case of Ising impurities (figure 5.6), the shallow valley around $E = 0$ dissolves for small couplings $J > 0$, but the values W_c never go beyond the $J = 0$

Table 5.2.: Fit results for $W_\mathrm{c}(J)$ for small values of the exchange coupling strength $J/t \in [0,1]$. In the top row, μ is a free fit parameter. Otherwise, $\mu = 2/\varphi$ is fixed to values (shown in bold) according to the given analytic formulas for φ [Weg87b, KMVS12], using either $\nu = 1.590(1.579, 1.602)$ [RVSR11] or our own average value $\bar{\nu} = 1.15 \pm 0.02$.

$\varphi = \ldots$	a	μ	b	χ^2_red
free fit	1.94 ± 0.09	0.49 ± 0.05	16.19 ± 0.06	0.99
$2\nu + 3$	1.88 ± 0.16	**0.32**	16.10 ± 0.11	3.45
2ν	1.94 ± 0.12	**0.63**	16.27 ± 0.07	1.91
$2\bar{\nu} + 3$	1.91 ± 0.12	**0.38**	16.13 ± 0.08	1.92
$2\bar{\nu}$	1.90 ± 0.23	**0.87**	16.40 ± 0.13	6.61

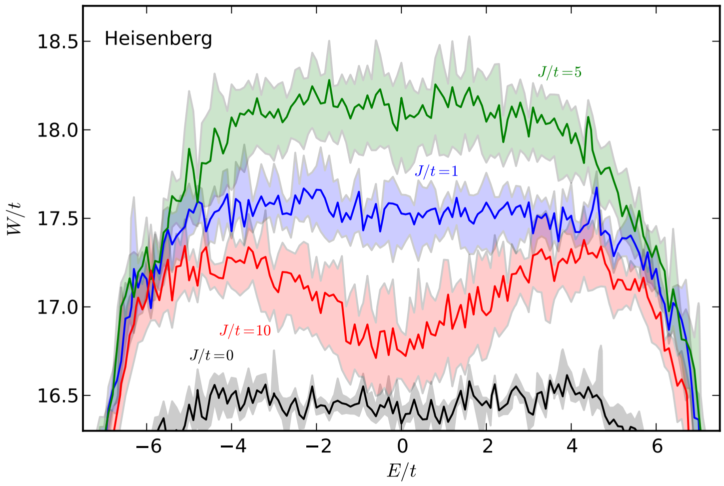

Figure 5.5.: Phase diagram of the Anderson-Heisenberg model for selected values of the exchange coupling strength J, obtained using the empirical scaling ansatz (4.51).

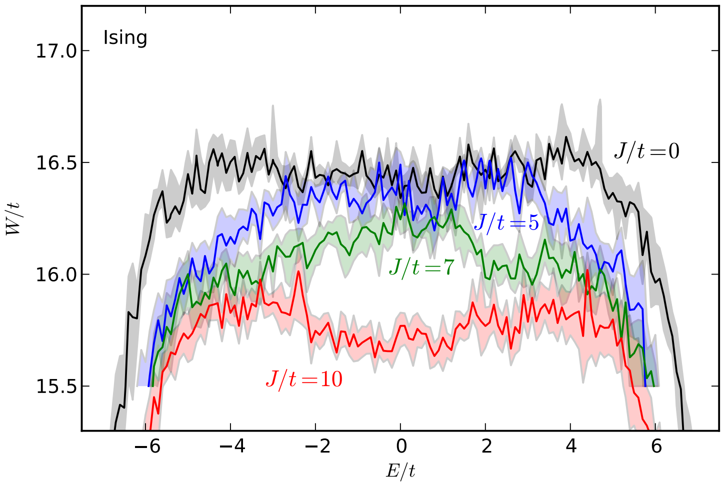

Figure 5.6.: Phase diagram of the Anderson-Ising model for selected values of the exchange coupling strength J, obtained using the empirical scaling ansatz (4.51).

trajectory. There is a strict downward tendency for all energies. For very large exchange couplings, as shown for $J/t = 10$, the valley at the band center reappears, similar to the case of Heisenberg impurities.

However, these findings should be considered with caution. As discussed in section 4.4, using the empirical scaling ansatz (4.51) is an approximate method at best, especially when moving away from the band center $E = 0$, where the second argument of the function $F(x, y)$ in equation (4.36) cannot be considered constant. According to equation (3.30), η is a non-trivial function of M and E, and the DOS $\rho_{\rm av}(E)$ is obviously far from constant when approaching the band edge. Scaling with the exponent p in equation (4.51) then means altering both arguments of $F(x, y)$ at the same time, which is hard to control. Still, our results for the phase diagrams might provide a first qualitative glimpse. More accurate investigations of the full phase diagram of disorder of the Anderson-Heisenberg model (5.2) remain to be done.

6. Conclusions

In this thesis, the effects of local magnetic moments on the Anderson metal-insulator transition (AMIT) have been investigated. Chapter 2 reviewed fundamental aspects regarding the problem of localization that were related to the present analysis, including a clarification of the physical situation leading to the metal-insulator transition (MIT) in phosphorus-doped silicon (Si:P) [vL00]. An effective model has been used to approximate the dynamics of the impurity band electrons in Si:P in the presence of local magnetic moments, based on the concept of a two-fluid model [Sac89].

In chapter 3, the numerical methods used in the analysis were explained. The kernel polynomial method (KPM) was used to calculate the local density of states (LDOS) [WWAF06]. A finite-size scaling (FSS) ansatz for the typical density of states, which is the geometric ensemble average of the LDOS (GLDOS), has been introduced in chapter 4 [ASO06] and tested against established results for the Anderson model [And58]. Furthermore, a simple empirical scaling ansatz for the GLDOS has been considered, which allowed for a qualitative estimation of the phase diagram in the energy-disorder plane [JCK12].

Using the FSS ansatz, the effective model for the impurity band electrons has been studied in chapter 5. The formation of local magnetic moments was approximated by an exchange coupling of the itinerant electrons to two kinds of classical magnetic impurities: Heisenberg impurities and Ising impurities. The influence of the exchange coupling parameter on the critical disorder strength at half filling has been examined for fixed impurity concentration. Also, the empirical scaling ansatz has been used to observe the qualitative behavior of the critical disorder away from half filling, under the influence of an increasing coupling strength.

We find that in the presence of Heisenberg impurities, the critical disorder W_c increases for a certain range of coupling parameter values J, while Ising impurities lower W_c for increasing J. This behavior can be qualitatively explained by a change of symmetry from orthogonal to unitary, caused by the Heisenberg impurities. Also a modification of the parameter α_0, which originates from the description of the multifractal properties of critical states, is observed when entering the unitary regime. We can roughly estimate its unitary value to $\alpha_0 \approx 4.3$. It would be interesting to see this value verified (or falsified) by alternative approaches.

Despite meeting expectations qualitatively, it was only partially possible to reproduce established values for the parameters characterizing the AMIT. While the orthogonal value for α_0 ($\alpha_0 = 4.01 \pm 0.01$) matches the expected value $\alpha_0 = 4.048(4.045, 4.050)$ [RVSR11] quite well, our result for $\nu \approx 1.15 \pm 0.02$ is considerably smaller than the expected value $\nu = 1.590(1.579, 1.602)$ [RVSR11]. Also the critical disorder amplitude $W_\mathrm{c}/t \approx 16.20 \pm 0.06$ of the pure Anderson model deviates somewhat from the value

$W_c/t = 16.530(16.524, 16.536)$ [RVSR11], which has been confirmed on several occasions using various methods during the past decades [BSK87, KM93, BK94, EM08].

The solutions to the above problems could be found by using a better energy resolution within the KPM, or by considering irrelevant scaling variables in the finite-size scaling ansatz [SO14]. However, both measures would require a significant increase of numerical effort. Taking into account the disorder dependence of the average density of states could also improve the scaling analysis, although test calculations have not shown a significant impact on the fitting results. Future investigations should keep the second argument of the scaling ansatz exactly constant anyway, to allow for a precise estimate of the phase transition away from half filling.

We find moderate agreement with analytical predictions [KL81, Weg87b, KMVS12] for the scaling exponent of the function $W_c(J)$. However, because of the above problems, and also because of the limited accuracy of the data, we can not exclude the validity of either of them with certainty. The methodological issues have to be solved first, and testet against known results for well-studied systems like the Anderson model.

The results for the complete phase diagram in the energy-disorder plane show good qualitative agreement with established results for the pure Anderson model [BSK87, SF09], despite the vast approximations considered in the empirical FSS ansatz. Also the evolution of the phase diagram of the Anderson-Heisenberg model for an increasing coupling strength already gives some insight into the effects of local magnetic moments on the phase transition. However, future investigations should consider the full scaling ansatz, also away from the band center. This will require the consideration of the precise energy and disorder dependence of the average density of states and of the energy dependence of the energy resolution within the KPM.

Finally, the significance of the effective model that is used to study the influence of magnetic moments on the Anderson transition is limited, considering the MIT in real Si:P. It successfully shows that the critical disorder strongly depends on the coupling strength. It can be expected that also the critical dopant density is significantly determined by the concentration of local moments present in Si:P. However, in real Si:P, the concentration of moments is a function of the dopant density itself, and the strength of the Coulomb repulsion must be taken into account as well. It is therefore desirable to consider a more sophisticated variant of the Anderson-Hubbard model in coming investigations, which is more closely related to the situation in real materials, going beyond the concept a two-fluid model [Sac89].

Overall, it can be summarized that problems occur mostly due to immaturenesses of this innovative combination of numerical methods, partly within the relatively unexplored kernel polynomial method, partly in minute details within the scaling ansatz for the typical density of states. There is hope that these problems will turn out as small flaws that can be eradicated after some further development, and to find a reliable method for studying the metal-insulator transition in various models.

Acknowledgements

First of all I would like to express my gratitude to my advisor Prof. Dr. Stefan Kettemann for the good guidance over the years. I would also like to thank the other members of the dissertation committee, Prof. Dr. Ulrich Kleinekathöfer and Prof. Dr. Keith Slevin, for their willingness to assess my work. Further, I am very thankful for all the fruitful discussions with Prof. Dr. Keith Slevin and my former colleagues Prof. Dr. Georges Bouzerar, Dr. Paul Wenk, Dr. Akash Chakraborty, Dr. Hyunyong Lee, and Llea Samuel. I thank Prof. Dr. Vincent Sacksteder IV for useful suggestions regarding certain aspects of the numerical methods.

Working in the field of computational science, I certainly have to mention the excellent technical support by Dr. Achim Gelessus and Florian Neu at the Computational Laboratories for Analysis, Modeling and Visualization (CLAMV), Jacobs University Bremen, Germany, which is also hosting the computer facilities on which the calculations were performed. The work was partly supported by the World Class University (WCU) program through the National Research Foundation of Korea funded by the Ministry of Education, Science and Technology (R31-2008-000-10059-0), Division of Advanced Materials Science.

A. Miscellaneous derivations

In this appendix, some lengthy derivations of minor importance are carried out that did not fit into the main text.

A.1. Recurrence relations for Chebychev polynomials of first kind

The Chebychev polynomials of the first kind read [WWAF06]

$$T_m(x) = \cos(m \ \arccos(x)) \quad . \tag{A.1}$$

There exist recurrence relations

$$T_{m+1}(x) = 2x\,T_m(x) - T_{m-1}(x) \tag{A.2}$$

for all $m > 0$, with $T_0(x) = 1$ and $T_1(x) = x$.

In the following it is shown that the recurrence relations (A.2) hold for the Chebychev polynomials (A.1):

Proof. Start from (A.2),

$$T_{m+1}(x) = 2x\,T_m(x) - T_{m-1}(x) \quad . \tag{A.3}$$

Insert the definition of Chebychef polynomials (A.1),

$$\cos((m+1)\arccos(x)) = 2x\cos(m\arccos(x)) - \cos((m-1)\arccos(x)) \quad .$$

Make the substitution $y = \arccos(x)$,

$$\begin{aligned}
\cos((m+1)y) + \cos((m-1)y) &= 2\cos(y)\cos(my) \\
\cos(my+y) + \cos(my-y) &= 2\cos(y)\cos(my) \\
\cos(my)\cos(y) - \sin(my)\sin(y) + \cos(my)\cos(y) + \sin(my)\sin(y) &= 2\cos(y)\cos(my) \\
2\cos(my)\cos(y) &= 2\cos(y)\cos(my)
\end{aligned}$$

□

A.2. Sample variance of the geometric mean

The arithmetic mean $\bar{x}$ of a discrete random variable x is defined as

$$\bar{x} = \frac{1}{N} \sum_{i=1}^{N} x_i \quad , \tag{A.4}$$

where N is the sample size. It is a good estimator for the population mean. Its (unbiased) sample variance is well known,

$$\sigma_x^2 = \frac{1}{N-1} \sum_{i=1}^{N} (x_i - \bar{x})^2 = \frac{\overline{x^2}}{N-1} - \frac{\bar{x}^2}{N(N-1)} \quad . \tag{A.5}$$

We introduce the quantity y, which is defined as the logarithm of the random variable x, $y = \log x$. Its arithmetic mean and variance is calculated according to (A.4) and (A.5),

$$\bar{y} = \overline{\log x} = \frac{1}{N} \sum_{i=1}^{N} \log x_i \quad , \tag{A.6}$$

$$\sigma_y^2 = \sigma_{\log x}^2 = \frac{1}{N-1} \sum_{i=1}^{N} (\log x_i - \overline{\log x})^2 = \frac{\overline{(\log x)^2}}{N-1} - \frac{\overline{\log x}^2}{N(N-1)} \quad . \tag{A.7}$$

Now, the geometric mean of x is

$$z = \mathrm{e}^{\overline{\log x}} = \mathrm{e}^{y} \quad . \tag{A.8}$$

We estimate the statistical error of z, given by its standard deviation σ_z, by

$$\sigma_z = z_1 - z_2 = \mathrm{e}^{\bar{y}} (\mathrm{e}^{\sigma_y} - 1) \quad , \tag{A.9}$$

with

$$z_1 = \mathrm{e}^{\bar{y} + \sigma_y} \tag{A.10}$$

$$z_2 = \mathrm{e}^{\bar{y}} \quad . \tag{A.11}$$

Assuming σ_y to be small, we approximate

$$\sigma_z = \mathrm{e}^{\bar{y}} (\mathrm{e}^{\sigma_y} - 1) \approx \mathrm{e}^{\bar{y}} \sigma_y \tag{A.12}$$

and hence the estimate of the sample variance of the geometric mean is given by

$$\sigma_z^2 \approx \mathrm{e}^{2\bar{y}} \sigma_y^2 \quad . \tag{A.13}$$

The same result has been obtained by Norris [Nor40] using more profound mathematical arguments.

B. Additional remarks regarding the numerical methods

For the analysis in this work, extensive software had to be developed, mainly due to the lack of available implementations of tight binding models[1] and the kernel polynomial method (KPM) [WWAF06]. The implementation was mainly done in the object-oriented programming language Python [Dub99, Oli07, Lan08], extended by the popular modules `numpy` [ADH+99] and `scipy` [JOPO07]. Performance-criticial parts have been written in Cython [Sel09, BBC+11], a project which aims to become a superset of Python, adding the ability to be partially translated to statically compilable C code. All figures have been created using the `matplotlib` library [Hun07].

The author encourages the use and publication of open source software, as it spurs scientific productivity and a rapid exchange of ideas. In this manner, the software developed in this thesis is going to be published as an open source software project in the near future[2]. May it serve as a starting point for future investigations, or as the basis of a larger open source project offering different forms of tight binding and kernel expansion techniques to the Python community.

Using our implementation of the kernel polynomial method (KPM) (see chapter 3), it is easy to obtain the density of states (DOS) (2.10) or the local density of states (LDOS) (3.1) of a tight binding Hamiltonian. In the absense of disorder, the DOS of the Hamiltonian (2.1) is identical to the LDOS at any lattice site, so the KPM algorithm for the LDOS can be used for its calculation (see section 3.2.4). To illustrate the usage of our software, the source code used to obtain figure 2.2 is given:

```
import tb.sc, kpm, matplotlib.pyplot
mat = tb.sc.scnnmat(shape=(100, 100, 100), format='csr')
energ, dens = kpm.ldos(mat, estep=.1, erange=(-7, 7), limit=350)
matplotlib.pyplot.plot(energ, dens)
```

The total execution time is about 25 seconds (using a standard desktop computer), where most of the time is spent on creating the tight binding matrix of this rather big system with $N = L^3 = 100^3$ lattice sites (second line in the source code).

---

[1] In the meantime, there exists another project regarding tight binding models in Python, focussing mainly on band structure calculations: `http://www.physics.rutgers.edu/pythtb/`.

[2] The main projects are hosted at `http://github.com/proggy/tb/` and `http://github.com/proggy/kpm/`.

B.1. Fitting methods

For fitting model functions to our data we use the Python module *lmfit* [New13], which utilizes the Levenberg-Marquardt algorithm [Lev44, Mar63] for the minimization of the squared residuals. Besides some advantages of the *lmfit* module concerning usability (e.g., object-oriented organization of model parameters), this constitutes the standard practice in numerical science.

The error of our input data is accounted for in the form of a linear weighting of the data points. The residual function is defined as usual,

$$R(x, y, s_y, P) = \frac{f(x, P) - y}{s_y} \quad , \tag{B.1}$$

where y is the independent data value, s_y the associated error value (in our case, the standard error of either the arithmetic or the geometric mean), and x the dependent data value. $f(x)$ is the fit model that is meant to fit the data. The sum of the squared residuals $R(x, y, s_y, P)$ is then minimized to find the optimal set of fit parameters P (*least-squares method*). The residual function can easily be generalized to the case of multiple dependent data values x, as it is needed for the scaling ansatz for the GLDOS (see chapter 4).

Like many other implementations of the Levenberg-Marquardt algorithm, also *lmfit* is yielding an estimate for the covariance matrix. So an estimate of the standard deviation of the resulting fit parameters can be obtained by taking the square root of the diagonal elements of that matrix, which allows for an indirect but simple way to propagate the error of the original data.

List of Figures

List of Tables

List of acronyms

The number in brackets is the page of first occurence or explanation of the term.

1BZ First Brillouin zone (14)

ADOS Ensemble-averaged density of states (57)

ALDOS Arithmetic average of the local density of states (53)

CSR Compressed sparse row (matrix format) (48)

DOS Density of states (9)

ETBM Effective tight binding model (39)

FCT Fast cosine transform (51)

FFT Fast Fourier transform (46)

FSS Finite-size scaling (12)

GLDOS Geometric average of the local density of states (53)

HWHM Half width at half maximum (20)

KPM Kernel polynomial method (42)

LDOS Local density of states (42)

MFA Multifractal analysis (25)

PBC Periodic boundary conditions (14)

PDF Probability density function (19)

RMT Random matrix theory (24)

SLDOS Spin-resolved local density of states (79)

SSE Standard error (53)

STM Scanning Tunneling Microscopy (34)

TRS Time-reversal symmetry (24)

VMKPM Variable-moment kernel polynomial method (52)

WFI Wave function intensity (25)

List of symbols

The number in brackets is the page where the symbol is defined or used for the first time.

a Lattice spacing (15)

a, b Rescaling parameters (46)

α Wave function intensity scaling exponent (26)

α_0 Position of the maximum of the singularity spectrum $f(\alpha)$ in the weak-multifractality limit (27)

d Number of dimensions (18)

D_q Fractal dimensions (26)

Δ_q Anomalous dimensions (26)

E Energy (15)

E_k Eigenenergy, eigenvalue of the Hamiltonian $\hat{H}$ (14)

E_{M} Mobility edge (critical energy) (20)

ε Reduced disorder or reduced energy (62)

ε_i Site potentials (13)

φ Azimuth impurity spin angle (78)

γ Parameter controlling the shape of the parabolic singularity spectrum (27)

Γ Ratio of typical and average density of states (67)

H Tight binding matrix (45)

$\hat{H}$ Hamiltonian (14)

$\hat{H}_0$ Basic Hamiltonian without magnetic impurities (77)

$\hat{H}_{\mathrm{s}}$ Part of the Hamiltonian describing the coupling of the electron spin to classical magnetic impurities (78)

η Energy broadening (inverse of energy resolution) (51)

i, j Lattice site indices (14)

J Exchange coupling strength (78)

$\mathbf{k}$ Wave vector (14)

k Eigenstate index (17)

κ Smoothness parameter (71)

L Longitudinal system size (number of lattice sites in one dimension) (93)

m Moment index (Chebychev expansion) (44)

M Truncation limit (number of Chebychev moments) (44)

μ Exponent describing the scaling of the critical disorder W_c with exchange coupling strength J (82)

ν Localization length exponent (23)

n Dopant density (34)

n_M Fraction of dopants carrying a local moment (36)

N System size (number of lattice sites) (93)

p Exponent in the empirical scaling ansatz (73)

p Cutoff value for the exponent p (73)

θ Polar impurity spin angle (78)

$\mathbf{r}$ Point in space (14)

$\mathbf{R}$ Lattice vector (14)

$\rho_\mathrm{av}(E)$ Average density of states (53)

$\rho_\mathrm{typ}(E)$ Typical density of states (54)

$\rho(E)$ Density of states (15)

$\rho_i(E)$ Local density of states (44)

$\rho(E, \mathbf{r})$ Local density of states (continuous space form) (63)

$\mathbf{S}$ Classical magnetic moment (78)

σ Electron spin (77)

σ_x Standard deviation of x (74)

σ_{DC} DC conductivity (zero-temperature/zero-frequency limit of the conductivity) (23)

σ_{x}, σ_{y}, σ_{z} Pauli matrices (78)

σ Vector containing the Pauli matrices (78)

t Hopping parameter (14)

T Temperature (13)

$T_m(x)$ Chebychev polynomials (44)

τ Scattering time

W Disorder parameter, width of the box distribution (17)

W_{c} Critical disorder (18)

ξ_{corr} Correlation length (62)

ξ_{loc} Localization length (23)

Z Coordination number (number of nearest neighbors) (14)

List of conferences and publications

Journal articles

- Daniel Jung, Keith Slevin, and Stefan Kettemann, *Anderson Metal-Insulator Transitions With Classical Magnetic Impurities*, to be submitted.

Proceedings

- Daniel Jung, Gerd Czycholl, and Stefan Kettemann, *Finite Size Scaling of the Typical Density of States of Disordered Systems Within the Kernel Polynomial Method*, Int. J. Mod. Phys. Conf. Ser. **11**, 108 (2012), doi:10.1142/S2010194512005983.
- Daniel Jung, and Stefan Kettemann, *Anderson Metal-Insulator Transitions with Classical Magnetic Impurities*, AIP conference proceedings (to be published).

Talks

The presenting contributor is marked in bold.

- **Daniel Jung**, and Stefan Kettemann, *Numerical Investigations of Metal-Insulator Transitions in Doped Semiconductors*, oral presentation, NanoFun Center and NanoMol Graduate Program Retreat, Clausthal-Zellerfeld, Germany (May 30–June 1, 2012).
- **Daniel Jung**, Keith Slevin, and Stefan Kettemann, *Anderson Metal-Insulator Transitions With Classical Magnetic Impurities*, talk, DPG Spring Meeting (Dresden 14), TU Dresden, Germany (March 30–April 4, 2014).

Posters

- **Daniel Jung**, Gerd Czycholl, and Stefan Kettemann, *Finite Size Scaling of the Typical Density of States Using the Kernel Polynomial Method*, APCTP Conference on Localisation 2011, Pohang, South Korea (August 4–7, 2011).
- **Daniel Jung**, Gerd Czycholl, and Stefan Kettemann, *Finite Size Scaling of the Typical Density of States Using the Kernel Polynomial Method*, DPG Spring Meeting (Berlin 12), TU Berlin, Germany (March 25–30, 2012).

- **Daniel Jung**, and Stefan Kettemann, *Anderson Metal-Insulator Transitions with Classical Magnetic Impurities*, 15th International Conference on Transport in Interacting Disordered Systems (TIDS 15), Sant Feliu de Guíxols, Barcelona, Spain (September 1–5, 2013).
- **Daniel Jung**, Keith Slevin, and Stefan Kettemann, *Anderson Metal-Insulator Transitions With Classical Magnetic Impurities*, poster, Recent Progress and Perspectives in Scaling, Multifractality, Interactions, and Topological Effects Near Anderson Transitions (RPSAT 14), MPIPKS Dresden, Germany (March 11–14, 2014).

Bibliography

[Abr79] E. Abrahams. Scaling Theory of Localization: Absence of Quantum Diffusion in Two Dimensions. *Physical Review Letters*, 42(10):673–676, March 1979.

[ADH$^+$99] David Ascher, P F Dubois, Konrad Hinsen, James Hugunin, and Travis Oliphant. *Numerical Python.* Lawrence Livermore National Laboratory, Livermore, CA, 1999.

[AM76] Neil W Ashcroft and N David Mermin. *Solid State Physics.* Brooks/Cole, Belmont, 1976.

[And58] PW Anderson. Absence of diffusion in certain random lattices. *Physical Review*, 109:1492–1505, 1958.

[And61] PW Anderson. Localized Magnetic States in Metals. *Physical Review*, 124(1):41–53, October 1961.

[ASO04] Yoichi Asada, Keith Slevin, and Tomi Ohtsuki. Numerical estimation of the β function in two-dimensional systems with spin-orbit coupling. *Physical Review B*, 70(3):035115, July 2004.

[ASO05] Yoichi Asada, Keith Slevin, and Tomi Ohtsuki. Anderson Transition in the Three Dimensional Symplectic Universality Class. *Journal of the Physical Society of Japan*, 74(Suppl):238–241, January 2005.

[ASO06] Yoichi Asada, Keith Slevin, and Tomi Ohtsuki. Finite size scaling of the local density of states at the Anderson transition. *unpublished*, 2006.

[BBC$^+$11] Stefan Behnel, Robert Bradshaw, Craig Citro, Lisandro Dalcin, Dag Sverre Seljebotn, and Kurt Smith. Cython: The Best of Both Worlds. *Computing in Science & Engineering*, 13(2):31–39, March 2011.

[BK94] D Belitz and TR Kirkpatrick. The Anderson-Mott transition. *Reviews of Modern Physics*, 66(2), 1994.

[BL82] RN Bhatt and PA Lee. Scaling Studies of Highly Disordered Spin- Antiferromagnetic Systems. *Physical Review Letters*, 48(5):1–4, 1982.

[BR81] RN Bhatt and TM Rice. Single-particle energy levels in doped semiconductors at densities below the metal-nonmetal transition. *Physical Review B*, 23(4), 1981.

[BSK87] B Bulka, M Schreiber, and B Kramer. Localization, quantum interference, and the metal-insulator transition. *Zeitschrift für Physik B Condensed Matter*, 30:21–30, 1987.

[BSMM00] Ilja N Bronstein, Konstantin A Semendjajew, Gerhard Musiol, and Heiner Mhlig. *Taschenbuch der Mathematik.* Harri Deutsch, 5., berar edition, August 2000.

[BW71] DW Bacon and DG Watts. Estimating the transition between two intersecting straight lines. *Biometrika*, 58(3):525–534, 1971.

[CB10] Akash Chakraborty and Georges Bouzerar. Dynamical properties of a three-dimensional diluted Heisenberg model. *Physical Review B*, 81(17):5, March 2010.

[CBB11] Akash Chakraborty, R Bouzerar, and Georges Bouzerar. Magnetic spin excitations in Mn doped GaAs: a model study. *The European Physical Journal ...*, 1:1–5, 2011.

[CBKB12] Akash Chakraborty, R Bouzerar, Stefan Kettemann, and Georges Bouzerar. Nanoscale inhomogeneities: A new path toward high Curie temperature ferromagnetism in diluted materials. *Physical Review B*, 014201:1–7, 2012.

[CP86] C Castellani and L Peliti. Multifractal wavefunction at the localisation threshold. *Journal of Physics A: Mathematical and General*, 19(8):L429, 1986.

[Czy08] Gerd Czycholl. *Theoretische Festkrperphysik.* Springer, 3. aufl. edition, 2008.

[DBZK98] T Dröse, Markus Batsch, IK Zharekeshev, and Bernhard Kramer. Phase diagram of localization in a magnetic field. *Physical Review B*, 57(1):37–40, 1998.

[Dub99] Paul F Dubois. Ten Good Practices In Scientific Programming. *Computing in Science and Engineering*, 1(1):7–11, 1999.

[Dys62] Freeman J. Dyson. The Threefold Way. Algebraic Structure of Symmetry Groups and Ensembles in Quantum Mechanics. *Journal of Mathematical Physics*, 3(6):1199, 1962.

[EM08] F Evers and AD Mirlin. Anderson transitions. *Reviews of Modern Physics*, 80(4):63, July 2008.

[ETT$^+$14] C E Ekuma, H Terletska, K.-M. Tam, Z.-Y. Meng, J Moreno, and M Jarrell. Typical medium dynamical cluster approximation for the study of Anderson localization in three dimensions. *Physical Review B*, 89(8):081107, February 2014.

[GS92] Heiko Grussbach and Michael Schreiber. Multifractality of wave functions and wave packets at the metal-insulator transition in the Anderson model of localization. *Physica A: Statistical Mechanics and its Applications*, 191(1-4):394–400, 1992.

[Hub63] J. Hubbard. Electron Correlations in Narrow Energy Bands. *Proceedings of the Royal Society A: Mathematical, Physical and Engineering Sciences*, 276(1365):238–257, November 1963.

[Hun07] J D Hunter. Matplotlib: A 2D Graphics Environment. *Computing in Science Engineering*, 9(3):90–95, 2007.

[Jan98] Martin Janssen. Statistics and scaling in disordered mesoscopic electron systems. *Physics Reports*, 295(1-2):1–91, 1998.

[JCK12] Daniel Jung, Gerd Czycholl, and Stefan Kettemann. Finite Size Scaling of the Typical Density of States of Disordered Systems Within the Kernel Polynomial Method. *International Journal of Modern Physics: Conference Series*, 11:108–113, January 2012.

[JOPO07] Eric Jones, Travis Oliphant, Pearu Peterson, and Others. {SciPy}: Open source scientific tools for {Python}, 2007.

[Jun10] Daniel Jung. *Numerische Untersuchungen zum Lokalisierungsproblem mittels Tight-Binding-Modellen und direkter Diagonalisierung.* Diplomarbeit, University of Bremen, 2010.

[KL81] DE Khmel'nitskii and AI Larkin. Mobility edge shift in external magnetic field. *Solid State Communications*, 39(10):1069–1070, 1981.

[KM93] Bernhard Kramer and A MacKinnon. Localization: theory and experiment. *Reports on Progress in Physics*, 56(June):1469–1564, 1993.

[KMV09] S Kettemann, E Mucciolo, and I Varga. Critical Metal Phase at the Anderson Metal-Insulator Transition with Kondo Impurities. *Physical Review Letters*, 103(12):126401, September 2009.

[KMVS12] S Kettemann, ER Mucciolo, I Varga, and K Slevin. Kondo-Anderson transitions. *Physical Review B*, 85(11):115112, 2012.

[Lan51] C Lanczos. An Iteration Method for the Solution of the Eigenvalue Problem of Linear Differential and Integral Operators. *Journal of research of the National Bureau of Standards*, 45:255–282, 1951.

[Lan08] Hans Petter Langtangen. *Python Scripting for Computational Science.* Texts in Computational Science and Engineering. Springer, 2008.

[Lev44] Kenneth Levenberg. A Method for the Solution of Certain Non-Linear Problems in Least Squares. *Quarterly of Applied Mathematics*, 2:164–168, 1944.

[LT78] D. C. Licciardello and D. J. Thouless. n disordered systems 11 . *Journal of Physics C*, 11(5):925, 1978.

[LT85] Patrick A. Lee and T. V. Ramakrishnan. Disordered electronic systems. *Reviews of Modern Physics*, 57(2):287–337, April 1985.

[LvTW09] Ad Lagendijk, Bart van Tiggelen, and Diederik S Wiersma. Fifty years of Anderson localization. *Physics Today*, 62(8):24–29, 2009.

[Mar63] Donald W. Marquardt. An Algorithm for Least-Squares Estimation of Nonlinear Parameters. *Journal of the Society for Industrial and Applied Mathematics*, 11(2):431–441, June 1963.

[MFT99] A Möbius, C Frenzel, and R Thielsch. Metal-insulator transition in amorphous Si_ {1-x} Ni_ {x}: Evidence for Mott's minimum metallic conductivity. *Physical Review B*, 60(20):18–22, 1999.

[Mil00] Frank Milde. *Disorder-induced metal-insulator transition in anisotropic systems.* Dissertation, Technische Universität Chemnitz, July 2000.

[Mot67] N. F. Mott. Electrons in disordered structures. *Advances in Physics*, 16(61):49–144, January 1967.

[Mot68] N. F. Mott. Metal-insulator transition. *Reviews of Modern Physics*, 40(4):677–683, 1968.

[Mot72] N. F. Mott. Conduction in non-crystalline systems IX. the minimum metallic conductivity. *Philosophical Magazine*, 26(4):1015–1026, October 1972.

[Mot90] N.F. Mott. *Metal-insulator transitions.* Taylor & Francis, London, second edition, 1990.

[Mou07] Daniel Mourad. Vergleichende Modellierung von Halbleiter-Quantenpunkten. Diplomarbeit, Universitt Bremen, Bremen, September 2007.

[MSB89] M Milovanović, Subir Sachdev, and RN Bhatt. Effective-field theory of local-moment formation in disordered metals. *Physical Review Letters*, 63(1), 1989.

[New13] Matthew Newville. lmfit, 2013.

[Nob77] The Nobel Prize in Physics 1977. *Nobelprize.org*, 1977.

[Nor40] N Norris. The standard errors of the geometric and harmonic means and their application to index numbers. *The annals of mathematical statistics*, 11(4):445–448, 1940.

[Oli07] T E Oliphant. Python for Scientific Computing. *Computing in Science and Engineering*, 9(3):10–20, May 2007.

[PGBS88] MA Paalanen, JE Graebner, RN Bhatt, and S Sachdev. Thermodynamic behavior near a metal-insulator transition. *Physical Review Letters*, 61(5):597–600, 1988.

[Phi12] Philip Phillips. *Advanced Solid State Physics*. Cambridge University Press, 2012.

[PSBR86] MA Paalanen, S Sachdev, RN Bhatt, and AE Ruckenstein. Spin dynamics of nearly localized electrons. *Physical review letters*, 57(16):2061, 1986.

[RMP$^+$83] TF Rosenbaum, RF Milligan, MA Paalanen, GA Thomas, RN Bhatt, and W. Lin. Metal-insulator transition in a doped semiconductor. *Physical Review B*, 27(12):7509–7523, June 1983.

[RVR08] Alberto Rodriguez, Louella J Vasquez, and Rudolf A Römer. Multifractal analysis of the metal-insulator transition in the three-dimensional Anderson model. II. Symmetry relation under ensemble averaging. *Phys. Rev. B*, 78(19):195107, November 2008.

[RVR09] Alberto Rodriguez, Louella J Vasquez, and Rudolf A Römer. Multifractal Analysis with the Probability Density Function at the Three-Dimensional Anderson Transition. *Phys. Rev. Lett.*, 102(10):106406, 2009.

[RVSR10] Alberto Rodriguez, Louella J. Vasquez, Keith Slevin, and Rudolf a. Römer. Critical Parameters from a Generalized Multifractal Analysis at the Anderson Transition. *Physical Review Letters*, 105(4):046403, July 2010.

[RVSR11] Alberto Rodriguez, Louella J. Vasquez, Keith Slevin, and Rudolf Römer. Multifractal finite-size scaling and universality at the Anderson transition. *Physical Review B*, 84(13):134209, October 2011.

[Sac89] Subir Sachdev. Local moments near the metal-insulator transition. *Physical Review B*, 39(8):5297–5310, 1989.

[Sch85] Michael Schreiber. Numerical evidence for power-law localisation in weakly disordered systems. *Journal of Physics C: Solid State Physics*, 18(12):2493, 1985.

[Sel09] DS Seljebotn. Fast numerical computations with Cython. In *Proceedings of the 8th Python in Science conference*, pages 15–22, Norway, 2009.

[SF09] G Schubert and H Fehske. *Quantum and Semi-classical Percolation and Breakdown in Disordered Solids*, volume 762 of *Lecture Notes in Physics*. Springer Berlin Heidelberg, Berlin, Heidelberg, 2009.

[SG91] Michael Schreiber and Heiko Grussbach. Multifractal wave functions at the Anderson transition. *Phys. Rev. Lett.*, 67(5):607–610, July 1991.

[SL97] HG Schlager and H Löhneysen. Susceptibility of local magnetic moments in phosphorus-doped silicon near the metal-insulator transition. *Europhysics Letters*, 661, 1997.

[SO14] Keith Slevin and Tomi Ohtsuki. Critical exponent for the Anderson transition in the three-dimensional orthogonal universality class. *New Journal of Physics*, 16(1):015012, January 2014.

[SW82] Frank Szmulowicz and JK Wendeln. Tetrahedral subdivision of the irreducible wedge for Brillouin zones of cubic lattices. *Physical Review B*, 25(4):2428–2432, 1982.

[vL98] H. von Löhneysen. Current issues in the physics of heavily doped semiconductors at the metal-insulator transition. *Philosophical Transactions of the Royal Society A: Mathematical, Physical and Engineering Sciences*, 356(1735):139–156, January 1998.

[vL00] H. von Löhneysen. Disorder, electron-electron interactions and the metal-insulator transition in heavily doped Si:P. *Advances in Solid State Physics*, 40:143–167, 2000.

[VRR08] Louella J Vasquez, Alberto Rodriguez, and Rudolf A Römer. Multifractal analysis of the metal-insulator transition in the three-dimensional Anderson model. I. Symmetry relation under typical averaging. *Phys. Rev. B*, 78(19):195106, November 2008.

[Weg86] FJ J Wegner. Crossover of the mobility edge behaviour. *Nuclear Physics B*, 270:1–9, 1986.

[Weg87a] Franz Wegner. Anomalous dimensions for the nonlinear sigma-model in 2 + ϵ dimensions (I). *Nuclear Physics B*, 280:193–209, January 1987.

[Weg87b] Franz Wegner. Anomalous dimensions for the nonlinear sigma-model in 2 + ϵ dimensions (II). *Nuclear Physics B*, 280:210–224, January 1987.

[Wig51] EP Wigner. On a class of analytic functions from the quantum theory of collisions. *The Annals of Mathematics*, 53(1):36–67, 1951.

[WWAF06] Alexander Weiße, Gerhard Wellein, Andreas Alvermann, and Holger Fehske. The kernel polynomial method. *Reviews of Modern Physics*, 78(1):275–306, March 2006.